I: THIN-FILM NANOPOROUS ANODIC ALUMINA FOR NANOBIOTECHNOLOGY
II: MICROSCALE $CD4^+$ CELL BIOSENSOR WITH SINGLE-CELL RESOLUTION FOR DIAGNOSIS OF HIV INFECTION

A Dissertation
Presented to the Faculty of the Graduate School
of Cornell University
In Partial Fulfillment of the Requirements for the Degree of
Doctor of Philosophy

by
Xingqun Jiang
August 2009

I: THIN-FILM NANOPOROUS ANODIC ALUMINA FOR NANOBIOTECHNOLOGY
II: MICROSCALE $CD4^+$ CELL BIOSENSOR WITH SINGLE-CELL RESOLUTION FOR DIAGNOSIS OF HIV INFECTION

Xingqun Jiang, Ph. D.
Cornell University 2009

Two research topics were presented in this dissertation. The first topic focused on nanoporous anodic alumina thin films and their applications in nanobiotechnology. It discussed in details the fabrication and the characterizations of nanoporous anodic alumina thin films on silicon substrates.

Two methods were presented for fabricating freestanding PAA thin films with open pores. In the first method, an alumina thin film was fabricated on a Si_3N_4-coated silicon substrate. A partly freestanding structure was achieved by removing the silicon substrates using KOH anisotropic etch. The second method, named as "double-layer anodization", was developed for fabricating partly or fully freestanding alumina thin films by utilizing a sacrificial metal layer.

The confined diffusion of small organic molecules in alumina nanopores was investigated. The diffusion system was built upon the silicon-based freestanding alumina thin film. The molecular diffusion in alumina pores was modeled as a one-dimensional Fickian flow, based on which the diffusion dynamics was characterized.

A novel DNA biosensor utilizing the large surface area of alumina films was developed. The device was based on a metal-alumina-metal vertical structure. The top and bottom metal films served as electrodes while the sandwiched alumina membrane served as a porous dielectric layer. Single-stranded DNA oligonucleotides were attached to the sidewalls of the alumina pores through chemical modifications. The DNA hybridization process was sensed by measuring the impedance spectrum of the alumina membrane between the two electrodes.

The second topic was the research of a cell biosensor for the precise quantification of human $CD4^+$ cells, orientated for the development of affordable point-of-care diagnostic tools for analyzing the HIV-infection status of AIDS patients. With this motivation, an impedance biosensor was developed, based on an array of cell-sized working electrode pixels. Each electrode pixels was able to independently detect the existence of one single cell on the electrode surface. The cell counting was digitalized by the electrode pixelation, being independent of the cell concentration. With this sensor, the detection of $CD4^+$ cells at single-cell resolution was demonstrated.

BIOGRAPHICAL SKETCH

The author of this dissertation, Xingqun Jiang, was born in Lin'an, Zhejiang in China in 1977. He studied at Changhua high school in 1993-1996. In 1996, he went to Beijing Institute of Technology for college study. Since 2003, he studied in Electrical and Computer Engineering at Cornell University. His Ph.D. research focused on the development of nanoporous materials for lab-on-chip applications, as well as the development of microscale and nanoscale biosensor chips based on silicon substrates. For years, he worked in The Cornell NanoScale Science & Technology Facility for the device fabrication, as well as in Nanobiotechnology Center at Cornell University for the research on DNA and cell biosensors. In his Ph.D. study, he independently initialized the research of silicon-based nanoporous anodic alumina thin film at Cornell and successfully used the material in the development of a solid-state DNA biosensor. He also developed a microscale impedance biosensor and demonstrated the detection of human $CD4^+$ cells at single-cell resolution on the sensor chip.

Aside the research in nanotechnology, Jiang also developed his background in object-oriented programming language and computer graphics. He worked in the Program of Computer Graphics at Cornell University, focused on the global illumination of high-complex scene for photorealistic image generation. In 2007, he worked as a student intern at Digital Domain, Inc in Los Angeles, where he focused on the distributive 3D rendering system for the generation of special effects in Hollywood films.

This dissertation is dedicated to the author's motherland, China

ACKNOWLEDGMENTS

The research projects in this dissertation were funded by The National Science Foundation of the United States of America. The device nanofabrication was mainly done at The Cornell NanoScale Science & Technology Facility (CNF). Part of the nanofabrication work, as well as the chemical and biological experiments, was done at Nanobiotechnology Center (NBTC) at Cornell University.

As a research scientist, I thank my committee chair Dr.Michael G. Spencer, colleagues Dr.Nirankar Mishra and Dr.James N. Turner, with whom I have worked closely over years. I enjoyed the research collaborations and the scientific discussions with them. I also thank Dr.Lester Eastman, Dr.George Malliaras, and Dr.Kavita Bala very much for being my special committee members.

Personally, I want to give my sincere appreciations to those who have supported me along the journey of my study at Cornell. I first thank Haiqing Liu, for going with me through years during which we conquered many difficulties. Her spiritual support will remain in my heart. I thank Zhitao Yang, Qing He, Kun Yue, Xiaoqing Xie, Hongfei Ge, and particularly my sister Jie Chen and her husband Xiaoyu Wang for their support in my commencement. I thank Zhigen Zhao and Junran Li for sharing with me many happy pingpong times. I thank Chunrong Song for her great support and encouragement in my graduation time. The days with all of you will be ever remembered. Lastly, I thank my mother Wenying Wang, my father Diyu Jiang, and especially my sister Lifen Jiang for their selfless support all the time.

TABLE OF CONTENTS

BIOGRAPHICAL SKETCH iii
DEDICATION iv
ACKNOWLEDGMENTS v
TABLE OF CONTENTS vi
LIST OF FIGURES ix
LIST OF TABLES xii
LIST OF ABBREVIATIONS xiii
CHAPTER 1: INTRODUCTION 1
1.1 Porous Anodic Alumina in Nanobiotechnology 2
1.1.1 Nanotechnology and Nanobiotechnology 2
1.1.2 Nanomaterial: Porous Anodic Alumina 5
1.1.3 Porous Anodic Alumina in Nanobiotechnology 6
1.1.4 Motivation and Focus of Dissertation 12
1.2 Review of Porous Anodic Alumina 17
1.2.1 Anodization Process 17
1.2.2 Porous Structure 20
1.2.3 Formation Mechanism 23
1.2.4 Anodization Conditions 30
1.2.5 Pattern Regularity 33
1.2.6 Material Properties 34
1.2.7 Summary 38
CHAPTER 2: FABRICATION AND CHARACTERIZATION OF THIN-FILM POROUS ANODIC ALUMINA 39
2.1 Substrates for Thin-Film Porous Anodic Alumina 40

2.2 Preparation of Thin-Film Aluminum 42
2.3 Anodization for Thin-Film PAA 45
2.4 Thin-Film PAA as Anodized 49
2.5 Pore Widening by H_3PO_4 Etch 51
2.6 Cross Section of Thin-Film PAA 59
2.7 Anodization Conditions 62
2.8 Nanoparticle Growth by PAA Thin Film 72
2.9 Tortuous PAA by Low-Voltage Anodization 74
CHAPTER 3: FREESTANDING THIN-FILM POROUS ANODIC ALUMINA 78
3.1 Background 79
3.2 Methods 82
3.2.1 Partly Freestanding PAA on Silicon 82
3.2.2 Double-Layer Anodization 83
3.3 Results and Discussion 90
3.4 Conclusion 100
CHAPTER 4: DIFFUSION OF SUB-1000-DALTON MOLECULES IN 40-NM ALUMINA NANOPORES 101
4.1 Background 102
4.2 Methods 104
4.3 Results and Discussion 109
4.4 Conclusion 118
CHAPTER 5: DNA BIOSENSOR BY METAL-ALUMINA-METAL STRUCTURE 119
5.1 Background 120
5.2 Methods 124

5.2.1 Fabrication of MAM Structure 124
5.2.2 PAA Surface Modification 130
5.2.3 Impedance Spectroscopy 134
5.3 Results and Discussion 135
5.4 Conclusion 162
CHAPTER 6: MICROSCALE $CD4^+$ CELL BIOSENSOR WITH SINGLE-CELL RESOLUTION FOR DIAGNOSIS OF HIV INFECTION 163
6.1 Background 164
6.2 Methods 167
6.2.1 Pixelated Three-Electrode System 167
6.2.2 Cell Culture 168
6.2.3 Cell Capture on Working Electrode 168
6.2.4 Electrochemical Impedance Spectroscopy 169
6.3 Results and Discussion 173
6.4 Conclusion 185
REFERENCES 186

LIST OF FIGURES

Figure 1.1: Electrolytic Cell for PAA Production 18
Figure 1.2: Structure Model of PAA Film 21
Figure 1.3: Ionic Transports in PAA Barrier Oxide 25
Figure 1.4: Field-Assisted Dissolution of PAA 26
Figure 1.5: Steady-State Growth of PAA 29
Figure 2.1: Aluminum Film on Si_3N_4-Si Substrate 44
Figure 2.2: I-t Curve of Thin-Film Aluminum Anodization 47
Figure 2.3: PAA Surface as Anodized 50
Figure 2.4: Pore Widening by H_3PO_4 Etch 52
Figure 2.5: Pore Size versus H_3PO_4 Etch Time 54
Figure 2.6: Pore Uniformity versus H_3PO_4 Etch Time 55
Figure 2.7: Pore Distortion versus H_3PO_4 Etch Time 56
Figure 2.8: Cross Section of Thin-Film PAA 61
Figure 2.9: PAA Films Produced in Sulfuric Acid 63
Figure 2.10: PAA Films Produced in Oxalic Acid 64
Figure 2.11: PAA Films Produced in Phosphoric Acid 65
Figure 2.12: Inter-Pore Distance versus Anodizing Voltage 68
Figure 2.13: Anodization Rate versus Anodizing Voltage 69
Figure 2.14: Nanoparticles in PAA Pores 73
Figure 2.15: Low-Voltage PAA Thin Films (1) 75
Figure 2.16: Low-Voltage PAA Thin Films (2) 76
Figure 3.1: Fabrication of Partly Freestanding PAA 86
Figure 3.2: Fabrication of Fully Freestanding PAA by DLA 87
Figure 3.3: Fabrication of Partly Freestanding PAA by DLA 88

Figure 3.4: I-t Curves of DLA 89
Figure 3.5: SEM Image of Partly Freestanding PAA..... 91
Figure 3.6: Fully Freestanding PAA Films by DLA..... 94
Figure 3.7: Pattern Transfer by Freestanding PAA 96
Figure 3.8: SEM Images of Partly Freestanding PAA by DLA 99
Figure 4.1: SEM Images of Thin-Film PAA Filter..... 107
Figure 4.2: Molecular Indicators and Diffusion Device..... 108
Figure 4.3: Pore Size Distribution of PAA Filter..... 110
Figure 4.4: Diffusion Dynamics in PAA Pores 112
Figure 4.5: Charge Effects on Confined Diffusivity..... 115
Figure 5.1: Fabrication of MAM DNA Biosensor (1) 125
Figure 5.2: Fabrication of MAM DNA Biosensor (2) 126
Figure 5.3: I-t Curve of Time-Controlled Anodization 128
Figure 5.4: Surface Chemistry on MAM Structure 131
Figure 5.5: Optical Images of MAM Structure..... 137
Figure 5.6: SEM Images of MAM Structure..... 138
Figure 5.7: Structure Model of PAA Film in MAM 142
Figure 5.8: Circuit Model of MAM Structure 143
Figure 5.9: Impedance Spectrum of MAM DNA Biosensor (1) 145
Figure 5.10: Impedance Spectrum of MAM DNA Biosensor (2) 146
Figure 5.11: Impedance Spectrum of MAM DNA Biosensor (3) 147
Figure 5.12: Impedance Spectrum of MAM DNA Biosensor (4) 148
Figure 5.13: Impedance Spectrum of MAM DNA Biosensor (5) 149
Figure 5.14: Circuit Parameters of MAM Structure..... 151
Figure 6.1: Fabrication of $CD4^+$ Cell Biosensor..... 171
Figure 6.2: Top View of $CD4^+$ Cell Biosensor 172

Figure 6.3: Surface Chemistry on $CD4^+$ Cell Biosensor 175-176
Figure 6.4: Cell Capture on $CD4^+$ Cell Biosensor 178
Figure 6.5: Impedance Spectra of $CD4^+$ Cell Biosensor 179
Figure 6.6: Impedances Before and After Cell Capture..... 180
Figure 6.7: Impedance Change by Cell Capture 181
Figure 6.8: Counting Accuracy of $CD4^+$ Cell Biosensor 182

LIST OF TABLES

Table 4.1: Physical Properties of Molecular Indicators 113

Table 5.1: Circuit Parameters of MAM Structure 150

LIST OF ABBREVIATIONS

AFM:	atomic force microscopy
APTS:	(3-aminopropyl)trimethoxysilane
BAA:	barrier-type anodic alumina
CAD:	computer-aided design
C.E:	counter electrode
CMOS:	complementary metal oxide semiconductor
CV:	cyclic voltammetry
DIC:	differential interference contrast
DLA:	double-layer anodization
DNA:	deoxyribonucleic acid
dsDNA:	double-stranded deoxyribonucleic acid
EDAC:	*N*-(3-dimethylaminopropyl)-*N'*-ethylcarbodiimide hydrochloride
FBS:	fetal bovine serum
LPCVD:	low-pressure chemical vapor deposition
MAM:	metal-alumina-metal
MGO:	malachite green oxalate
MO:	methyl orange
MOSFET:	metal oxide semiconductor field-effect transistor
MPA:	3-mercaptopropionic acid
MUA:	11-mercaptoundecanoic acid
PAA:	porous anodic alumina, or porous-type anodic alumina
PBS:	phosphate buffered saline
PDMS:	polydimethylsiloxane

PECVD:	plasma enhanced chemical vapor deposition
R.E.:	reference electrode
RF:	radio frequency
SEM:	scanning electron microscopy
ssDNA:	single-stranded deoxyribonucleic acid
sulfo-NHS:	*N*-hydroxysulfosuccinimide sodium salt
W.E.:	working electrode
XPS:	X-ray photoelectron spectroscopy

CHAPTER 1

INTRODUCTION

1.1 Porous Anodic Alumina in Nanobiotechnology

1.1.1 Nanotechnology and Nanobiotechnology

The prefix "nano" means 10^{-9}. Nanotechnology refers to the control of matter at the scale of nanometer (nm), typically in the range of 1 to 100 nm. It involves the processes of inspecting, measuring, modeling, and manipulating matter at the nanometer scale. Nanotechnology is able to produce devices with smaller features than its predecessor, microtechnology, which has been the driving force for the rapid advances in information and communication systems within the past few decades. Photolithography has been able to continuously scale down the physical dimensions of microelectronic devices such as CMOS transistors, therefore achieving faster circuit speeds and higher packing densities. The exponential increase of the computing power, as described by Moore's Law, has introduced profound technological and social changes since the late 20^{th} century. In nanotechnology, photolithography in the enhanced forms such as immersion lithography enables semiconductor devices to continue to reduce their physical sizes, gaining a larger degree of the circuit integration. With the next-generation lithography, the size reduction will go further till it eventually reaches the resolution limit.

In addition to producing nanoelectronic devices, nanotechnology also involves controllable syntheses and manipulations of novel materials and structures at the nanoscale, such as nanowires and nanoparticles. Nanotechnology is fundamentally different from microtechnology because quantum mechanical phenomena that do not

show their effects at large dimensions start to be pronounced at the nanoscale. Nanomaterials often exhibit unusual physical properties compared to bulk materials. Therefore nanotechnology requires new understandings on the physical aspects and material attributes of nanoscale matters. With controllable manipulations of materials at the nano or even atomic level, nanotechnology opens the possibility of building functional systems in a "bottom-up" hierarchy, opposite to the conventional "top-down" approach. In other words, with nanotechnology high-level structures can be possibly constructed from the basic building blocks such as atoms and molecules.

Nanotechnology spans over a broad band of research disciplines, mainly involving physics, chemistry, electronics, material science, and biology. The interactions between biology and nanotechnology have shown to be an interesting research field in recent years. The terminology "nanobiotechnology", often used interchangeably with "bionanotechnology", is used to address the relation between biology and nanotechnology. The importance of this field can be interpreted in the following few aspects. First, many biological species (DNA, virus, protein, etc) have their physical sizes at the nanoscale, falling in the operational range of nanotechnology. Nanotechnology may be able to achieve the direct controls on individual biological molecules. Manipulations at the single-molecule level allow for fundamental understandings and bottom-level controls on biological processes and life activities. Second, biology provides good examples of molecular self-assembly. For instance, single-stranded DNA (ssDNA) nucleotides with complementary sequences hybridize, forming a Watson-Crick

double helix structure. Antibodies selectively bind with specific antigens based on their immune recognitions. In these biological systems, macromolecules are self assembled precisely and automatically, providing solid supports for the “bottom-up” approach. The supra-molecular chemistry in these systems serves as a possible mechanism for building complex structures from atomic or molecular elements. Last, nanotechnology provides a powerful system for developing nanoscale materials and devices for biological, medical and clinical applications. Several fields have been developed towards this direction, such as “Lab on a Chip”, which performs laboratory functions on miniaturized chip devices, “Nanomedicine”, which uses nanomaterials for medical applications such as molecular imaging and tissue repairing, and “Nanorobotics”, which develops nanoscale devices for clinical applications such as surgery, drug delivery, and biomedical instrumentation.

“Small things have big roles”. Providing so far the finest controls of materials and processes, nanotechnology serves as a universal platform with its applications widely spread in various fields such as information & communication, chemistry, medicine, environment, energy, heavy industry, and consumer goods. As it advances, nanotechnology is expected to bring more technical innovations in the future. Nanobiotechnology emphasizes on using nanotechnology to achieve biological tasks in better ways. In addition, it also studies biological materials and their operation mechanisms for the possible molecular nanotechnology in the future. It is considered as one of the most important research areas in the 21st century.

1.1.2 Nanomaterial: Porous Anodic Alumina

Anodic aluminum oxide (AAO), or anodic alumina, is formed by the electrolysis of aluminum. Its chemical form is Al_2O_3. Depending on the solubility of AAO in the electrolyte, AAO can be either non-porous barrier-type anodic alumina (BAA) or porous-type anodic alumina (PAA). PAA is well known for its unique nanoporous structure, which is featured with a hexagonal array of cylindrical alumina pores with a narrowly dispersed pore size.[1] Depending on the anodization conditions, the pore diameter ranges from sub-10 nm[2] to hundreds of nm.[3] From the material perspective, anodic alumina is a wide bandgap (6-11 eV)[4-6] insulator with a high dielectric constant (~8 for BAA and ~55 for PAA).[7-10] Mechanically PAA is very robust[11] and highly resistant to abrasions.[12] It also shows a great thermostability, having a melting temperature over 2000 °C.[13] Chemically PAA is inert to organic solvents and relatively stable in biological environments.

PAA has been studied for decades and has been widely used in the industries of dyeing, printing, and sealing.[12] In recent ~15 years, the nanoporous structure of PAA has been of increasing research interest to the field of micro/nanotechnology. Compared to the nanoscale features patterned by lithography, self-assembled PAA can be achieved from a relatively simple process while with good controls on the nanoporous structure. Therefore it has been a classic model for the non-lithography nanostructures. PAA has been used in numerous applications, generally through the following three mechanisms: (1) it is used as a host material for patterning nanoscale structures such as nanoparticles[14-16] and nanowires;[17-19] (2) it is used as a membrane

filter for nanoscale filtrations,[20-26] separations,[24,27-33] or controlled molecular releases;[34-36] (3) The large surface area of PAA is used in sensor applications.[37-39]

Section 1.2 is a literature review of nanoporous alumina, which provides more detailed information on the structure, fabrication, and material properties of PAA.

1.1.3 Porous Anodic Alumina in Nanobiotechnology

This subsection reviews pervious works related with the use of PAA in molecular transports and biosensing applications. In the next subsection, the motivation and the focus of this dissertation are presented, and the topic of each following chapter is outlined.

(1) PAA for Molecular Transports

The term "molecular transports" here means any applications that involve passing molecules through alumina nanopores, such as filtrations, separations, and controlled molecular releases.

PAA has been investigated as a membrane filter in gas filtrations[2,20,23-25], because of its potentially important applications in the energy industry. In nanobiotechnology, PAA is more often used for molecular separations in the liquid phase. As an inorganic synthetic membrane, PAA has advantages over other porous materials such as polymeric and biological membranes. PAA has excellent mechanical robustness and thermal stability, being able to sustain in a wide range of physical conditions. PAA has a well-defined porous structure with a narrow pore-size distribution. This size uniformity is favorable for achieving size-exclusion separations with sharp cut-offs. The oxide

nature of PAA allows chemical modifications on the surface, providing the possibilities of anchoring chemical or biological molecules on the PAA surface.

Lee et al.[29] demonstrated a separation of enantiomeric drugs on an antibody-coated PAA membrane. In their work, the sidewalls of the alumina pores were deposited with a thin silica film using the sol-gel method. The alumina pores were then treated with the aldehyde-terminated silane and further coated with antibody proteins through the aldehyde-amine reaction. The antibody used was chirality specific, being able to selectively bind with the RS type of the drug enantiomers but not with the SR type. When the mixture of the drug enantiomers diffused through the antibody-coated alumina pores, they were separated based on their chiralities, having the RS type captured on the alumina sidewalls whereas the SR type passed through the alumina pores. A similar approach was adopted by Vlassiouk et al.[31] to achieve the separation of DNA oligonucleotides on a PAA membrane. In their method, the alumina sidewalls were chemically attached with the ssDNA oligonucleotides using amino-silane and glutaraldehyde. Complementary DNA oligonucleotides passing through the alumina pores were captured on the sidewalls by the DNA hybridization. Non-complementary DNA molecules flowed through the pores without being captured. In these applications, the molecular transports through the alumina pores were driven by diffusion. Recently, Cheow et al.[33] demonstrated using an electric field as the driving force to separate the electrically charged proteins such as bovine serum albumin, lysozyme, and myoglobin. In their method, the PAA membrane was

coated with platinum on both sides, serving as two electrodes across which a dc bias was applied to drag the charged proteins through the alumina pores. The approach was advantageous for achieving a high electric field across the PAA membrane with a relatively low voltage. Sano et al.[40] demonstrated a chromatographic separation of DNA molecules on a PAA membrane. Instead of transporting through the alumina pores, DNA molecules flowed through a microfluidic channel, passing over the surface of the PAA membrane underneath the channel. The alumina pores served as the nanoscale traps for differentiating the migration speed of the DNA molecules with different sizes. Large DNA molecules passed along the surface relatively smoothly whereas smaller DNAs were trapped more frequently by the alumina pores, therefore traveling relatively slower.

Besides molecular separations, PAA has also been used for controlled molecular releases. Molecules passing through alumina pores are subject to the physical confinements from the nanoscale pore channels, especially when the molecular size is comparable to the channel diameter. Controlled molecular release is of great interest because its importance for applications such as drug delivery and cell culture. Gong et al.[34] investigated the diffusions of fluorescein (MW=400 Da) and FITC-dextran conjugates (MW=4-150 kDa) through some tubular alumina capsules with the pore size ranging between 25 nm and 55 nm. Their experiments showed that the speed of molecular diffusions through the alumina pores could be controlled by the pore size. The diffusion rate of the fluorescein was increased by ~7 times when the pore size increased from 25 nm to 55 nm. For the dextran

conjugates, the transport exhibited a hindered Knudsen-type diffusion, due to their large hydrodynamic molecular size. Larger dextran molecules diffused through the alumina pores with a slower rate. Molecules larger than 70 kDa showed no detectable diffusions through the 55-nm pores. A similar dependence of the diffusion rate upon the pore size was observed by Kipke and Shimid,[35] who diffused crystal violet (MW=373 Da) through the alumina pores with a pore size of 20-200 nm. The crystal violet molecules were encapsulated in the micelles of sodium dodecylsulfate (MW=288 Da) in order to increase the molecular size to enhance the hindering effects from the pore walls. In the experiments by Hohlbein et al.,[36] the diffusions of fluorescent molecules such as enhanced green fluorescent protein (MW~27 kDa) and Alexa Fluor 488 through the alumina pores with a diameter of 35-40 nm were monitored by fluorescence correlation microscopy. It was observed that the diffusion of the probe molecules in the alumina pores was up to 19 times slower than that in the bulk solution. Takoh et al.[41] used a PAA as a porous membrane support for the application in cell culture. Hela cells were cultured on one side of the PAA while the stimulating chemical (ethanol) was supplied from the other side of the membrane. A local stimulation was achieved by lithographically patterning the PAA membrane.

(2) PAA for Biosensors

Currently an interesting subdivision of PAA applications is to utilize the nanoporous structure of PAA to develop sensor systems for detecting biological molecules such as DNAs and proteins.

For DNA biosensors based on PAA, the biological event mostly used

as the detection target is the DNA hybridization. Usually ssDNA nucleotides are immobilized on alumina pore walls through chemical crosslinking methods. DNA nucleotides with a complementary sequence passing through the alumina pores hybridize with the anchored DNA molecules. Optical and electrical methods are commonly used for the detection of the hybridization event. In the work by Vlassiouk et al.,[31] the alumina pore walls were coated with 21-mer or 41-mer ssDNAs through the crosslinking system of amino-silane and glutaraldehyde. The hybridization with the complementary DNAs was directly detected by measuring the UV and IR absorption spectra. The optical absorbance in these regions increased after the hybridization process. The surface density of the bound DNA molecules was on the order of 10^{12} cm^{-2}, and the hybridization efficiency was ~70%. In the method by Matsumoto et al.,[42] ssDNA molecules were labeled with fluorescent Cy2 or Cy3 dyes, and the hybridization was detected by fluorescence microscopy. DNA molecules fixed in the alumina pores with an inter-pore distance larger than 400 nm were able to be resolved as individual bright spots under the fluorescence microscope. A similar detection approach of using fluorescent dyes was reported by Cloutier et al.,[43] who utilized the intercalation of fluorescent TOTO-1 dyes with DNA molecules.

Besides optical methods, the DNA hybridization in alumina pores can also be detected by electrical measurements. Steinle et al.[44] reported that alumina pores could serve as ion channels with a switchable gate controlled by the alumina surface hydrophilicity. When modified with a hydrophobic C_{18} silane layer the PAA membrane

prevented water and ions ($Ru(bpy)_3^{2+}$) from passing through the alumina pores. The gate could be switched on by the addition of hydrophobic ions (dodecylbenzene sulfonate) to a sufficiently high concentration. Vlassiouk et al.[45] monitored the DNA hybridization on the PAA sidewalls by measuring the ionic conductance through the alumina pores, using cyclic voltammetry, dc time course, and impedance microscopy. The hybridization of 21-mer DNAs in the 20-200-nm alumina pores was shown to be accompanied with an increase of the ionic resistance. A theoretical limit of the detection of the complementary DNA molecules was estimated to be 10^{-17} mol. In the work by Takmakov et al.,[46] alumina pores were hydrothermally shrunk to a smaller size (less than 10 nm) to enhance the effects of the DNA hybridization on the ionic conductance through the alumina pores. Besides the DNA hybridization, PAA has also been used for analyzing other DNA events, for example, chromosome dissection.[47]

In parallel with DNA biosensors, protein biosensors have been developed based on PAA membranes. Kang et al.[48] reported a 3D microwell array, in which a PAA membrane was used as the porous substrate for enhancing the capture capacity of antigen proteins on the surface. Takmakov et al.[49] used PAA membranes to detect the streptavidin-biotin binding in the alumina pores by fluorescence microscopy. The optical intensity was enhanced by a factor of 7, compared to the flat glass substrates. Darder et al.[50] used PAA membranes as a porous matrix for hosting glucose oxidase with retained enzyme activities. In these applications, PAA showed its advantages in achieving the high density of the protein binding sites

because of its porous structure and the large surface area.

In the applications introduced above, PAA was directly used as a core material for transporting molecules or sensing biological species. In addition, PAA has also been used as a template for constructing nanoscale biological structures such as DNA nanotubes[51] and protein nanotubes.[52]

1.1.4 Motivation and Focus of Dissertation

As introduced in the previous subsection, PAA has been of great interest to nanobiotechnology. Its unique nanoporous structure is being utilized for various applications. In the following paragraphs, several considerations regarding the future applications of PAA membranes in nanobiotechnology are presented:

(1) Thin-film PAA

For nanobiotechnology applications, the integration of PAA with nanofabricated devices is important. Compared to the conventional technologies, miniaturized systems made by nanotechnology are advantageous in many aspects for solving biological problems, such as the fabrication cost, sample consumption, analysis speed, and device portability. In addition, nanoscale devices can be integrated with electronic circuits, achieving automatic controls by computer systems. In nanofabrication, metal films at the micrometer scale or less can be easily fabricated by the evaporation or sputtering process. The natural integration of PAA as a component in nanoscale devices can be achieved by anodizing pre-deposited aluminum thin films on solid substrates such as silicon and oxides (e.g. SiO_2 and Si_3N_4). In previous

reports, however, thick PAA membranes have been widely used, probably because of researchers' limited access to nanofabrication facilities and/or the availability of commercial PAA membranes. These stand-alone membranes usually range from tens[53,54] to hundreds[3,55-60] of μm in thickness. From the viewpoint of the device miniaturization, thin-film PAAs on solid substrates represents a more promising direction for future applications in nanobiotechnology.

(2) Freestanding PAA with Open Pores

Usually PAA is firmly attached to its substrate after the anodization process. A U-shaped oxide barrier is formed at the pore bottoms.[61] However, for applications such as filtration, separation, and controlled molecular release, freestanding PAA films with through holes are necessary. The barrier oxide needs to be removed to open the alumina pores. Several methods, including chemical dissolution,[1] voltage reduction,[62] voltage pulse,[2,63] and voltage reversal,[64] have been developed to strip PAA films off their supporting substrates. These methods, however, can only produce stand-alone freestanding PAAs.

For on-chip PAA thin films, a local freestanding structure with through pores is essential for any chip systems that involve nanofluidics in PAA pores. Fabricating such a structure remains as a challenge due to the difficulties of removing the barrier oxide while keeping the PAA film freestanding on the substrate. To realize practical thin-film PAA chip devices for applications such as biomolecular separations, approaches of fabricating local freestanding PAA films on chip remain to be explored.

(3) Dynamics of Molecular Transport in PAA

As reviewed previously, many biological applications involve passing molecules through alumina pores. Molecular transports confined in such small channels are significantly different from those in the bulk solution. Macroscopic physics often cannot precisely describe the behaviors of fluid in nanopores. The complexity is believed to arise from the small-scale effects such as the solid surface charges[65] and the inhomogeneous liquid properties.[66,67] In general, molecular transports through nanopores have not been fully understood and still remains largely unexplored. Because of its well-defined porous structure, PAA provides an ideal structure model for experimenting the confined molecular transports in nanopores. However, although many papers have utilized PAA membranes in the applications of molecular transports, the reports focused on studying the transport dynamics are limited.[68-70] Characterizing the dynamics of molecular transports in PAA nanopores is important not only for understanding the fundamentals of nanoscale physics, but also for developing PAA-based nanofluidic systems.

The main topic of this dissertation is focused on fabricating chip-based PAA thin films, with an orientation toward developing nanoscale PAA-on-chip systems for biological applications, such as molecular separations and biosensors. With the considerations presented above, the topics of Chapter.2-5 are outlined as follows:

Chapter.2:

This chapter presents the fabrication and characterization of micrometer-thin PAA films based on silicon substrates. The topics

include: the supporting substrates for the PAA thin films, the preparation of aluminum thin films, the thin-film anodization, the surface characteristics of PAA films as anodized, the pore widening process, the cross section of PAA thin films, the anodization conditions, the nanoparticle growth in PAA thin films, and low-voltage PAA thin films.

Chapter.3:

This chapter focuses on the development of new approaches for fabricating freestanding PAA thin films with through pores. Two methods are presented. In the first method, a PAA thin film was fabricated on a Si_3N_4-coated silicon substrate. A partly freestanding structure was achieved by removing the supporting silicon substrate using KOH anisotropic etch. The second method, named as "double-layer anodization" (DLA), was developed for fabricating partly or fully freestanding PAA thin films by utilizing a sacrificial metal layer (SML), which was inserted between the supporting substrate and the aluminum film. The anodization of the SML layer automatically detached the top PAA film from the substrate.

Chapter.4:

This chapter investigates the confined diffusion of small (sub 1000 Da) organic molecules in alumina nanopores. The diffusion system was built upon a silicon-based micrometer-thin partly freestanding PAA membrane. The molecular diffusion course was recorded by monitoring the optical absorbances of the diffused molecules. The porous geometry of the PAA filter was characterized, base on which the diffusion was modeled as one-dimensional Fickian flow confined in

nanoscale space. The characteristic parameter of the diffusion process, diffusion coefficient, was calculated from the physical model. The diffusion behaviors in the alumina nanopores are discussed in details.

Chapter.5:

In this chapter, a novel DNA biosensor utilizing the large surface area of PAA films has been developed. The device was based on a metal-alumina-metal (MAM) sandwich structure. The top and bottom metal films served as two electrodes whereas the middle PAA membrane served as a porous dielectric layer. ssDNA oligonucleotides were attached to the sidewalls of the alumina pores through chemical crosslinkings. The DNA hybridization was sensed by measuring the impedance spectrum between the two electrodes.

Chapter.6

A second part of this dissertation is the research of cell biosensors for the precise quantification of the $CD4^+$ cells in human blood, orientated for the development of affordable point-of-care diagnostic tools for quantitatively analyzing the infection status of AIDS patients. With this motivation, an impedance biosensor with a single-cell detection resolution has been developed, which was featured with a dense array of microscale working electrode. The electrode surfaces were chemically modified to be able to selectively capture $CD4^+$ cells. Each electrode was comparable to a $CD4^+$ cell in size, being able to individually sense one single cell in a binary mode. With this biosensor, the detection of $CD4^+$ cells at the single-cell resolution while independent of the dynamic range of the cell concentration was demonstrated. Details of this work are presented in Chapter.6.

1.2 Review of Porous Anodic Alumina

1.2.1 Anodization Process

Anodic alumina is produced by anodizing aluminum in an electrolytic cell. The anodization is essentially an electrochemical process that oxidizes aluminum to alumina through redox reactions. Figure 1.1 shows the schematic of a typical electrolytic cell for the aluminum anodization. The cell consists of an external power source, two electrodes (anode and cathode), and a bath container filled with the electrolyte solution.

The nature of the electrolyte has significant influences on the alumina formation. In general, for the electrolytes in which alumina is insoluble, the formed alumina film is relatively uniform and compact, having a nonporous structure. This type of alumina is referred as barrier-type anodic alumina (BAA), and the electrolytes generating BAA are referred as barrier-type electrolytes. Examples include neutral boric acid, ammonium borate or tartrate aqueous solution (pH 5-7), as well as organic acids such as borate, tartrate, citric, malic, and glycollic acids.[12] For the electrolytes in which alumina is slightly soluble, the formed alumina films have a porous structure. This type of alumina is referred as porous-type anodic alumina, or porous anodic alumina (PAA). Popular porous-type electrolytes include sulfuric acid (H_2SO_4), oxalic acid ($C_2H_2O_4$), and phosphoric acid (H_3PO_4).[71] This dissertation focuses on the porous-type alumina thin films only. Unless specified explicitly, all the alumina films discussed in the following chapters refer to the porous-type anodic alumina.

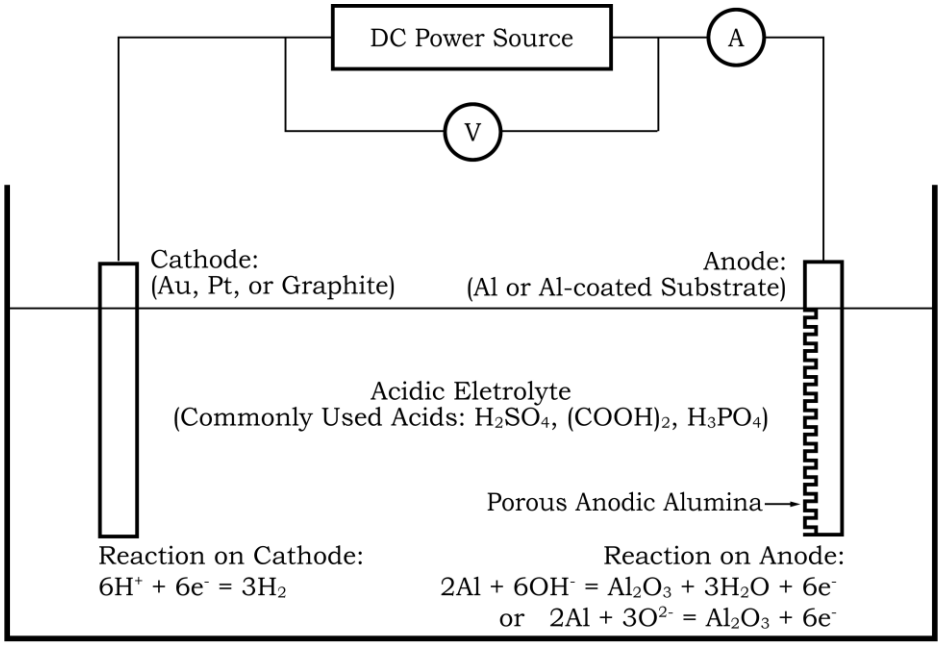

Figure 1.1. Electrolytic Cell for PAA Production. The cell consists of a power source, two electrodes (cathode and anode), and an electrolytic bath. Aluminum source is on the anode, immersed in the electrolyte. Powered by a dc voltage or current, the aluminum source is oxidized to alumina in the electrolyte through the redox reactions occurred on the two electrodes. Common electrolytes for the PAA production are sulfuric acid (H_2SO_4), oxalic acid ($C_2H_2O_4$), and phosphoric acid (H_3PO_4).

The aluminum substrate is prepared on the anode and immersed in the electrolyte. The aluminum source is usually a bulk metal or a solid substrate coated with a thin aluminum film. The purity and the surface flatness of the aluminum source are important for achieving a homogeneous porous structure. Under a positive bias, Al atoms are oxidized to Al^{3+} and react with the oxygen-containing anions (OH^- and O^{2-}) from the electrolyte, forming an alumina film on the top of the aluminum substrate. The oxidation reaction on the anode is expressed as follows:

$$2Al^{3+} + 6OH^- = Al_2O_3 + 3H_2O \quad (1.1)$$

or

$$2Al^{3+} + 3O^{2-} = Al_2O_3 \quad (1.2)$$

On the other hand, the cathode drains the current from the anode, having the following reduction reaction:

$$2H^+ + 2e^- = H_2 \quad (1.3)$$

Gold, platinum, and graphite are commonly used materials for the cathode because of their chemical stability.

Essentially the redox reactions produce Al_2O_3 and H_2, consuming Al and H_2O. The external power source provides energy for activating the redox reactions. Based on the electric output, the anodization can run in two different modes, the constant-voltage mode and the constant-current mode. In the first mode, the power source applies a constant voltage across the electrolytic cell whereas the current is subject to the resistance of the electrolytic cell. In the second mode, the power

supply outputs a constant current through the cell while the voltage is dependent on the cell resistance. For the process control, the electric characteristics (V-t and I-t curves) during the anodization are usually monitored in real time.

1.2.2 Porous Structure

The porous structure of PAA was unknown prior to 1930s. Early researchers,[72-74] motivated by the rectifying effects of aluminum, proposed several theories to explain the PAA formation. The porous nature of PAA was first suggested by Setoh et al.,[75] based on their electric characterizations. Using the optical and electron microscopes, Keller et al.[76] inspected the microscopic structure of the PAA films and modeled it as a hexagonal array of cylindrical pores in their paper published in 1953. Over decades their proposal has been proven to be essentially true and served as a classic model for the PAA structure.

In their model, shown as Figure 1.2, the PAA formed on the top of the aluminum substrate consists of numerous cylindrical pores that are densely packed as a hexagonal array, presenting a honeybee comb structure. The primary unit of this porous structure is defined as a pore cell. Each pore cell is a hexagonal tube with a cylindrical hollow (pore) in the center. The bottom of the pore cell is closed by a thin barrier oxide layer in a “U” shape.

Ideally all the alumina pores are cylindrical, having an identical pore size. Each pore is surrounded by six other pores that are evenly distributed around, with an equivalent inter-pore distance. The inter-pore distance and the pore diameter are dependent on the anodization conditions, primarily on the anodizing voltage (or the current density).

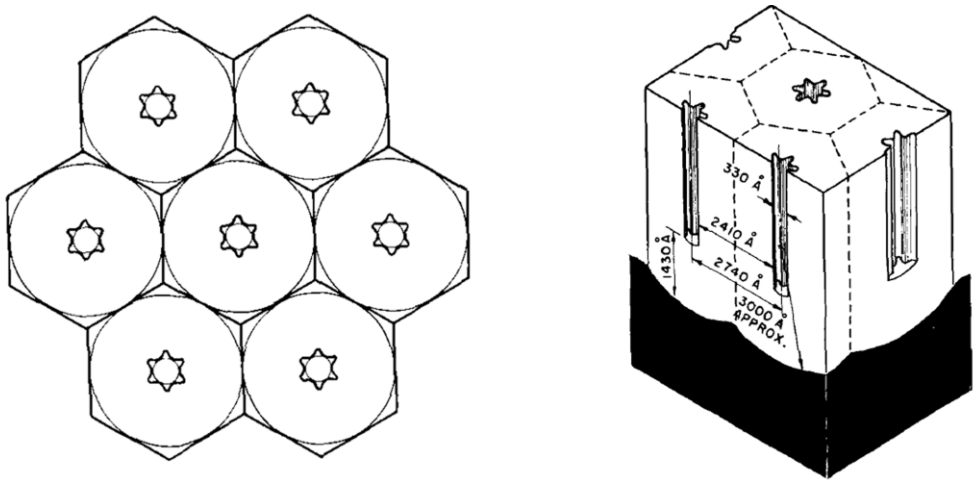

Figure 1.2. Structure Model of PAA Film. (A) The top view of the PAA film. (B) The cross-sectional view of the PAA film. The PAA film consists of a hexagonal array of cylindrical pores, with a thin barrier oxide layer at the pore bottoms. The model was first proposed by Keller et al..[76] Although the six-point-star pore feature is unnecessary, the overall structure has been proven by numerous experiments to be essentially true.

With the other anodization conditions the same, the inter-pore distance and the pore diameter are linearly proportional to the anodizing voltage or the current density.[3,76-80]. In other words, lower voltage or current density produces smaller pores with a higher packing density, whereas higher voltage or current density generates larger pores with a lower packing density. Practically the pore diameter varies from sub-10 nm[2] to hundreds of nm,[3] with a packing density up to 10^{12} cm^{-2}.

Figure 1.2 (B) shows the cross section of the PAA film. The pores originate at the top surface of the aluminum substrate and terminate at the alumina-metal interface. The straight pores are parallel to each other, being perpendicular to the substrate. In the anodization, the alumina pores are the channels through which the oxygen-containing anions transport from the electrolyte to the pore bottoms where the aluminum substrate is oxidized to alumina. The pore length, i.e., the PAA film thickness, is primarily determined by the anodizing time. Longer anodization consumes more aluminum, producing thicker alumina film and longer pores. PAA films as thick as a few hundred μm can be achieved. The straight pore profile together with its high aspect ratio makes PAA unique among all the porous membranes.

There exists a thin barrier oxide in a scallop shape at the bottom of each alumina pore.[61] During the anodization this barrier oxide layer is under a high electric field (~10^7 V cm^{-1})[81], serving as an active frontier where aluminum is oxidized to alumina. The thickness of the barrier oxide is correlated to the pore diameter and the inter-pore distance.

1.2.3 Formation Mechanism

Significant research efforts have been made to unveil the PAA formation, such as the investigation of the morphology and formation mechanism by O'Sullivan and Wood,[82] the theoretical modeling of the pore structure by Parkhutik and Shershulsky,[83] and the kinetics study of the pore growth by Patermarakis et al.[84-97] To date, it has been generally accepted that the PAA formation consists of three stages:[12,81-83,98] (1) the barrier-type oxide growth; (2) the pore initiation; (3) the steady-state anodization.

(1) Barrier-Type Oxide Growth

Immediately after the anodization starts, the electrochemical oxidation takes place on the anode, forming a thin alumina film on the substrate. This alumina thin film is uniform and non-porous. As it grows thicker, it presents a higher electric resistance. The increase of the resistance results in a current decrease in the constant-voltage anodization mode, or a voltage increase in the constant-current mode. This alumina thin film is essentially a barrier-type oxide. Therefore this stage is referred as the barrier-type oxide growth.

(2) Pore Initiation

Once the barrier oxide is formed, the aluminum substrate loses the direct contact with the electrolyte. The further anodization requires the cations and anions to penetrate into the barrier oxide, in order to form Al_2O_3. The Al^{3+} cations migrate from the metal-oxide interface towards the electrolyte-oxide interface, whereas the OH^- and O^{2-} anions migrate in the opposite direction. The migrations are driven by the electric field across the barrier oxide. Figure 1.3 shows the ionic transports across

the barrier oxide during the anodization.

In the porous-type electrolytes such as sulfuric acid, oxalic acid, and phosphoric acid, the growth of the barrier-type oxide only lasts for a short period at the very beginning of the anodization. As the process continues, the barrier oxide film turns quickly into a porous structure, essentially because alumina is soluble in these acidic electrolytes. The barrier oxide is subject to the electrolytic dissolution immediately after its formation. Instead of a pure chemical dissolution, the electrolytic etch is accelerated by the high electric field across the barrier oxide layer.[99] The schematic of the field-assisted dissolution is shown in Figure 1.4. The electric field polarizes the Al-O bonds on the barrier oxide surface by pushing the Al^{3+} ions away from the lattice and pulling the O^{2-} ions towards inside. The Al-O bonds are further weaken by the hydrogen bonds occurred on the O^{2-} ions and the hydration on the Al^{3+} ions. Eventually the Al-O bonds dissociate, generating $Al(H_2O)_6^{3+}$ and H_2O.

The pore initiation starts with the local penetration of the electrolyte ions into the barrier oxide layer. The electrolyte ions have a relatively faster etch rate at certain local sites, probably due to the metal surface conditions, such as the grain structure and the material impurity. The preferred etch at these local sites results in many fine paths into the barrier oxide layer. These paths are the precursors of the final alumina pores. At the bottom of these paths, the anodizing voltage drops across a very thin barrier oxide layer, leading to a high electric field. From the metal-oxide interface to the oxide-electrolyte interface, the electric field is further concentrated because of the

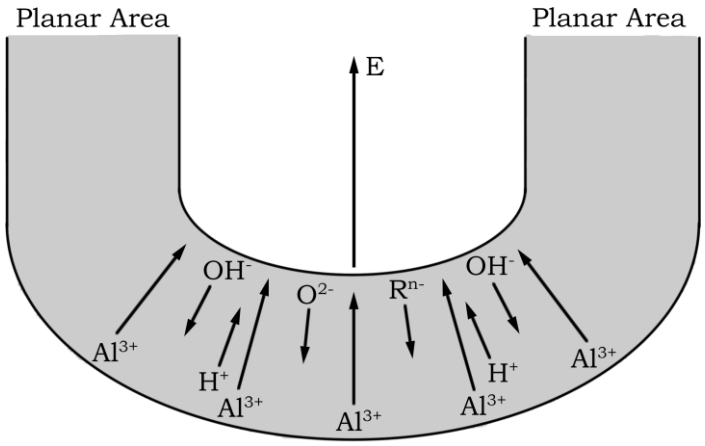

Figure 1.3. Ionic Transports in PAA Barrier Oxide. Under a high electric field across the barrier oxide, Al^{3+} cations migrate from the Al-Al_2O_3 interface to the Al_2O_3-electrolyte interface. H^+ ions generated within the barrier oxide move in the same direction. OH^-, O^{2-} and electrolytic anions (R^{n-}) move from the Al_2O_3-electrolyte interface towards the opposite direction. The electric field is high because of the thin barrier oxide. In the planar areas, the electric field is low as the alumina film in those regions is much thicker.

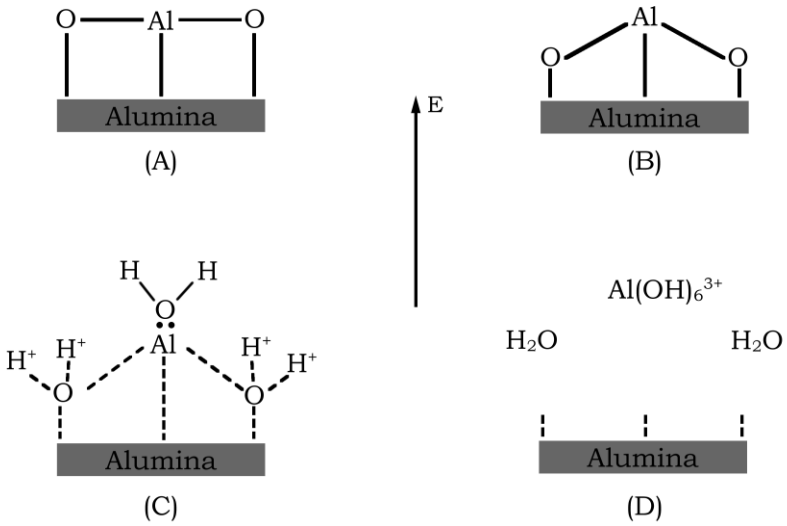

Figure 1.4. Field-Assisted Dissolution of PAA.[82] (A) Normal Al-O bonds at the PAA surface. (B) The Al-O bonds polarized under a high electric field. (C) The hydrogen bonding on polarized oxygen atoms ($O^{\sigma-}$) and the hydration on polarized Al atoms ($Al^{\sigma+}$). (D) The dissociation of Al-O bonds, generating $Al(OH)_6^{3+}$ and H_2O.

scallop shape of the barrier oxide layer. Therefore the aluminum oxidation and the alumina dissolution at the pore bottoms are much faster than in the planar areas due to the field-acceleration effect. In the planar non-porous areas, the alumina layer is much thicker than the barrier oxide at the pore bottoms. The electric field is evenly distributed with a much smaller magnitude. The field-assisted migration through these areas is negligible and the alumina dissolution is the chemical dissolution only. Therefore the further anodization preferably propagates along the existing paths, finally reaching a steady-state pore growth.

(3) Steady-State Growth:

After the pores are initialized, two competing processes, the aluminum oxidation and the alumina dissolution, take place simultaneously at the pore bottoms. New alumina generates within the barrier oxide layer whereas old alumina at the oxide-electrolyte interface dissolves into the electrolyte. Both processes are accelerated by the high electric field. When they reach a dynamic equilibrium, a steady-state anodization is established (Figure 1.5 (A)). After that, the aluminum-oxide and the oxide-electrolyte interfaces move downwards with the same speed. The thickness of the barrier oxide stays unchanged.

Aluminum has a density of 2700 kg m^{-3}. If assuming anodic alumina has a same density as other alumina types (4000 kg m^{-3}), the aluminum-to-alumina conversion comes with a volume expansion by a factor of ~1.3. As shown in Figure 1.5 (B), the newly formed oxide tends to expand around the pore bottoms (arch arrows), presenting a

repulsive force[57] (F and F') to their neighbor pores. This repulsive force plays critical roles in the pore growth during the anodization.

Ideally, all the pores are arranged in a hexagonal array, being separated evenly. The repulsive forces between adjacent pores are of the same magnitude and cancel each other in the lateral direction ($F_{\square}$ and $F_{\square}'$). Since the pores are initialized on the surface in a random manner, the inter-pore distances are not necessarily identical. Instead, they may vary from pore to pore. If two adjacent pores are separated farther than average, the barrier oxide between these two pores is relatively thicker. The corresponding electric field is lower. Therefore the field-assisted oxidation and dissolution are both slower. The alumina formation is also slower than average, producing a smaller repulsive force. The two pore bottoms are pushed closer by the surrounding pores. On the other hand, if two adjacent pores are closer than average, the barrier oxide between them is thinner, resulting in a higher electric field. Thus the oxidation in this region is faster, generating more alumina in a limited space, which pushes the pore bottoms away from each other. For this reason, the repulsive force essentially serves as a negative feedback to automatically adjust the inter-pore distances, rearranging the pore positions from a random manner toward the regular hexagonal pattern.

In the vertical direction, the components of the adjacent repulsive forces are accumulated as they all point to the same direction. This vertical force pushes the alumina sidewalls upwards, contributing to the formation of the straight channel profile of the alumina pores in the vertical direction.

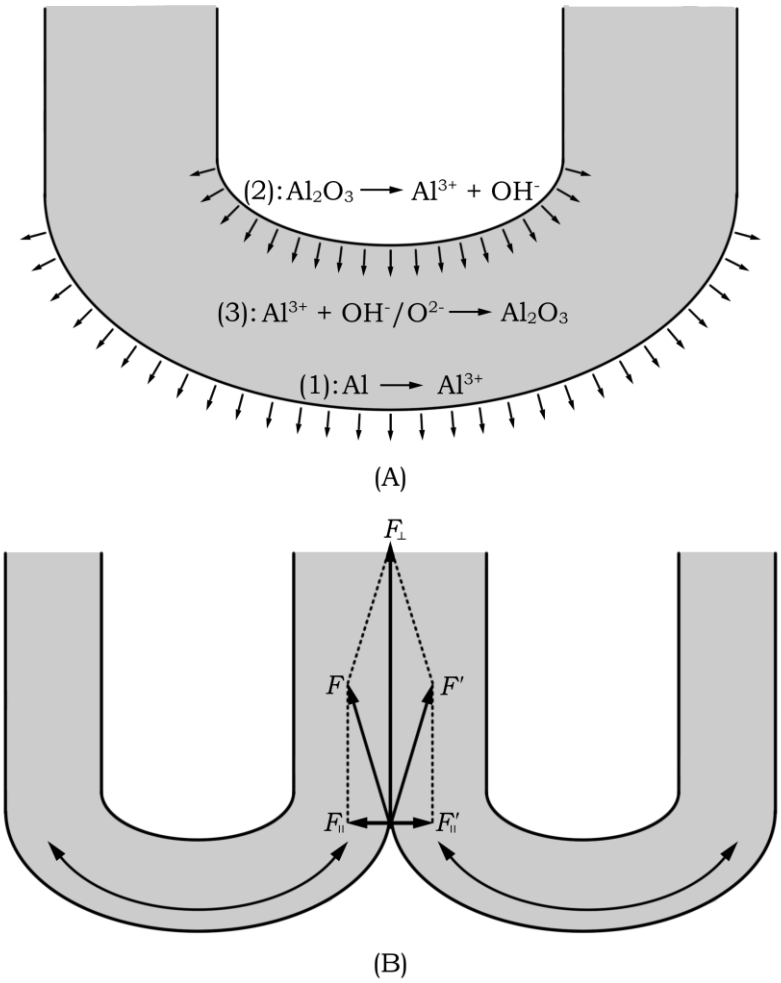

Figure 1.5. Steady-State Growth of PAA. (A) The steady-state growth at the pore bottom, with two competing processes: (1) the field-assisted aluminum oxidation at the Al-Al_2O_3 interface (2) the field-assisted alumina dissolution at the Al_2O_3-electrolyte interface. Alumina forms in between the two boundaries (3). (B) The repulsive forces in the volume expansion. At the pore bottoms, alumina tends to expand around (arch arrows), due to the volume expansion in the Al-to-Al_2O_3 conversion. F and F' are the repulsive forces between the adjacent pores. The vertical components of the forces are accumulated as $F_\perp$, contributing to the growth of the straight pores. The lateral components, $F_\parallel$ and $F_\parallel'$, are responsible for the self arrangement of the porous structure toward the ideal hexagonal pattern.

1.2.4 Anodization Conditions

PAA film has a uniform porous structure. The uniformity is reflected by the homogenous distributions of the inter-pore distance and the pore diameter, as well as the identical film thickness over the entire substrate surface. The well-defined porous structure is primarily controlled by the anodization conditions, including (1) the anodizing voltage or current density (2) the electrolyte type and concentration (3) the anodizing time (4) the temperature.

(1) Anodization Voltage/Current

In the aluminum anodization, the dc voltage (current) output provides energy for activating the redox reactions on the anode and cathode. The pore growth rate is correlated to the area density of the electrons generated from the Al-to-Al^{3+} conversion in unit time, which is essentially the current density. In experiments, the constant-voltage mode enjoys a technical convenience because in this mode the steady-state current density stays independent of the sample area. In other words, samples with arbitrary processing areas have the same pore growth rate and pore geometry as long as they are anodized under the same voltage. For this reason, all the anodization processes in this dissertation were performed under the constant-voltage mode. Future discussions by default refer to this mode.

The most important correlation between the anodizing voltage and the pore geometry is that, the pore dimension (l), expressed either in the inter-pore distance or the pore diameter, is linearly proportional to the anodizing voltage:

$$l = kU + c \tag{1.4}$$

Where U is the anodizing voltage; and k and c are the relation coefficients. This linear dependence has been proven to be valid by many experiments.[3,76-80] The importance of this relation is that the nanoscale features of PAA films can be controlled by a simple macroscopic condition.

(2) Electrolyte

The nature of the electrolyte has significant influences on the morphology of PAA films. The commonly used porous-type electrolytes include sulfuric acid, oxalic acid, and phosphoric acid. Sulfuric acid is a strong acid, often used for producing relatively small alumina pores at low anodizing voltages. For 0.3 M sulfuric acid, the inter-pore distance was ~50 nm with a voltage bias of 20-25 V.[3] Commonly used concentrations were 15% (w/v),[76,100-104] 20% (w/v),[57,77,80,105] and 0.3 M.[3,55,106-108] Other concentrations such as 10%,[109] 17.5%,[110] 1.5 M[111] and 2.5 M[112] were occasionally seen in reports. Commonly used voltages ranged from 15 V to 30 V,[57,76,80,108,109], typically at 25 V.[3,55,105,107] A higher voltage of 40 V was also reported.[104] Oxalic acid is suitable for fabricating alumina pores with a medium size. For 0.3 M $C_2H_2O_4$ the inter-pore distance was 80-150 nm with a voltage bias of 25-60 V.[3] Typical settings were 0.3 M in concentration with 40 V in voltage,[1,3,53,56-58,108,113-116] and 0.04-0.05 M with 60-80 V.[53,54,116] Other conditions such as 2-3% (w/v),[76,117] 0.5-0.6 M[54,104,106,118] in concentration, and 20-25 V[76,107] in voltage were also reported. Phosphoric acid is usually used for producing alumina with large pores. For 10% phosphoric acid, the inter-pore distance was 300-450 nm with a voltage bias of 100-160 V.[3] Typical concentrations were 4%

(v/v)[76,117,119] and 10% (v/v).[3,106] The typical voltage ranged from 80 V to 200 V,[3,59,61,106,108,116] while voltages as low as 20 V[76] or as high as 270 V[78] were also seen in reports.

Besides these three major electrolytes, other acids were also used for the PAA production, such as chromic acid[76,119] and malonic acid.[120] The electrolyte could also be a mixture of multiple acids such as sulfuric acid and oxalic acid.[121,122]

(3) Temperature

Temperature affects the anodization rate. High temperature provides additional thermal energy for activating the redox reactions, therefore enhancing the rates of both the aluminum anodization and the alumina dissolution. Maintaining a constant temperature is important for getting uniform PAA films. In the investigation by Hunter and Fowle,[100] the current density in 15% sulfuric acid with a 10-volt bias was enhanced from ~2 A ft^{-2} up to 60 A ft^{-2} when temperature increased from 50 °F to 160 °F. The dissolution rate was doubled for every 8.6 °C increase, and was increased tenfold for every 28.3 °C increase. The unit barrier oxide thickness (in Å V^{-1}) stayed relatively constant. Among the major reports, several temperatures were routinely used by researchers such as 20-25 °C,[76,77,108,112] 17 °C,[54,107,116,123] 10 °C[3,55,76,106], and 0-5 °C,[3,55-58,106,115,118]

(4) Anodizing Time

Depending on the PAA thickness, the anodizing time varies from minutes for ultrathin PAA films,[124] up to days for very thick films.[56,57] Under the same anodization conditions, longer anodization produces slightly larger pores because the pore walls are subject to a

longer dissolution in the electrolyte. More importantly, longer anodization is more favorable for producing an ordered porous structure because PAA membranes undergo a longer self arrangement, adjusting the pores from random positions to a hexagonal pattern.

1.2.5 Pattern Regularity

Highly ordered PAAs have an elegant hexagonal pore array, often desired in many applications for its pattern regularity and identical pore sizes. Although the alumina structure has now been clear and much consensus has been reached regarding its formation mechanism, there have not been any theoretical models that can describe the dependence of the pattern regularity upon the anodization conditions. Explorations of the optimal conditions for ordered PAAs basically rely on experiments. In the reported articles, the anodization conditions vary in many aspects such as the sample preparation, anodizing mode, electrolyte selection, operation temperature, etc. Several condition sets, such as 0.3 M sulfuric acid at 25 V, 0.3 M oxalic acid at 40 V, and 10% phosphoric acid at 160 V, were reported to be favorable for obtaining ordered PAA structures.[3] As explained previously, a long-time anodization is generally favorable in fabricating ordered PAA films because it allows better structure rearrangement.

Besides tuning anodization conditions, other approaches have been proposed to achieve ordered PAAs. Here two remarkable methods, two-step anodization[125] and pre-imprinting anodization,[53] are introduced. In the two-step anodization, an ordered PAA was achieved by a pre-anodizing step. The aluminum substrate first underwent a long-time

pre-anodization. The formed PAA had a relatively ordered structure at the pore bottoms because of the long-time self arrangement. This PAA film was then removed by chemical dissolution. The remaining aluminum substrate had an order array of craters on the surface due to the pore bottoms of the previous PAA film. The second anodization was performed on the remaining substrate, with these ordered craters serving as the initial pore positions. Benefitting from this regular pore initiation, the second PAA film turned out to be highly ordered. Since its proposal, the two-step anodization has been widely used in the PAA fabrication because of its relative simple process. In the pre-imprinting anodization, the pore initiation was controlled by a lithographical pattern. A master mold containing a hexagonal array of convexes was fabricated with electron beam lithography. The pattern was transferred on to an aluminum plate by a physical imprinting process, producing a hexagonal matrix of concaves on the aluminum surface. The further anodization on this pre-imprinted substrate produced a PAA film with an ideally ordered porous pattern. Interestingly, the imprinting technique was also used to produce PAA films with novel pore shapes[126] or patterns.[116,127]

1.2.6 Material Properties

(1) Electrical Properties

Aluminum oxide exists in amorphous form as well as in multiple crystalline forms, including α-, γ-, δ-, θ-, and x-Al_2O_3. Anodic alumina is a special type of aluminum oxide. It was reported that anodic alumina had an amorphous structure when produced under a mild

voltage, but the crystalline component in the alumina increased as the anodizing voltage increased.[128] Aluminum oxide is a wide bandgap (6-11 eV.[4-6]) insulator with a high dielectric constant (~8 for BAA and ~55 for PAA[7-10]).

The electric characteristics of PAA films were studied by Gould et al.,[8,129,130] who used an Al-Al_2O_3-metal sandwich structure with the alumina pores partly filled with metal ions by metal pigmentation. dc measurements on this sandwich structure showed very complex conduction characteristics, including Schottky emission, tunneling, field ion diffusion, space-charge-limited conduction, ohmic conduction, electron emission, and differential negative resistivity. A typical barrier height for Schottky emission at Al-Al_2O_3 interface was calculated to be around 1.1 eV. The activation energy for the space-charge-limited conduction was estimated to be ~0.7 eV. For the barrier-type anodic alumina, the electric characteristics such as electron emission, electroluminescence, and electroforming effects together with a voltage-controlled differential negative resistance were also observed.[9,131]

The ac impedance characteristics of PAA films were studied by Hitzig et al.[10] The PAA structure was considered as a thick porous layer in series with a thin barrier layer. A simple Randles circuit was used as the equivalent circuit. According to their measurements, the porous layer had a high dielectric constant (~55) due to the oxide hydration whereas the barrier oxide had a dielectric constant of 8-12. The resistivity of the porous layer was 1.3×10^8 Ω·cm.

(2) Optical Properties

Optically PAA is characteristic for its blue photoluminescence (PL). Yamamoto et al.[132] reported that the PAA film fabricated in 0.5 M oxalic acid exhibited an emission peak at a wavelength of 470 nm. The PL centers were shown to be located predominantly in the middle region of the pore sidewalls. The PL emission was believed to originate from the electron transitions between the energy levels of the F^+ centers (oxygen vacancy trapping one electron) in the alumina film,[133] possibly from the F centers (oxygen vacancy with two electrons)[134] and the luminescent centers introduced from the oxalic impurities as well.[135] The PL emission was strong for the PAA film produced in oxalic acid, whereas no significant emission was observed on the PAA film fabricated in sulfuric acid[133] or phosphoric acid.[134] For the PAA film fabricated on a silicon substrate, multiple emission bands were observed, including the normal blue band, one violet band (395 nm), and two ultraviolet bands (~295 nm and ~340 nm). These emission bands at shorter wavelengths were possibly attributed to the excessive aluminum ions existing in the PAA film.[136]

(3) Mechanical Properties

In general, aluminum oxide has excellent mechanical robustness. The Young's modulus was reported to be 350-390 GPa for dense polycrystalline alumina[137] and 380-400 GPa for hot-pressed alumina ceramics.[138] For the barrier-type anodic alumina, the Young's modulus was ~98 GPa,[139] whereas for the porous-type anodic alumina, it showed to be anisotropic. In the direction of the pore length, the Young's modulus was measured to be 140 GPa,[11] whereas

in the transverse direction the Young's modulus was ~49 GPa for the PAA made from pure aluminum,[140] and 56-73.2 GPa for that made from AMG3M alloy.[141] In the work by Xia et al.,[11] the hardness and the fracture toughness of PAA films were measured to be 5.2 GPa and 3.4 MPa $m^{1/2}$ at room temperature, but increased and decreased to 6.3 GPa and 0.4 MPa $m^{1/2}$, respectively, after annealing the films at 650 °C for 12 hours. The relatively high Young's modulus was not affected by the same heat treatment. The PAA porosity has significant effects on it mechanical properties. Both the Young's modulus and the hardness decrease by a factor of ~2 as the porosity increases from about 0.1 to 0.3.[142,143] The atomic force microscopy (AFM) experiments by Choi et. al.[144] showed that the adhesion force between the PAA film and AFM tip decreased rapidly as the initial pores formed on the flat substrate. When the porosity was larger than 0.1, the adhesion force turned to be relatively constant because the actual contact area stayed almost unchanged due to the simultaneous increases in both the apparent contact area and the porosity.

(4) Thermal Properties

The reviews of the thermal characteristics of the barrier-type alumina has been given by Madhusudana and Fletcher,[145] and by Fletcher.[146] However, limited reports have been published on the thermal properties of the porous-type alumina. Ogden et al.[147] reported the thermal conductivity of an industrial alumina without giving detailed information on the film geometries. In the work of Borca-Tasciuc et al.,[148] the temperature dependence of the thermal properties of commercial anodic alumina membranes, such as the

thermal conductivity and thermal diffusivity, were characterized by using 3ω and photothermoelectric techniques. For the PAA film with a porosity of ~30% and a pore diameter of 0.02 μm, the effective thermal conductivity along the pore axis increased from 0.54 W mK^{-1} at 80 K to 1.33 W mK^{-1} at 300 K, while the thermal diffusivity measured with 3ω technique decreased from 2.2×10^{-6} m^2 s^{-1} to 1.0×10^{-6} m^2 s^{-1}, and from 1.6×10^{-6} m^2s^{-1} to 0.8×10^{-6} m^2s^{-1} by the photothermoelectric method, showing an anisotropic factor of 0.7.

1.2.7 Summary

In summary, porous anodic alumina has shown to be a nanomaterial of great research interest. Study on this material has been lasting for more than half a century. The porous structure is achieved naturally during the aluminum anodization process. Geometrically it is featured with the monodisperse nanopores, the straight channel profile, the high aspect ratio, and the high packing density. It is physically robust and chemically stable. For its unique porous structure, anodic alumina has been widely used in diverse fields such as electronics, optics, biology, etc. The pre-imprinting method shows to be effective in improving the pattern regularity.

In the future, ultra thin porous anodic alumina film integrated on silicon substrate will be interesting to the field of nanobiotechnology for the development of on-chip systems. The freestanding structure will be essential for utilizing anodic alumina truly as a molecular sieve. The large surface area of anodic alumina will be generally useful in sensor applications.

CHAPTER 2

FABRICATION AND CHARACTERIZATION OF THIN-FILM POROUS ANODIC ALUMINA

2.1 Substrates for Thin-Film Porous Anodic Alumina

Silicon (Si) is the most commonly used semiconductor material used in nanofabrication. As a supporting substrate for PAA thin films, silicon has advantages such as the excellent surface flatness and the good adhesion with aluminum. The silicon substrates used in this dissertation were commercial wafers purchased from Silicon Quest, Inc, with the following specifications: diameter: 4 inch; thickness: 500 μm±25 μm; orientation: [100]; doping: N type; resistivity: <0.005 Ω·cm; double-side polished. For the surface cleaning, the silicon wafers underwent a MOS clean by soaking in APM (NH_4OH:H_2O_2:H_2O =1:1:6 at 70 °C) for 10 min and in HPM (HCl:H_2O_2:H_2O =1:1:6 at 70 °C) for 10 min.

Silicon oxidizes electrochemically. After the aluminum film is converted to a PAA, the further anodization oxidizes the silicon substrate, forming a silicon dioxide (SiO_2) layer:

$$4OH^- + Si = SiO_2 + 2H_2O + 4e \quad (2.1)$$

Since SiO_2 is insoluble in typical PAA electrolytes, the silicon anodization quickly ceases after the SiO_2 layer is formed, due to its high electric resistance. However, from the author's experience, the anodization of aluminum directly on a silicon substrate was often accompanied with some local cracks on the surface, which was possibly due to the thermal or mechanical stress introduced from the silicon anodization. To obtain PAA films with better uniformity, the silicon substrate can be pre-coated with a thin oxide film as a

passivation layer to encapsulate the silicon substrate, preventing it from the anodization.

Silicon nitride (Si_3N_4) has an excellent adhesion to aluminum. Aluminum can be directly deposited on Si_3N_4 without using an intermediate adhesion layer such as Ti or Cr. Another advantage of Si_3N_4 is its high resistance to the KOH wet etch. It can be used as a mask for patterning the silicon substrate by the anisotropic KOH etch. A high quality Si_3N_4 on the silicon substrate can be achieved by depositing the low-stress Si_3N_4 through the low-pressure chemical vapor deposition (LPCVD). In this dissertation, for example, a 300-nm-thick Si_3N_4 film was deposited under the following conditions: DCS:NH_3=84:22 sccm, 200 mTorr, 800 °C. Si_3N_4 can be removed by CF_4 reactive ion etch. The 300-nm-thick Si_3N_4 was removed under the following conditions for 15 min: chamber pressure: 40 mTorr, RF power: 150 watts, CF_4 flow rate: 30 sccm.

Silicon dioxide (SiO_2) can also passivate the silicon substrate. High quality SiO_2 is thermally grown in furnace. Compared to Si_3N_4, SiO_2 is less resistant to the KOH etch (etch rate: 28 Å min^{-1})[149]. SiO_2 can also be removed by the CF_4 etch.

Glass is fully compatible with the anodization process because of its good chemical stability. The glass substrates used in this dissertation were commercial glass wafers purchased from Silicon Quest, Inc, with the following specifications: type: soda lime; diameter: 4 inch; thickness: 550 μm±50 μm; double-side polished. The glass surface is pre-cleaned using hot piranha or nanostrip to remove organic contaminants.

2.2 Preparation of Thin-Film Aluminum

Thick PAA films are made on thick aluminum substrates such as aluminum foils, whereas thin PAA films are made from aluminum deposited on solid substrates by metal evaporation or sputtering in nanofabrication.

The evaporation runs in two modes: thermal evaporation and electron-beam evaporation. Being heated either thermally or by high-energy electron beams, the aluminum resource is vaporized and deposited on the solid substrate. The deposition profile can be controlled to be either conformal (covering the substrate uniformly) or non-conformal (no coverage on vertical sidewalls). For the sputtering system, the deposition is achieved by the physical bombardment of ion beams on the metal resource. The deposition profile is conformal. The deposition substrates are required have a clean surface. MOS clean is preferred if the substrates are compatible with the process. Nanostrip and hot piranha are effective ways for removing organic contaminants. Visible particles and dusts can be removed by water rinsing, N_2 gas blow, and/or sonication.

The silicon substrate for the aluminum deposition was prepared as follows: 4-inch double-side polished silicon wafers with an orientation [100] were purchased from Silicon Quest, Inc. The wafers underwent a MOS clean process by soaking in APM (NH_4OH:H_2O_2:H_2O =1:1:6 at 70 °C) for 10 min and in HPM (HCl:H_2O_2:H_2O =1:1:6 at 70 °C) for 10 min. A 300-nm-thick low-stress Si_3N_4 film was deposited on the silicon substrate by LPCVD, under the following conditions: DCS:NH_3=84:22

sccm, 200 mTorr, 800 °C.

In this dissertation, high-purity (99.999%) aluminum (Research and PVD Material, Corp) was used as the material source. The typical deposition rate was 0.5-5 Å sec^{-1}. The deposition thickness was controlled in the range from tens of nm to the micrometer scale, depending on the experimental needs.

The aluminum deposited on the Si_3N_4-Si substrate visually looked as a mirror, indicating an excellent surface flatness. Figure 2.1 (A) is the AFM image of the top surface of a 1-μm-thick aluminum film deposited on a Si_3N_4-Si substrate by the electron-beam evaporation. Overall the surface was flat and clean. As the image shows, the surface was featured with a nanoscale grain structure. Figure 2.1 (B) is the cross-sectional profile scanned along a horizontal line in the image in (A). The peak-to-peak variation of the aluminum surface was less than 10 nm, with a standard deviation of 4.1 nm. This good surface smoothness was important for producing PAA films with a uniform porous structure. Other types of aluminum films such as foils and electroplated films generally did not have such good surface smoothness. In order to be used for the PAA production, these substrates need to go through laborious surface polishing processes. Compared with these films, aluminum thin films deposited on silicon-based substrates are of great advantage in the surface conditions. For this reason, in the experiments of this dissertation, the aluminum thin films deposited on the Si_3N_4-Si substrates were directly used in the anodization process without additional surface polishing processes.

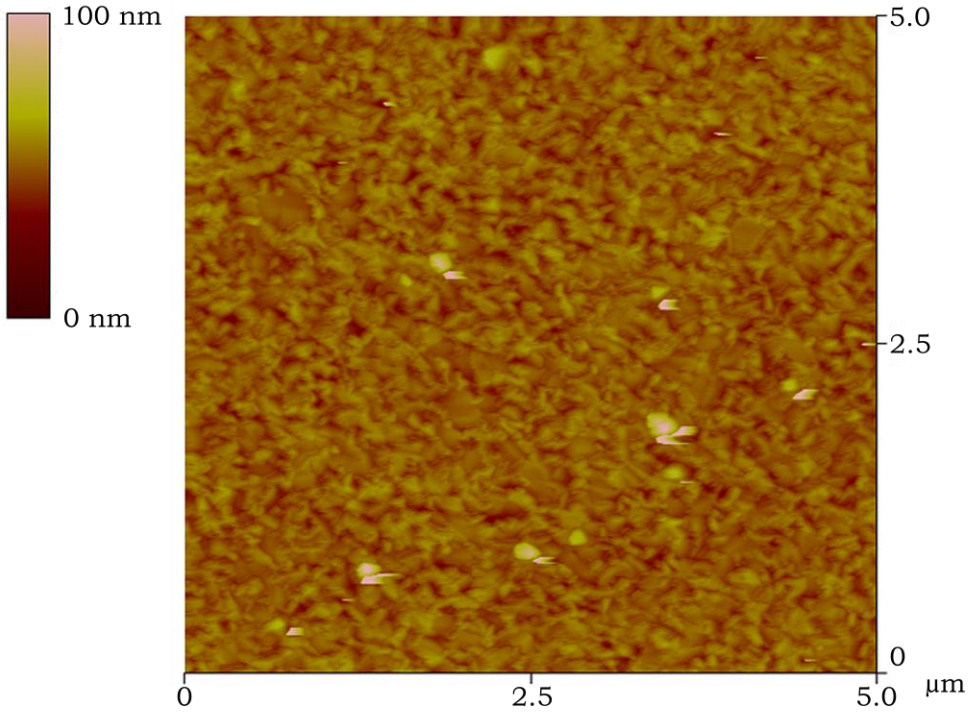

Figure 2.1. Aluminum Film on Si_3N_4-Si Substrate. (A) The AFM image of the top surface of a 1-µm-thick Al film on a Si_3N_4-Si substrate. (B) The cross-sectional profile, scanned along a single line in the surface in (A). The standard deviation of the Z depth was calculated to be 4.1 nm.

2.3 Anodization for Thin-Film PAA

The thin-film aluminum on a Si_3N_4-Si substrate was prepared as follows: 4-inch double-side polished silicon wafers with an orientation [100] were purchased from Silicon Quest, Inc. The wafers underwent a MOS clean process by soaking in APM (NH_4OH:H_2O_2:H_2O =1:1:6 at 70 °C) for 10 min and in HPM (HCl:H_2O_2:H_2O =1:1:6 at 70 °C) for 10 min. A 300-nm-thick low-stress Si_3N_4 film was deposited on the silicon substrate by LPCVD, under the following conditions: DCS:NH_3=84:22 sccm, 200 mTorr, 800 °C. High-purity (99.999%) aluminum was deposited on the Si_3N_4-Si substrate at 1.5 Å sec^{-1} for 1000 nm.

Prior to the anodization, the Si_3N_4-Si wafers coated with an aluminum film were rinsed with acetone, isopropanol, and water thoroughly, followed by drying under N_2 gas flow. The anodizing area was arbitrary as long as the anodizing voltage and current were under the compliances of the power source. In the experiments of this dissertation, the aluminum samples were anodized either in small pieces (a few cm^2 each) or as an entire wafer. The aluminum sample was installed on the anode, while a copper plate with a comparable size was installed on the cathode. The electrolytic bath was filled with a porous-type electrolyte. The aluminum sample and the copper plate were immersed vertically in the electrolyte, being parallel to each other with a separation distance of ~10 cm. The anode and the cathode were connected to the (+) and (-) terminals of the dc power source (Keithley 2400 or BK Precision 1787A), respectively. The power source was controlled by computer through a GPIB or RS232 interface. The

electric characteristics were monitored in real time using a Matlab program written by the author. The anodization settings, such as the voltage and the electrolyte, have determinative effects on the porous structure of the final PAA film. The anodization conditions have been discussed in details in Chapter.2. A typical condition set used in this dissertation was as follows: dc voltage: 40 V; electrolyte: 0.3 M oxalic acid; temperature: 20 °C; no physical stirrings. The anodization process was controlled by turning on/off the power source through the computer program. After the anodization, the alumina sample was rinsed with dH_2O thoroughly and dried under N_2 gas flow.

Figure 2.2 shows a current-time profile recorded in real time during the anodization of a 1-μm-thick aluminum film under the conditions described above. The entire time period was ~400 sec, during which the current profile underwent a few changes along the time, explicitly reflecting the anodization stages as described in Subsection.1.2.3. From t=0 to 12 sec, it was the period of the barrier-type oxide growth. A thin and non-porous alumina film was formed at the surface of the aluminum substrate. The current decreased rapidly because the resistance of the barrier oxide increased quickly as it grew thicker. After t=12 sec, the current was gradually increased, leveled off around t=75 sec. In this stage, the electrolytic ions migrated through small paths in the barrier oxide, continuing oxidizing the aluminum underneath the barrier layer. The existence of small paths was possibly due to the grain structures and material impurities of the aluminum substrate. These small paths were widened by the field-assisted dissolution during the further anodization, forming the initial

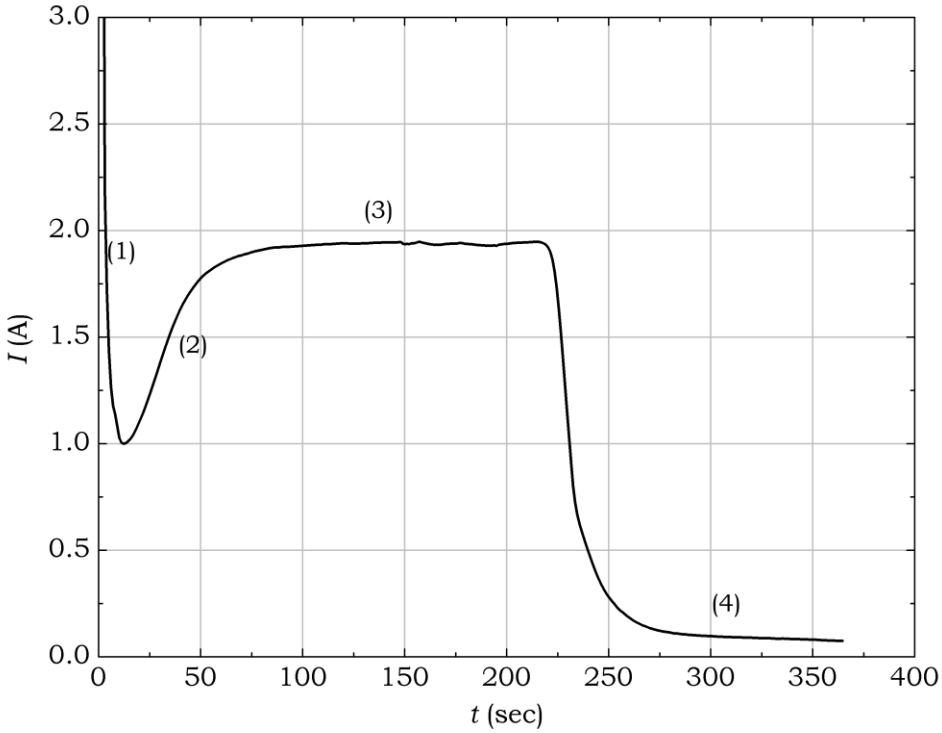

Figure 2.2. I-t Curve of Thin-Film Aluminum Anodization. The curve was recorded in real time during the anodization of a 1-μm-thick aluminum film, showing four different stages along the anodization process: (1) the barrier oxide growth, (2) the pore initiation, (3) the steady-state growth, and (4) the completion.

alumina pores. At the same time, the electric field was redistributed inhomogeneously, being much more concentrated in the initial pores than the planar areas. The further anodization, as well as the field-assisted alumina dissolution, preferably continued at the bottoms of the initial pores. From t=75 to 225 sec, the current remained stable at ~2×10^{-2} A. In this period, the field-assisted oxidation and dissolution reached a dynamic equilibrium at the pore bottoms, establishing a steady-state anodization. The pores grew deeper into the substrate at a constant speed. Since t=225 sec, the aluminum film started to be depleted. When each pore bottom reached the Si_3N_4-Si substrate, the local anodization ceased. As a result the current decreased rapidly. By t=275 sec, the anodization was completely ceased. The current was reduced to the leakage current level. The total time length of the effective anodization was ~250 sec. The anodization rate in this particular example was ~4 nm sec^{-1}. Under the constant-voltage mode, the absolute current is proportional to the anodizing area. In this experiment, the anodized area was a few cm^2. Therefore the steady-state current density was estimated to be on the order of 10^{-2} A cm^{-2}. Compared to thick alumina membranes, the time course of anodizing aluminum thin films was much shorter. In the thick-film anodization, the steady-state process could last for hours or even days.[56,57] However, in this thin-film anodization, the steady-state anodization only lasted for less than 200 sec. The time period for the barrier oxide growth and the pore initiation was ~75 sec, counting almost one thirds of the total anodizing time.

2.4 Thin-Film PAA as Anodized

Figure 2.3 shows the AFM and scanning electron microscopy (SEM) images of the alumina surface as anodized. The aluminum sample and the anodization conditions were the same as described in the previous section. Briefly, the 1-μm-thick aluminum film was anodized in 0.3 M oxalic acid under a dc bias of 40 V at room temperature.

As the images show, the as-anodized alumina surface was featured with a structure of microscale grains. These micrograins were possibly resulted from the nonuniform volume expansion during the Al-to-Al_2O_3 conversion. The alumina pores were seen as the dark spots in the SEM image, randomly distributed over the surface with irregular shapes. The pore diameter was ~20 nm. Shallow grooves were formed along the boundaries between the micrograins. It was noticed that most alumina pores were formed on the grooves, indicating that the pore initiation preferably occurred on the boundaries of between the micrograins, where the electrolytic ions probably had an easier access to the aluminum substrate underneath.

Seen from the images, the porous pattern as anodized was rather random, instead of being the ideal hexagonal array consisting of circular pores. It was primarily because the steady-state anodization of such a thin film was too short. Therefore the porous structure was significantly off the ideal hexagonal pattern Due to this short-time process, the alumina film was subject to the electrolytic dissolution only for a brief period. The surface was believed to well retain the topographic characteristics of the initial pores.

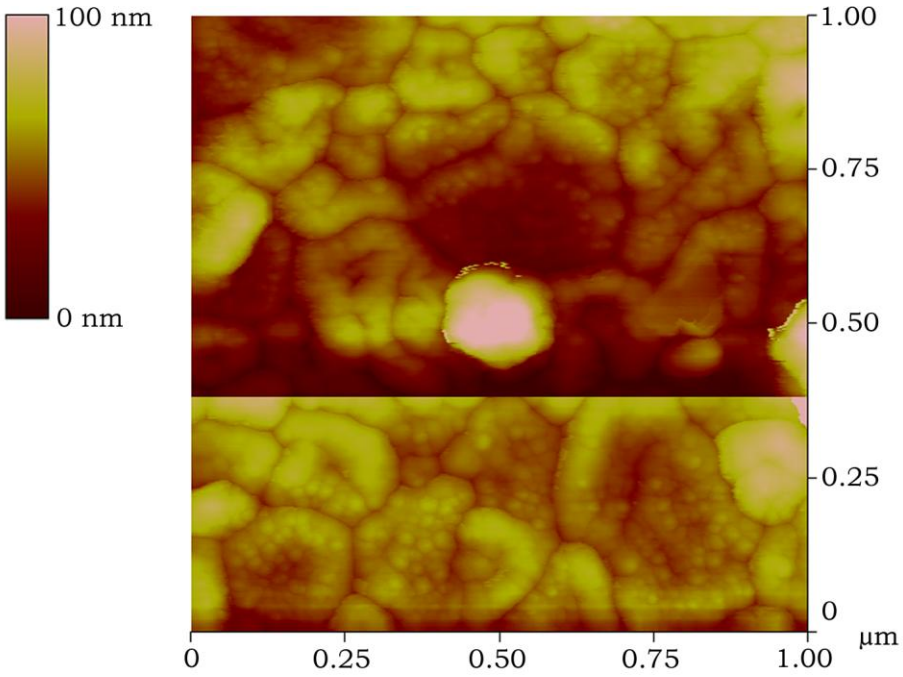

(A)

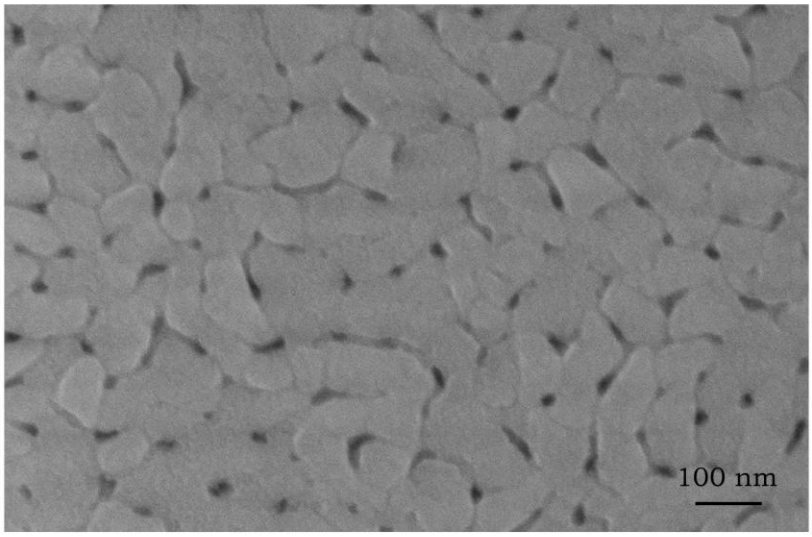

(B)

Figure 2.3. PAA Surface as Anodized. (A) The AFM image of a PAA film as anodized. (B) The SEM image of the PAA film. The PAA film was fabricated from a 1-µm-thick aluminum substrate, under the following conditions: 40 V (dc), 0.3 M oxalic acid, room temperature.

2.5 Pore Widening by H_3PO_4 Etch

Porous-type electrolytes dissolve PAAs slowly, by the following chemical reaction mechanism:

$$Al_2O_3 + 6H^+ = Al^{3+} + 3H_2O \quad (2.2)$$

The chemical dissolution is isotropic, taking place at the alumina top surface, as well as on the sidewalls of the alumina pores. In the aluminum anodization, there are two types of electrolytic dissolution. One takes place at the pore bottoms where the dissolution is accelerated by the high electric field across the barrier oxide. This type of dissolution is very fast, being responsible for the pore growth. The other type is the pure electrolytic dissolution without the field acceleration, taking place on the alumina top surface and the sidewalls. This type of dissolution is relatively slow but it enlarges the alumina pores. This effect has been utilized as an additional control on the pore size and the film porosity. In research reports, phosphoric acid is widely used for the pore widening process.

This section investigates the effects of the acidic etch on the geometry of PAA thin films. The thin-film aluminum on a Si_3N_4-Si substrate was prepared as follows: 4-inch double-side polished silicon wafers with an orientation [100] were purchased from Silicon Quest, Inc. The wafers underwent a MOS clean process by soaking in APM (NH_4OH:H_2O_2:H_2O =1:1:6 at 70 °C) for 10 min and in HPM (HCl:H_2O_2:H_2O =1:1:6 at 70 °C) for 10 min. A 300-nm-thick low-stress Si_3N_4 film was deposited on the silicon substrate by LPCVD, under the

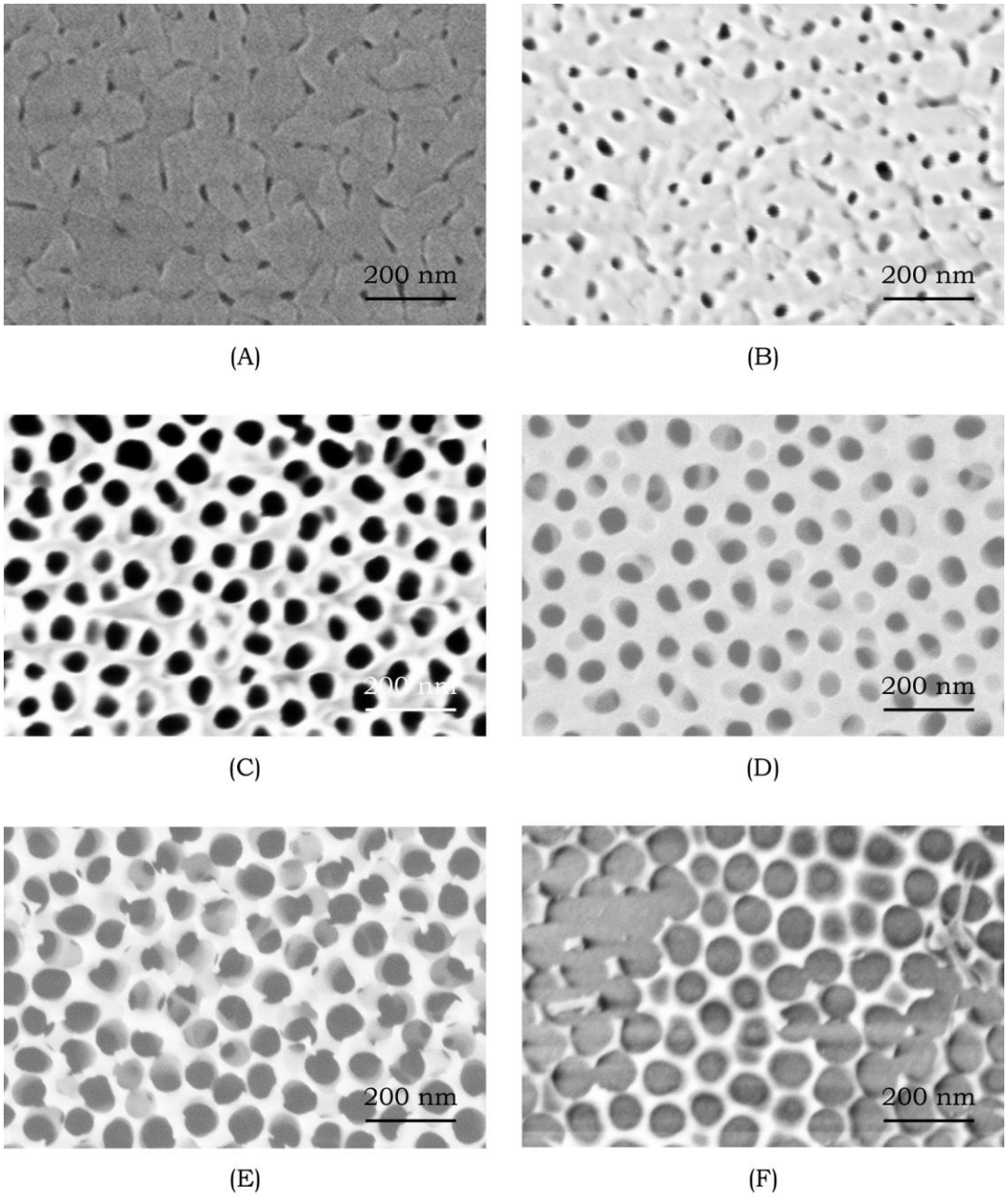

Figure 2.4. Pore Widening by H_3PO_4 Etch. (A)-(F): The SEM images of the PAA films etched by 5% H_3PO_4 at room temperature for 0, 10, 40, 45, 60, and 80 min, respectively.

following conditions: DCS:NH_3=84:22 sccm, 200 mTorr, 800 °C. High-purity (99.999%) aluminum was deposited on the Si_3N_4-Si substrate at 1.5 Å sec^{-1} for 1000 nm.

For the pore widening, the samples were soaked in 5% H_3PO_4 over a series of time periods. The incubations were done at room temperature without physical stirrings.

Figure 2.4 shows the porous structures of the samples after an incubation time of 0-80 min. Over all, the alumina pores experienced two changes as the etch time increased. First, the pore diameter became larger. Second, the pore shape became more round. The groove texture on the original sample attenuated after 10 min and disappeared after 40 min. The pore widening was ultimately limited by the alumina sidewalls. After 60 min the membrane surface was slightly over etched while after 80 min some pores in local areas were destructed.

Since the porous structure of PAA thin films were significantly different from the ideal hexagonal array. To take count in the pore irregularity, in this dissertation, the pore shapes were modeled as ellipses with two characteristic dimension parameters a and b ($a > b$). The diameter d of a single pore was defined as:

$$d = \sqrt{a \cdot b} \tag{2.3}$$

The diameters of individual pores were measured from in the SEM images. Figure 2.5 plots the average value of d as a function of the etch time, showing that d was linearly proportional to the H_3PO_4 etch time, with the following trend line:

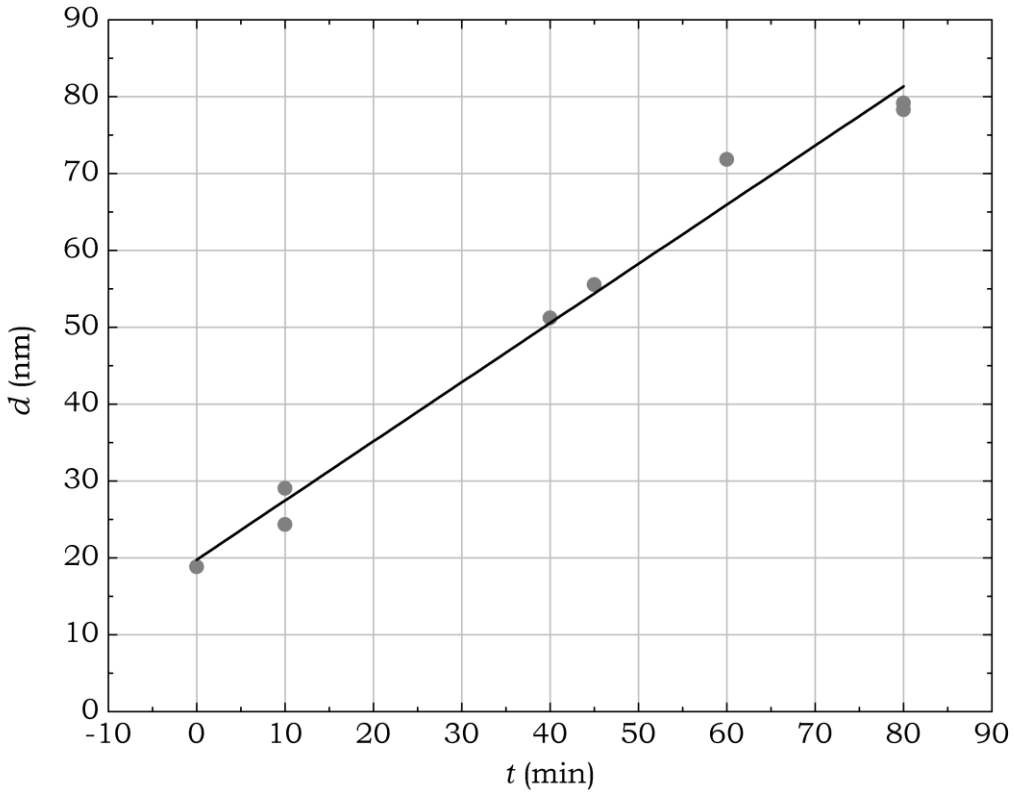

Figure 2.5. Pore Size versus H_3PO_4 Etch Time. The average PAA pore diameter (d) increased as a linear function of the etch time (t) in 5% H_3PO_4 at room temperature. The etch rate was calculated to be 0.77 nm min^{-1}.

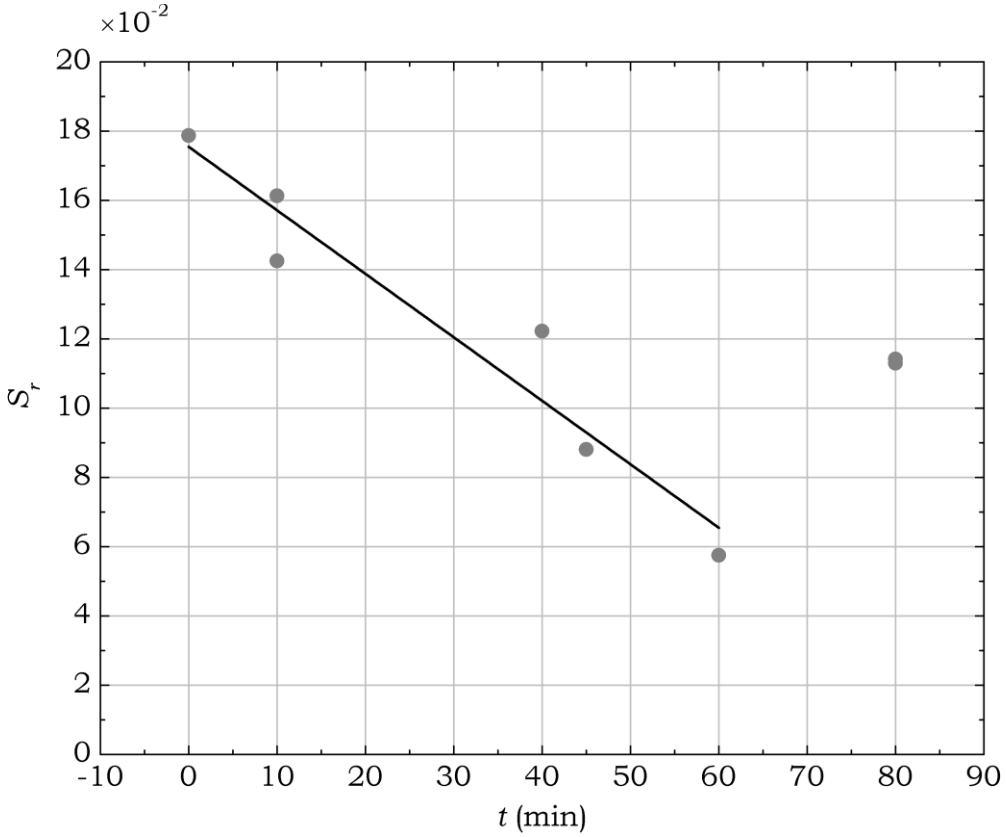

Figure 2.6. Pore Uniformity versus H_3PO_4 Etch Time. The pore uniformity, expressed by the relative standard deviation of the pore diameter (S_r), decreased linearly as a function of the etch time (t) in 5% H_3PO_4, within the first 60 min.

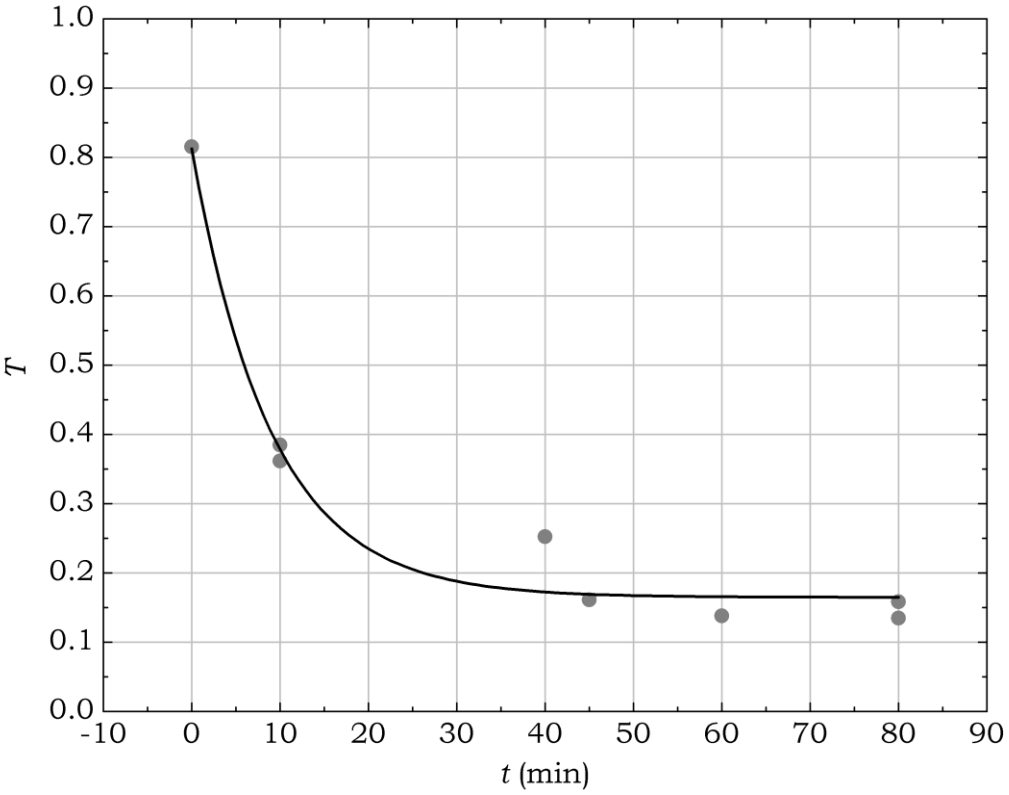

Figure 2.7. Pore Distortion versus H_3PO_4 Etch Time. The pore distortion (T) decreased exponentially as a function of the etch time (t) in 5% H_3PO_4.

$$d = 0.77t + 19.77 \tag{2.4}$$

Where d and t were in the units of nm and min, respectively. Therefore, the etch rate of by 5% H_3PO_4 at room temperature was 0.77 nm min^{-1}.

The "pore uniformity" was expressed using the relative standard deviation of the pore diameter (S_r). As Figure 2.6 shows, S_r decreased linearly as a function of the etch time from 18% at t=0 min to 6% at t=60 min. The mathematical expression was:

$$S_r = -1.83 \times 10^{-3} t + 17.5 \times 10^{-2} \tag{2.5}$$

Where t was in the unit of min. It suggests that the pore uniformity was improved along the pore widening process. At t=80 min, however, S_r was noticeably deviated from the trend line, being ~11%. At this point, the main body of the membrane was etched away, leaving a residual layer on the substrate. The geometric features seen in Figure 2.4 (F) were actually the structures near the pore bottoms, where the scallop shape of the pore bottom had certain degree of pore-to-pore variations. From the top view, these variations were reflected as a relatively large variation of the pore diameter. That was possibly the reason why S_r was off the trend line at t=80 min.

The "pore regularity" was evaluated using the pore distortion, T, which is simply defined as:

$$T = \frac{|a-b|}{d} \tag{2.6}$$

Ideally alumina pores would be in a perfect circular shape ($a = b$), having a distortion of $T = 0$. Figure 2.7 plots the mean distortion T as

a function of the etch time. The curve fitting yielded the following relation:

$$T = 0.16 + 0.65e^{-0.11t} \tag{2.7}$$

Based on the plot, the pore regularity was significantly improved in the first 30-min etch, with T reduced from 0.8 to 0.2. After 30 min, T gradually leveled off at 0.16.

In summary, the H_3PO_4 etch after the anodization served as an additional control on the porous geometry of PAA thin films. It enlarged the alumina pore size by dissolving the pore sidewalls. The enlargement was ultimately limited by the sidewall thickness. The etch time needed to be controlled to avoid any destructive over etches. Importantly, the widening process also improved the pattern regularity by enhancing the pore uniformity and reducing the pore distortion.

In research reports, the pore widening process has been commonly used for removing the barrier oxide and increasing the pore size. In research papers, the widening protocol varied in terms of the acid type, concentration, etch time, and temperature. Therefore PAA membranes produced under the same anodization conditions could show different pore dimensions because of the widening process. For this reason, it was not suitable to use the pore diameter to correlate the pore dimension with the anodization conditions. Instead, the inter-pore distance was not subject to the pore widening process, being able to serve as a characteristic parameter for describing the dependence of the pore dimension on the anodization conditions.

2.6 Cross Section of Thin-Film PAA

PAA is characteristic for its unique porous structure. Unlike other porous membranes whose pore paths often have complex structures, Alumina pores are straight. Figure 2.8 shows the cross section of a 1.2-μm-thick PAA fabricated on a Si_3N_4-Si substrate. Briefly, the fabrication was: 1.2-μm-thick high-purity (99.999%) aluminum was deposited on a 300-nm-thick Si_3N_4 substrate, and anodized in 0.3 M oxalic acid with a dc voltage of 40 V. The PAA film underwent the pore widening process in 5% H_3PO_4 for 30 min at room temperature. The PAA sample was cleaved manually. The cross section was inspected under SEM. As the image shows, all the alumina pores were straight, penetrating through the membrane. The pores were parallel to each other with their channel axes perpendicular to the substrate.

It has been well known that PAA as anodized has a thin barrier oxide layer at the bottom of the alumina pores.[61] The barrier oxide layer is a natural component of PAA that forms during the anodization process. It is the active frontier where the field-assisted oxidation and dissolution take place simultaneously. PAA films are often utilized as a molecular sieve for applications such as filtrations and separations, in which PAA films are required to have through pores for the purpose of molecular transport. For these applications, the barrier oxide is an undesired feature and needs to be removed to achieve through pores.

The pore widening process discussed in the previous section serves as a simple and effective method for removing the barrier oxide layer. The 1.2-μm-thick PAA film was etched in 5% H_3PO_4 for 30 min at room

temperature. After the etch, no barrier oxide was observed at the pore bottoms (Figure 2.8 (B)). Since the wet etch was isotropic, the pore diameter also increased in the etch process. The etching time needed to be controlled to avoid over etches.

Besides the wet etch, CF_4-based reactive ion etch was an efficient approach for removing the alumina barrier oxide. The CF_4 dry etch was anisotropic, meaning that the alumina pores were not widened during the etch process. However, if the pore aspect ratio was high, the etching efficiency might be low as the etchant needed to go through the long channels to reach the barrier layer. In this case, the alternative method was to perform the CF_4 etch from the backside of PAA films, directly upon the barrier oxide. This required the PAA films to have a freestanding structure such that the barrier oxide could be exposed directly to the etchant. Methods of fabricating such freestanding structures, such as the KOH etch and the double-layer anodization, are discussed in details in Chapter 3. The exposed barrier oxide could be effectively removed by CF_4 anisotropic etch. The typical settings of the CF_4 etch process was: chamber pressure: 40 mTorr, RF power: 150 watts, CF_4 flow rate: 30 sccm, time: 15 min. The CF_4 etch here was referenced from a process for etching silicon or silicon dioxide. Its cleaning effects on the PAA barrier oxide were presumably due to the high-energy bombardment by the reactive ions generated in the RF plasma.

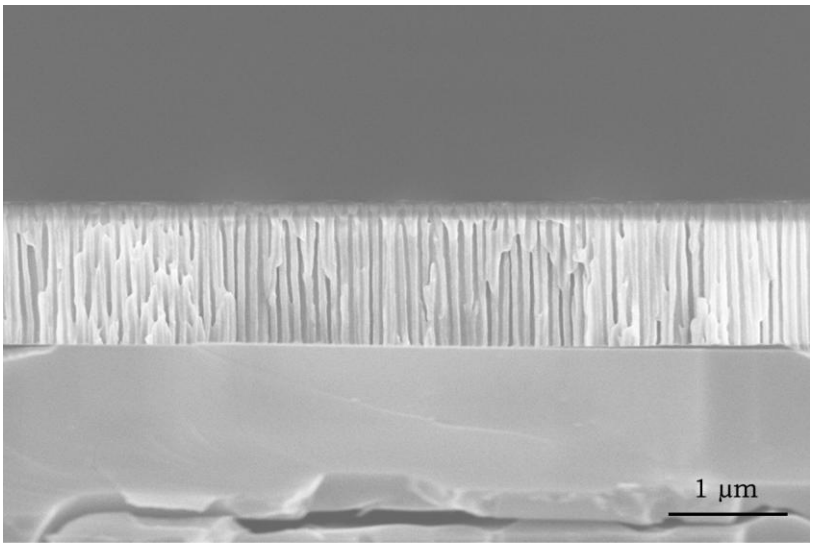

(A)

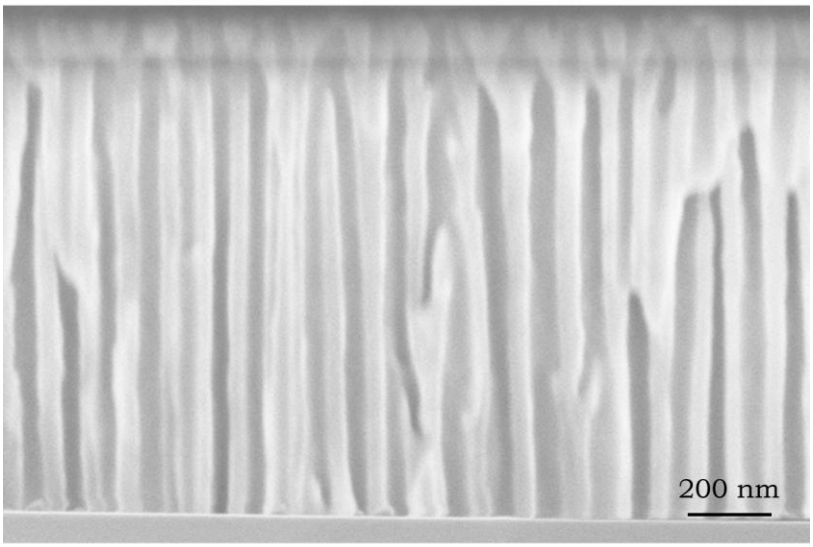

(B)

Figure 2.8. Cross Section of Thin-Film PAA. (A) The cross section of a 1.2-µm-thick PAA film fabricated on a Si_3N_4 substrate, showing straight pore channels. (B) The high-magnification view of the image in (A).

2.7 Anodization Conditions

In this section, the major porous-type electrolytes, including oxalic acid, sulfuric acid, and phosphoric acid were used for fabricating silicon-based PAA thin films, at different anodizing voltage settings.

Briefly, the aluminum samples were prepared as follows: A 300-nm-thick low-stress Si_3N_4 film was deposited on the silicon substrate by LPCVD, under the following conditions: DCS:NH_3=84:22 sccm, 200 mTorr, 800 °C. High-purity (99.999%) aluminum was deposited on the Si_3N_4-Si substrate at 1 Å sec^{-1} for 200 nm.

The three electrolytes were prepared as follows: (1) Oxalic acid ($(COOH)_2$, Mallinckrodt Baker, Inc) was prepared in dH_2O with a final concentration of 0.3 M. (2) Sulfuric acid (H_2SO_4, Mallinckrodt Baker, Inc) was prepared in dH_2O with a final concentration of 0.3 M. (3) Phosphoric acid (H_3PO_4, Mallinckrodt Baker, Inc) was prepared in dH_2O with a final concentration of 10% (w/v).

With each electrolyte above, six anodizations were performed, under an anodizing voltage of 10, 20, 30, 40, 50, and 60 V, respectively. All the anodizations were all performed at room temperature, without physical stirrings. The anodized samples underwent a pore widening process by soaking in 5% H_3PO_4 for 10 min. The samples were then with dH_2O thoroughly and dried under N_2 gas flow.

SEM images were taken on the top surfaces of the samples obtained from the conditions described above. Figure 2.9-2.11 show the porous patterns of the samples produced in sulfuric acid, oxalic acid, and phosphoric acid, respectively.

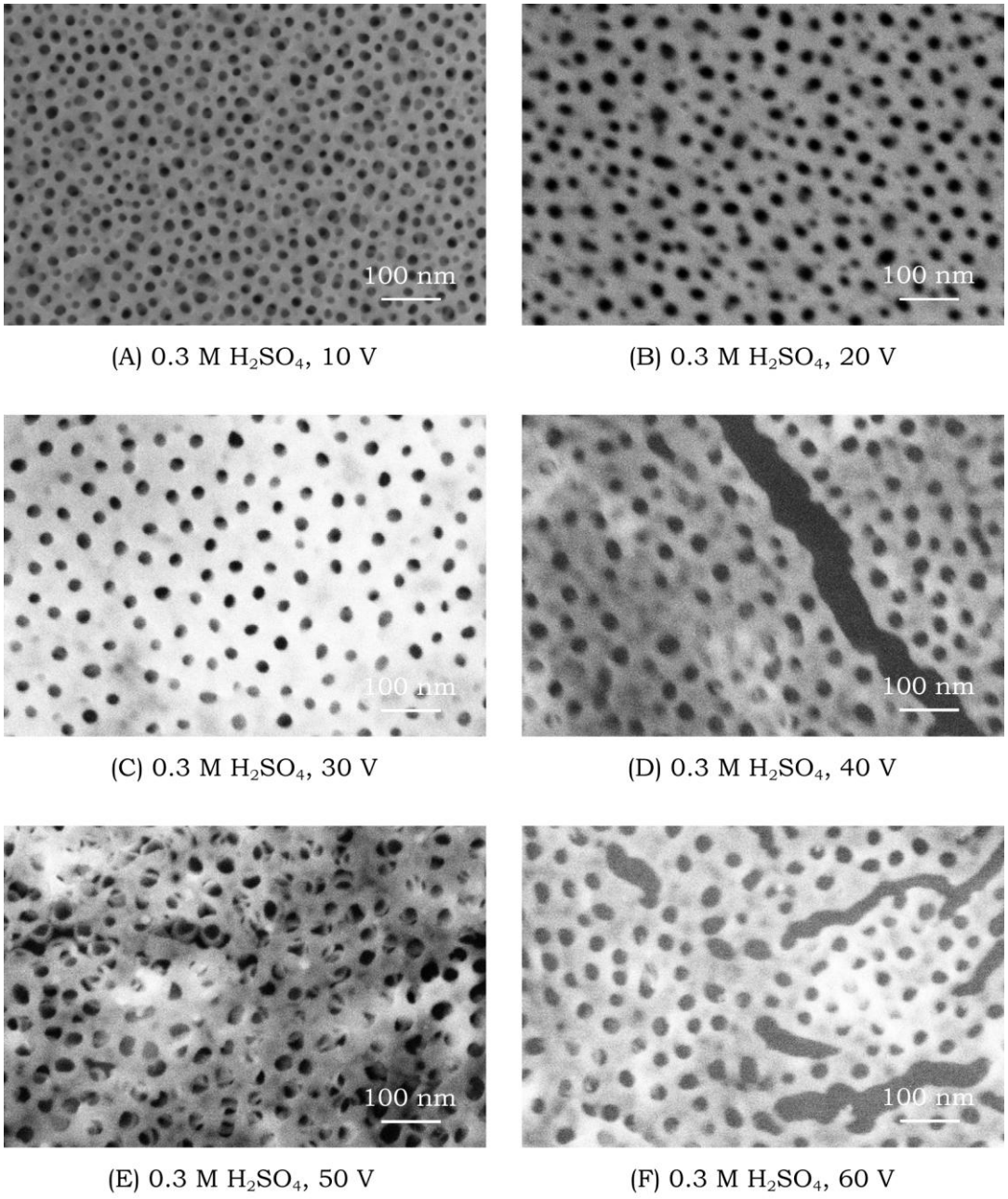

(A) 0.3 M H_2SO_4, 10 V

(B) 0.3 M H_2SO_4, 20 V

(C) 0.3 M H_2SO_4, 30 V

(D) 0.3 M H_2SO_4, 40 V

(E) 0.3 M H_2SO_4, 50 V

(F) 0.3 M H_2SO_4, 60 V

Figure 2.9. PAA Films Produced in Sulfuric Acid. (A)-(F): The SEM images of the top surfaces of the PAA films fabricated in 0.3 M sulfuric acid at room temperature, with an anodizing voltage from 10 to 60 V. The pores were widened in 5% H_3PO_4 for 10 min.

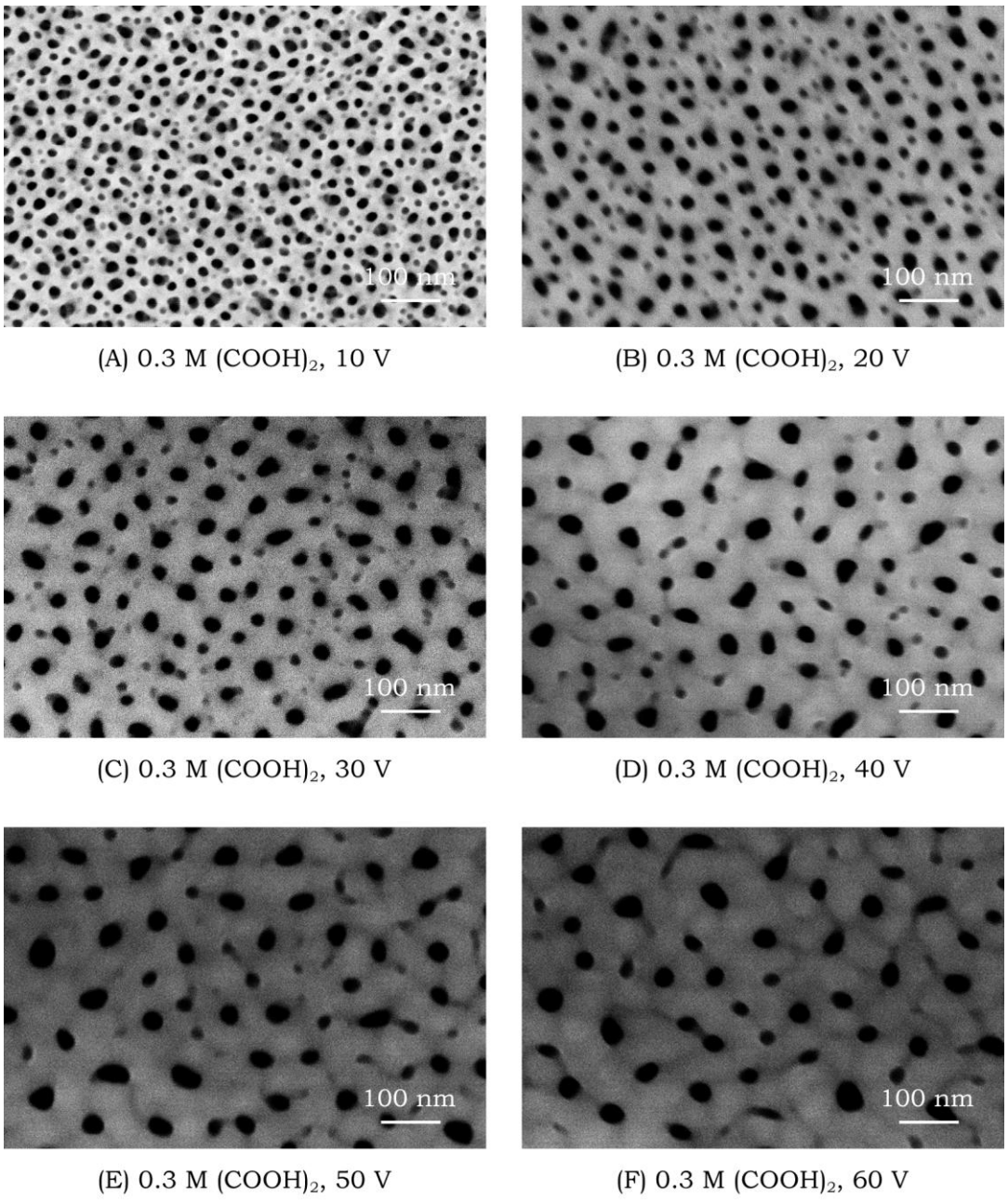

(A) 0.3 M $(COOH)_2$, 10 V

(B) 0.3 M $(COOH)_2$, 20 V

(C) 0.3 M $(COOH)_2$, 30 V

(D) 0.3 M $(COOH)_2$, 40 V

(E) 0.3 M $(COOH)_2$, 50 V

(F) 0.3 M $(COOH)_2$, 60 V

Figure 2.10. PAA Films Produced in Oxalic Acid. (A)-(F): The SEM images of the top surfaces of the PAA films fabricated in 0.3 M oxalic acid at room temperature, with an anodizing voltage from 10 to 60 V. The pores were widened in 5% H_3PO_4 for 10 min.

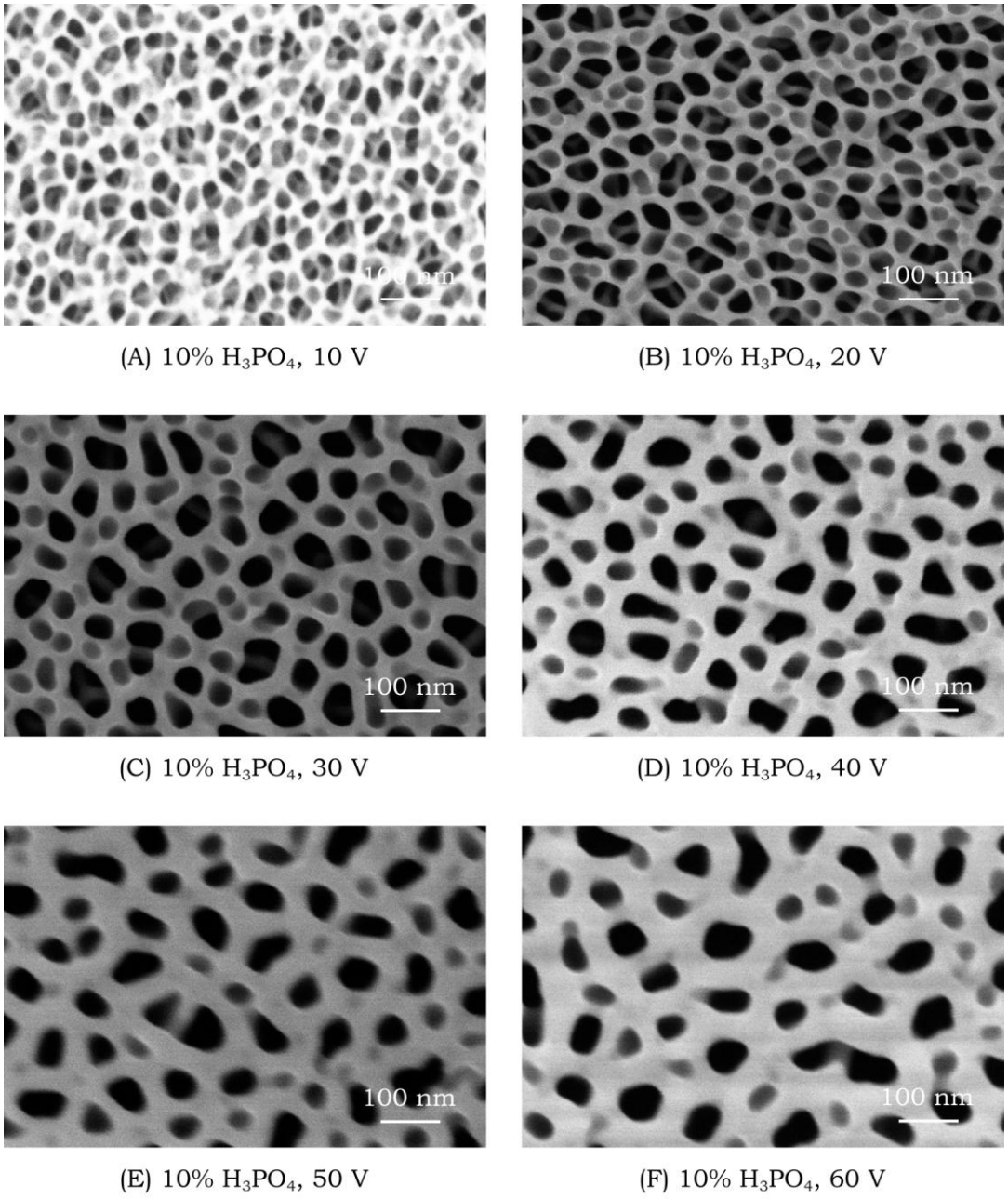

(A) 10% H_3PO_4, 10 V

(B) 10% H_3PO_4, 20 V

(C) 10% H_3PO_4, 30 V

(D) 10% H_3PO_4, 40 V

(E) 10% H_3PO_4, 50 V

(F) 10% H_3PO_4, 60 V

Figure 2.11. PAA Films Produced in Phosphoric Acid. (A)-(F): The SEM images of the top surfaces of the PAA films fabricated in 10% phosphoric acid at room temperature, with an anodizing voltage from 10 to 60 V. The pores were widened in 5% H_3PO_4 for 10 min.

Oxalic, sulfuric, and phosphoric acids are the three major electrolytes for producing PAA membranes. In the fabrication of thick PAA membranes, these three acids are used with different voltage ranges for producing different pore dimensions. Sulfuric acid with a relatively low anodizing voltage (15-30 V), is suitable for producing small alumina pores. Oxalic acid operates at moderately higher voltages (40-80 V). Phosphoric acid is usually used in the high-voltage anodization (80-200 V) for making PAA membranes with large pores.

The aluminum films used here were only 200 nm thick, several orders of magnitude thinner than thick aluminum substrates. The porous patterns of the corresponding PAAs were relatively less ordered, as seen in Figure 2.9-2.11. Anodization conditions could be part of the reasons, as the pore pattern was dependent on the anodization conditions.[3] For the experiments in this section, the more important reason was the ultra small thickness of the aluminum substrates. The anodizations on the 200-nm-thick aluminum films took only minutes or seconds to complete, whereas the anodizations on the thick aluminum substrates could last hours or days.[56,57] Because PAA self arranges its porous structure during the steady-state anodization, longer steady-state anodization allows more optimal rearrangements, therefore producing a more ordered porous pattern. On the other hand, under the same anodization conditions, the pore initiation always takes the same time, regardless of the aluminum thickness. For thick aluminum films, the time for the pore initiation is negligible compared to the period of the steady-state anodization stage. For thin aluminum films, however, the time period of the pore

initiation stage counts a significant portion of the entire anodizing time, because the steady-state anodization is rather short. Therefore the surface of PAA thin films represents more of the structural characteristics of the initial pores, compared to thick PAA films. For this reason, the porous structure of PAA thin films is generally less ordered. Achieving PAA thin films with highly ordered porous structures still remains as a challenge.

The inter-pore distance of these PAA thin films increased as a function of the anodizing voltage. As Figure 2.12 shows, for oxalic acid and phosphoric acid, the average inter-pore distance and the anodizing voltage maintained a good linearity in the voltage range of 10-60 V. Based on the curve fittings, the dependence of the inter-pore distance upon the voltage was 1.51 nm V^{-1} and 1.55 nm V^{-1} for oxalic acid and phosphoric acid, respectively. For sulfuric acid, the linearity was reasonable below 30 V but not above 30 V. It was possibly because of the strong acidity of sulfuric acid. Its field-assisted oxidation and dissolution increased more rapidly than the other two electrolytes as the voltage increased. At high voltages (>30 V), the anodization was rather fast, as seen in Figure 2.13. On a 200-nm-thick aluminum substrate, the anodization completed almost instantaneously. The dynamics of the field-assisted oxidation and dissolution was probably far off the equilibrium state. It could possibly explain the unusual porous patterns obtained at 40-60 V. In addition, surface defects such as gaps were observed on these patterns. Therefore the anodizations in sulfuric acid only under 30 V were favorable in producing PAA thin films with relatively small pores.

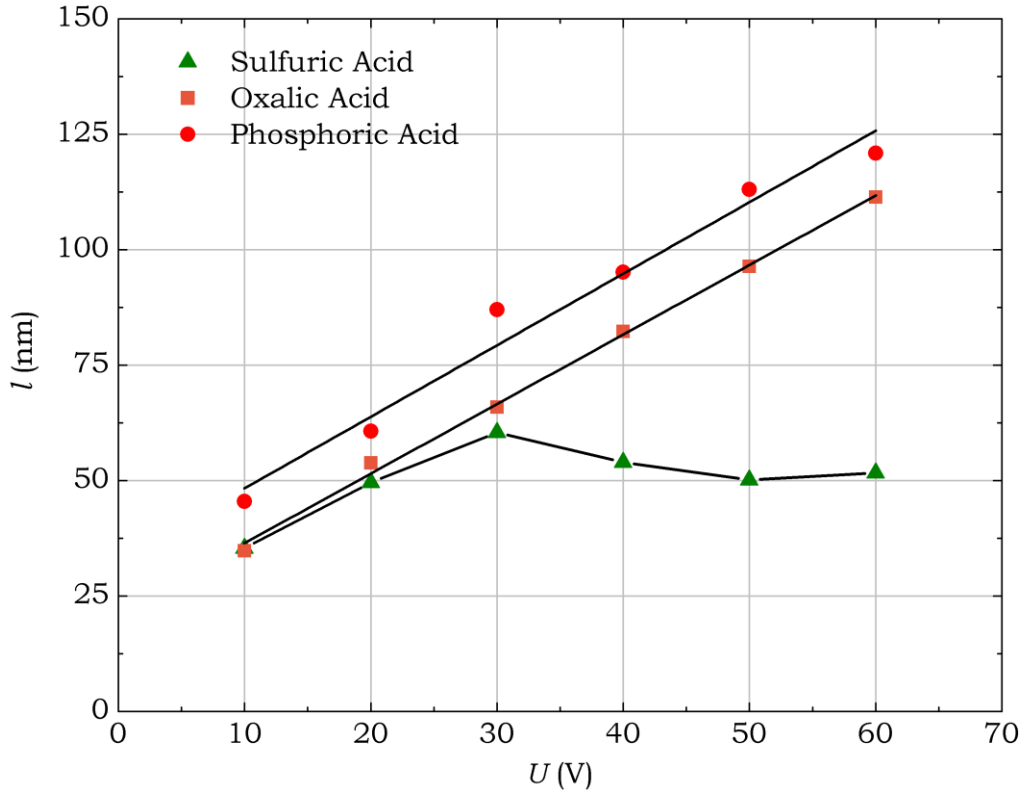

Figure 2.12. Inter-Pore Distance versus Anodizing Voltage. The plot shows the inter-pore distance (l) as a function of the anodizing voltage (U) for oxalic, sulfuric and phosphoric acids.

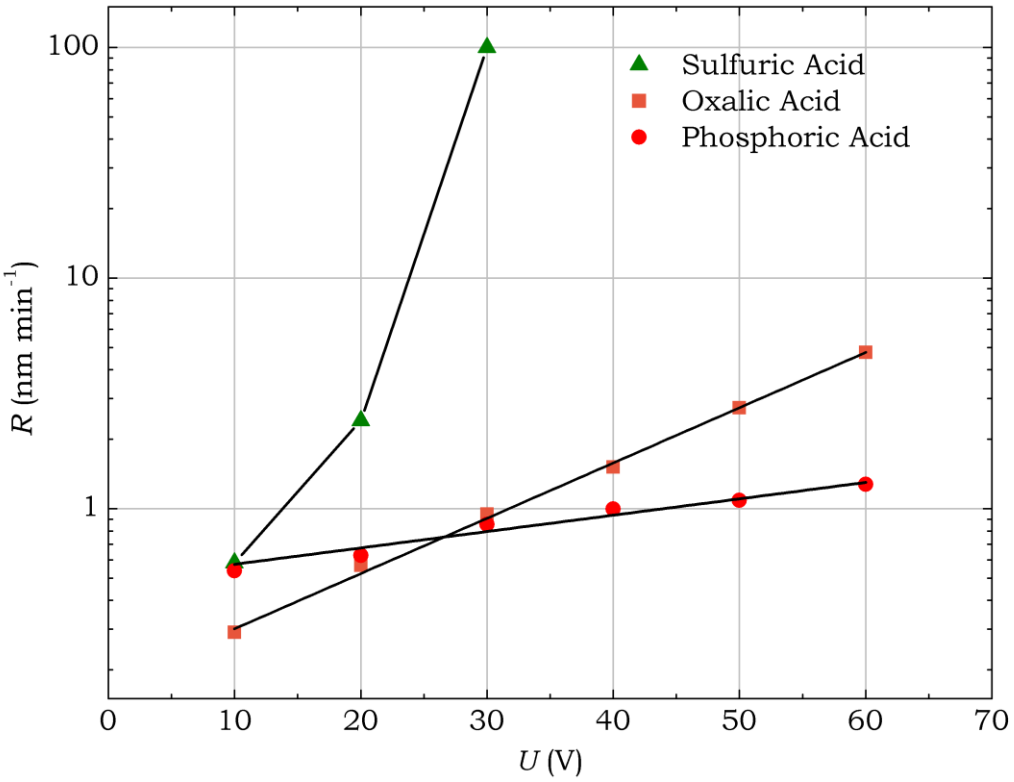

Figure 2.13. Anodization Rate versus Anodizing Voltage. The plot shows the anodization rate (R) as a function of the anodizing voltage (U) for oxalic, sulfuric and phosphoric acids.

Figure 2.13 shows the anodization rate (R) as a function of the anodizing voltage (U). The anodization rate was calculated as the aluminum thickness (200 nm) divided by the total anodizing time (recorded in the experiments). Sulfuric acid was the most sensitive to the applied voltage whereas phosphoric acid was the least. As the plot shows, for oxalic acid the phosphoric acid, R was exponential to U:

$$\log R = a \cdot U + b \tag{2.8}$$

Based on the curve fittings, the exponential factor a was 5.5×10^{-2} and 1.6×10^{-2} for oxalic acid and phosphoric acid, respectively. For sulfuric acid, the slope was much steeper. For example, the anodization rate reached 100 nm s^{-1} when the voltage was 30 V. It took only 2 seconds to complete the anodization on a 200-nm-thick aluminum film.

It is worthwhile to point out that the method used here for calculating the average anodization rate was dependent of the aluminum film thickness, especially when the film was very thin. As seen from Figure 2.2, the anodization rate was slower in the pore initiation stage than in the steady-state stage. For the 200-nm-thick aluminum substrates, the time period of the pore initiation stage counted a significant portion of the total anodizing time. Therefore the average anodization rates shown in Figure 2.13 were expected to be lower than their corresponding steady-state anodization rates.

At low anodizing voltages, the PAA thin films contained a number of "unfinished" pores, shown as the gray holes in the SEM images. These pores creased growing during the anodization. The possible reason for

these “unfinished” pores was that at low anodizing voltages the surfaces were over initialized with excessive pore seeds. As the anodization went along, some of these pores either merged with other pores, or ceased growing because of the local aluminum depletion. As seen in Figure 2.9-2.11, the number of “unfinished” pores reduced as the anodizing voltage increased.

In summary, for sulfuric acid, the best organized porous structure was produced under a voltage of 30 V, agreeing well with the previous results.[3,55] Higher anodizing voltages were inappropriate as the PAA films showed to have artifacts under high voltages. For oxalic acid, the porous patterns fabricated within 10-30 V were featured with similar many “unfinished” pores due to the over initialization of pores. These “unfinished” pores were less when the anodizing voltage was between 40 V and 60 V. For phosphoric acid, the PAA films fabricated under a voltage of 10-20 V showed complex porous structures. When the voltage was increased to 30 V or above, the pore channels were more apparent to see. The PAA pores fabricated in sulfuric acid had the best pore regularity (especially at 30 V) while the pores made in phosphoric acid had the largest variations in the shape.

In general, the porous pattern of the PAA thin films was less ordered than that of the thick PAA films, even though they were fabricated under the same conditions. The primary reason was that the steady-state anodization on thin films was too short to have a sufficient structure rearrangement. Therefore fabricating PAA thin films with a highly ordered porous structure remains a challenge for future studies.

2.8 Nanoparticle Growth by Thin-Film PAA

A useful application of PAA films is to serve as a porous template for patterning nanocomposites such as nanowires and nanoparticles. With a PAA thin film, semiconducting or metal materials can be directly deposited into the alumina pores to form nanoparticles. The experiment in this section demonstrated this templating functionality.

The aluminum samples were prepared as follows: a 300-nm-thick low-stress Si_3N_4 was deposited on a silicon substrate, followed by a deposition of high-purity (99.999%) aluminum for a final thickness of 150 nm. The anodization was performed in 0.3 M oxalic acid with a dc voltage of 40 V at room temperature. The formed PAA was under a pore widening in 5% H_3PO_4 for 50 min at room temperature. Au (Research and PVD Material, Corp) was evaporated on the PAA film at 2 Å sec^{-1} for 200 nm. The sample was cleaved manually and the cross section along the newly exposed edge was inspected under SEM.

Figure 2.14 shows the SEM image of the cross section from a 45° viewing angle. Au particles were formed in the alumina pores, each of them being encapsulated in a single pore. The particle size was ~65 nm in diameter. The alumina pores were eventually sealed by Au on the top, but the covering layer remained disconnected with the particles in the pores. The covering layer could be lifted off by etching the PAA template in acids. Nanoparticles made from the PAA template are advantageous for their small size, uniformity, physical isolation, and large area distribution. They can be useful in the electronic devices such as nanocrystal memory.[150]

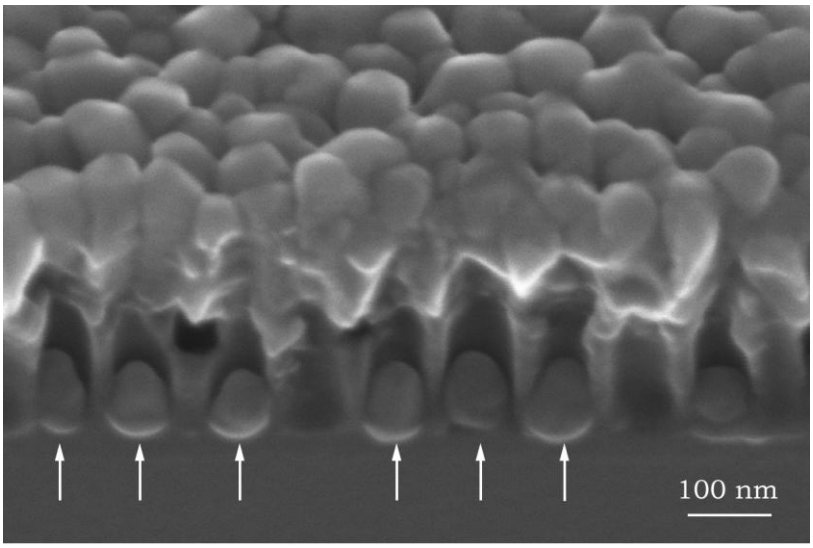

Figure 2.14. Nanoparticles in PAA Pores. The SEM image shows the Au nanoparticles (pointed by arrows) fabricated in the 150-nm-deep PAA pores by depositing Au on the PAA template. The particles were ~65 nm in diameter.

2.9 Tortuous PAA by Low-Voltage Anodization

PAA pores are known for their straight channel profile. Pores are in a cylindrical shape, being parallel to each other. Adjacent pores are fully isolated from each other, having no interconnections with the surrounding pores. Here two PAA thin films featured with ultra small pore sizes (<10 nm) and tortuous channel paths were achieved at low anodizing voltages (5-10 V).

The aluminum samples were prepared as follows: a 300-nm-thick low-stress Si_3N_4 film was deposited on a silicon substrate, followed by a deposition of high purity (99.999%) aluminum for a final thickness of 1200 nm. PAA films were made from the following two conditions: (1) 0.3 M oxalic acid with a dc voltage of 10 V at room temperature; (2) 0.3 M sulfuric acid with a dc voltage of 5 V at room temperature. No pore widening process was applied after the anodizations. SEM images were taken from the bottom side and the cross section of the PAA films (refer to Chapter.3 for the method details of imaging from the backside of the PAA films).

Figure 2.15 (A) and (B) show the bottom view of the PAA films fabricated under the condition sets (1) and (2), respectively. As seen in the figure, these pores were very small. For the condition set (1), the average pore diameter was 8.5 nm, with an inter-pore distance of 30 nm. For the condition set (2), the average pore diameter was 7 nm, with an inter-pore distance of 20 nm. With such a small inter-pore distance, the pore packing density was rather high, being on the order of 10^{13} cm^{-2}.

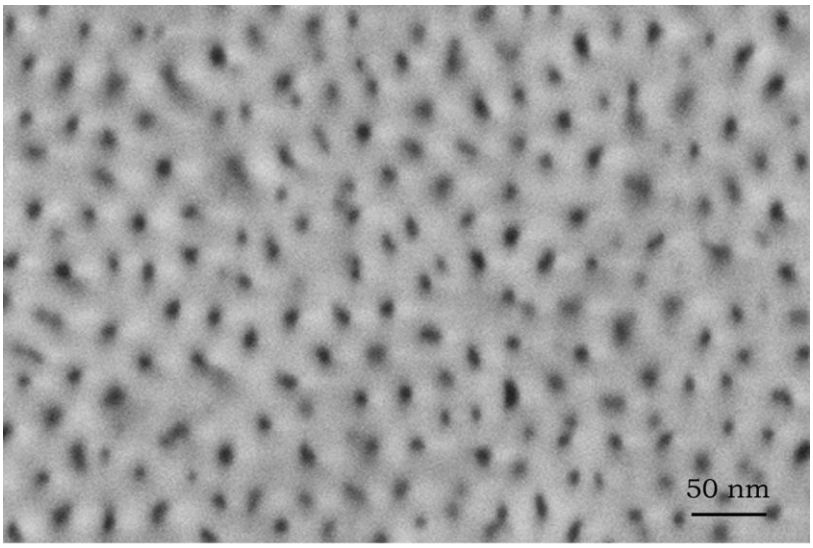

(A)

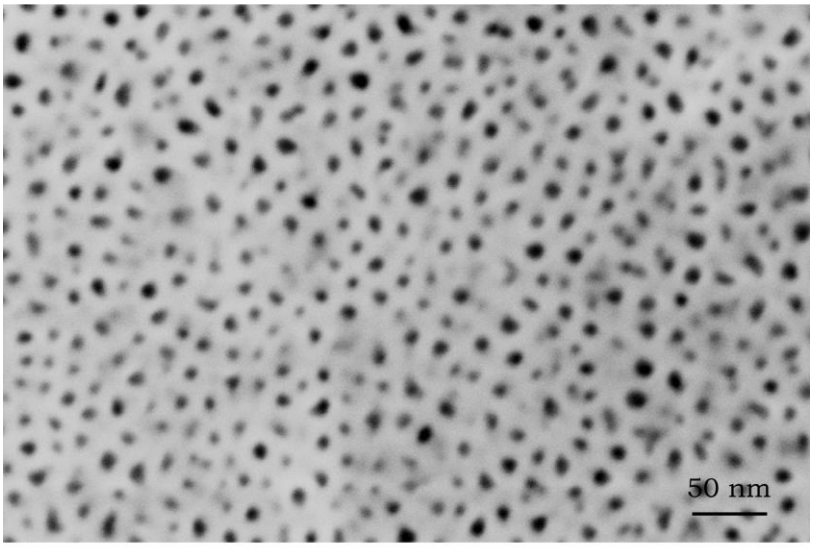

(B)

Figure 2.15. Low-Voltage PAA Thin Films (1). (A) The SEM image of the top surface of a PAA film fabricated in 0.3 M oxalic acid at 10 V. (B) The SEM image of the top surface of a PAA film fabricated in 0.3 M sulfuric acid at 5 V.

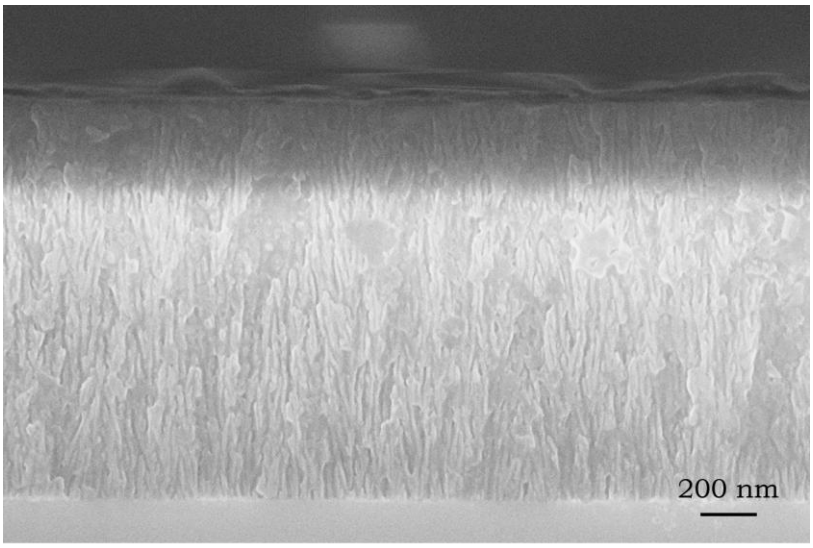

(A)

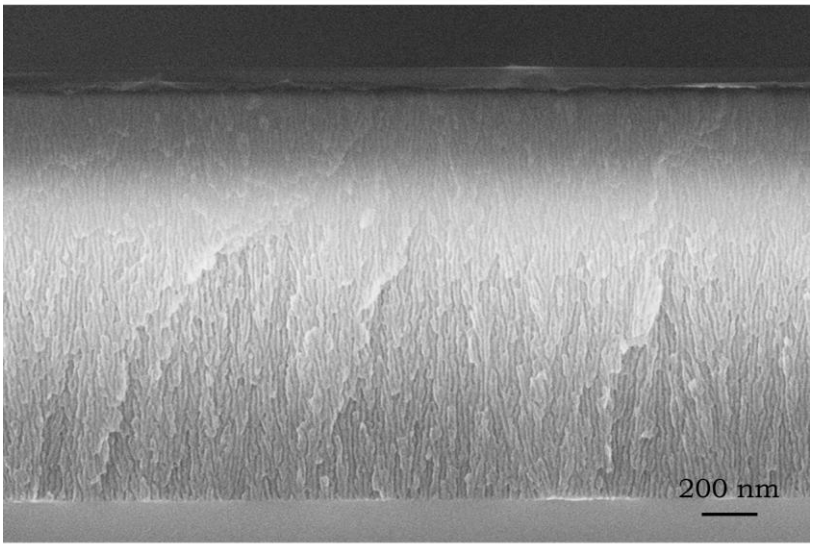

(B)

Figure 2.16. Low-Voltage PAA Thin Films (2). (A) The SEM image of the cross section of a PAA film fabricated in 0.3 M oxalic acid at 10 V. (B) The SEM image of the cross section of a PAA film fabricated in 0.3 M sulfuric acid at 5 V.

The channel profiles of these two membranes are shown as Figure 2.16 (A) and (B), respectively. Instead of being the typical cylindrical tubes, the low-voltage PAA pores presented unique pore paths with certain degree of tortuosity. Along the pore growth, the pores bifurcated into multiple pore branches, or merged with other pores, forming a complex porous matrix. No pores penetrated through the membrane as the normal cylindrical alumina pores. The tortuous paths were possibly introduced by "pore pacing". Ideally all the pore bottoms were at the same depth. However, due to the surface roughness and the random initiations, the pore bottoms in reality might not be ideally synchronized to the same depth. In other words, some pore bottoms might be slightly deeper or shallower than others. This small difference might not affect much the growth of large pores as the depth difference was much smaller than the pore size. But for small pores as reported here, the depth difference was relatively much more significant. Therefore these small pores were more likely to steer their growth direction along the propagation, due to the unbalanced growth with their neighbor pores. However, although the pore paths were not straight, the overall direction of the pore growth was still vertical to the substrate.

Low-voltage PAA thin films are potentially useful. The ultra small pore sizes will be helpful for achieving finer molecular separations. The tortuous pores can possibly enhance the chromatographic effects, thus improving the separation efficiency. With these low-voltage PAA films, nanocomposites such as nanoparticles will be realized with a smaller size and a higher pattern density.

CHAPTER 3

FREESTANDING THIN-FILM POROUS ANODIC ALUMINA

3.1 Background

PAA has been of great interest for its unique nanoporous structure. The typical anodization process is done by applying a positive dc bias on an aluminum substrate in an acidic electrolyte such as sulfuric acid, phosphoric acid or oxalic acid.[3,57,76] During the anodization cylindrical pores are formed and densely packed in a hexagonal array with the pore axis perpendicular to the surface. The pore diameter ranges from sub-10 nm[2] to hundreds of nm,[3] primarily determined by the anodization voltage and the electrolyte type. Because of its unique structure and excellent stability, PAA has been widely used as a porous template in nanomaterial syntheses[125,151-160] as well as in biochemical analyses.[29-31,40,45-52,161] In general, PAA films can be categorized into two domains in terms of the film thickness. Thick-film PAAs are usually made from bulk aluminum substrates such as aluminum foils, having a thickness from tens to hundreds of μm. Although the anodization of thick-film PAAs usually takes long time,[56,57] it can produce highly ordered structures. For their monodisperse nanopores and high aspect ratio, thick-film PAAs are favorable for applications such as gas filtrations[20-26] and biological separations.[29,31,33,40] In comparison, thin-film PAAs have a thickness typically from tens of nm to the micrometer scale. Substrates for thin-film PAAs are often made by depositing aluminum on silicon chips using nanofabrication facilities. Since E-beam lithography is inefficient in throughput, thin-film PAAs presents as a cheap and efficient approach to fabricate nanoscale patterns on silicon substrates, which

has attracted great interest in nanoscience in recent years.[40,155,159,162-164] Normally PAAs are firmly attached to their substrates after the anodization and a U-shaped oxide barrier is formed at the pore bottoms. However, for most applications freestanding PAAs with through holes are desired. The barrier oxide needs to be removed to achieve open pores. Therefore, how to strip PAA films from their substrate becomes a critical step in the fabrication of freestanding PAA films. Among the four methods reported previously, the mostly used method is chemical dissolution.[1] In this method, a high-purity aluminum foil was partially anodized and the residual aluminum substrate was dissolved in $HgCl_2$ solution. The barrier oxide was etched in a diluted H_3PO_4 solution, resulting in a freestanding PAA film. However chemical dissolution was usually used for thick-film PAAs. Plus, heavy metal (Hg) was generated during the process. To reduce the environmental contamination, $CuCl_2$ was used as a substitute for $HgCl_2$.[165] The other three methods, voltage reduction,[62] voltage pulse,[2,63] and voltage reversal[64] all relied on the voltage adjustments in the anodization process. In the voltage-reduction method, the bias voltage was progressively reduced, causing a perforation of the barrier oxide, which separated the PAA film from the substrate. In the voltage-pulse method, a normal anodization was performed first and the separation of the PAA film was achieved by applying a voltage pulse of 10–15 V higher than the anodization bias in a concentrated $HClO_4/(CH_3CO)_2$ solution for a few seconds. In the voltage-reversal method, a negative voltage (3.5 to 5 V) was applied to the PAA film for minutes in the same electrolyte immediately after the

anodization. The PAA film could be detached from the substrate by the voltage reversal but voids and cracks were introduced at the interface between the PAA film and the substrate.

In this chapter, two methods are introduced for fabricating freestanding PAA thin films based on silicon substrates. In the first method, a silicon substrate was coated with a Si_3N_4 layer on both sides. The Si_3N_4 layer on the backside was patterned with an opening window. KOH anisotropically etched the silicon substrate through the opening window until it reached the front Si_3N_4 layer. A PAA thin film was then fabricated on the front Si_3N_4 layer. Finally, the supporting Si_3N_4 layer was removed by CF_4 reactive ion etch, achieving a partly freestanding PAA film over the opening window. The second method, namely, double-layer anodization (DLA), was able to produce partly or fully freestanding PAA films. In the DLA, a sacrificial metal layer (SML) was deposited on a Si_3N_4-Si substrate, followed by an aluminum deposition and a subsequent anodization. After the aluminum layer was depleted the anodization penetrated through the thin barrier oxide, continuing to oxidize the SML layer. During the SML anodization the PAA was spontaneously detached from the Si_3N_4-Si substrate, forming a freestanding film in the electrolyte. The pore opening was realized by removing the barrier oxide using either H_3PO_4 wet etch or CF_4 dry etch. The nanoporous pattern of the PAA was transferred to a silicon substrate using the freestanding PAA as an etch mask. By patterning the SML, a partly freestanding PAA film was fabricated on the top of a microfluidic channel, forming a unique hybrid of microscale and nanoscale structures.

3.2 Methods

3.2.1 Partly Freestanding PAA on Silicon

4-inch double-side polished silicon wafers with an orientation [100] (Silicon Quest, Inc) were cleaned in APM ($NH_4OH:H_2O_2:H_2O$ =1:1:6 at 70 °C) for 10 min and in HPM ($HCl:H_2O_2:H_2O$ =1:1:6 at 70 °C) for 10 min. A 250-nm-thick low-stress Si_3N_4 film was deposited on the silicon substrate by LPCVD ($DCS:NH_3$=84:22 sccm, 200 mTorr, 800 °C). Photoresist S-1818 (Shipley, Corp) was spun on the backside at 4000 rpm for 30 sec, and baked at 90 °C for 60 sec. A square window of 0.97 mm by 0.97 mm was patterned by the contact UV exposure of the photoresist at 12 mW cm^{-2} for 7 sec, followed by the development in 300 MIF (AZ Electronic Materials, Corp) for 60 sec. After removing the Si_3N_4 layer within the window area by CF_4 reactive ion etch (chamber pressure: 40 mTorr, RF power: 150 watts, CF_4 flow rate: 30 sccm; etch time: 15 min), the exposed silicon substrate was etched in 40% KOH (Mallinckrodt Baker, Inc) at 95 °C for hours until it was stopped at the front Si_3N_4 layer. The etched region was shaped as a truncated pyramid with a front window of 900 μm by 900 μm. High-purity (99.999%) aluminum (Research and PVD Material, Corp) was evaporated on the front side at 5 Å sec^{-1} for 1200 nm. The anodization was performed at one of the optimal conditions reported,[3] briefly, in 0.3 M oxalic acid at a dc bias of 40 V, until the entire aluminum film was converted to alumina. The sample was rinsed with dH_2O thoroughly and soaked in 5% H_3PO_4 for 40 min to widen the pores and remove the barrier oxide. After rinsed with dH_2O and dried under N_2

gas flow, the sample was etched from the backside by the CF_4 dry etch for 15 min (chamber pressure: 40 mTorr, RF power: 150 watts, CF_4 flow rate: 30 sccm), in order to remove the supporting Si_3N_4 layer to achieve a partly freestanding PAA film over the window. The fabrication process flow is shown as Figure 3.1.

3.2.2 Double-Layer Anodization

(1) Fully Freestanding PAA Thin Film

4-inch double-side polished silicon wafers with an orientation [100] (Silicon Quest Inc.) were cleaned in APM (NH_4OH: H_2O_2:H_2O=1:1:6 at 70 °C) for 10 min and in HPM (HCl:H_2O_2:H_2O=1:1:6 at 70 °C) for 10 min. A 300-nm-thick low-stress Si_3N_4 film was deposited on the silicon substrate by LPCVD (DCS :NH_3=84:22 sccm, 200 mTorr, 800 °C).

Cu or Ag (Research and PVD Material, Corp) was evaporated on the Si_3N_4 at 1 Å sec^{-1} for 50 nm, followed by a deposition of high-purity (99.999%) aluminum at 5 Å sec^{-1} for 200 nm. The fabrication flow is shown in Figure 3.2 (A)-(C).

The Si_3N_4-Si substrate coated with the metal films was cleaned with acetone, isopropanol, and dH_2O, followed by drying under N_2 gas flow. Double-layer anodization was performed at a constant dc bias of 20 V in 0.3 M H_2SO_4 solution (Mallinckrodt Baker, Inc) at 10°C, at which an ordered structure was reported.[3] Under these conditions, the anodization took a couple of minutes to complete. The current-time profiles are shown in Figure 3.4. At the end of the process the dc current decreased rapidly and a significant color change occurred on the sample surface. The PAA film was detached from the substrate

during the oxidation of the SML. Depending on the SML material used (Cu or Ag), two types of PAA films were made in the DLA, named as Cu-PAA and Ag-PAA, respectively. After the anodization the PAA films were transferred on to a silicon substrate with the bottom side up, carefully rinsed with dH_2O, and dried under N_2 gas flow.

The barrier oxide layer on the Cu-PAA was removed by soaking the PAA film in 5% H_3PO_4 (Mallinckrodt Baker, Inc) for 10 min at room temperature. After the H_3PO_4 treatment the PAA film was rinsed with dH_2O and dried under N_2 gas flow. The barrier oxide on the Ag-PAA was removed by performing an additional CF_4 dry etch for 15 min (chamber pressure: 40 mTorr, RF power: 150 watts, CF_4 flow rate: 30 sccm).

The Cu-PAA on the silicon substrate was used as a contact mask to demonstrate the pattern transfer. After the H_3PO_4 treatment, the sample was under the CF_4 dry etch for 15 min (chamber pressure: 40 mTorr, RF power: 175 watts, CF_4 flow rate: 30 sccm), similar to the pore-opening process for the Ag-PAA. After the CF_4 etch the Cu-PAA film was removed by soaking the sample in 5% H_3PO_4 for 4 hours at room temperature. SEM images were taken from the rest silicon substrate to verify the pattern transfer. The process flow of the pattern transfer is shown as Figure 3.2. (E)-(H).

(2) Partly Freestanding PAA Thin Film

4-inch double-side polished silicon wafers with an orientation [100] (Silicon Quest Inc.) were cleaned in APM (NH_4OH: H_2O_2:H_2O=1:1:6 at 70 °C) for 10 min and in HPM (HCl:H_2O_2:H_2O=1:1:6 at 70 °C) for 10 min. A 300-nm-thick low-stress Si_3N_4 film was deposited on the silicon

substrate by LPCVD (DCS :NH_3=84:22 sccm, 200 mTorr, 800 °C).

LOR-5A (MicroChem, Corp) was spun on the Si_3N_4-Si substrate at 4000 rpm for 30 sec, and baked at 180 °C for 5 min. The photoresist S-1818 was spun on the LOR-5A at 4000 rpm for 30 sec, and baked at 90 °C for 60 sec. A 4-μm-wide trench were patterned by the contact UV exposure at 12 mW cm^{-2} for 7 sec, followed by the development in 300 MIF for 60 sec. Cu was evaporated on the substrate at 5 Å sec^{-1} for 200 nm and lifted off by the incubation in the remover 1165 (Rohm and Haas Electronic Materials, LLC) overnight, forming a 4-μm-wide Cu line on the substrate. High-purity (99.999%) aluminum was deposited on the substrate at 5 Å sec^{-1} for 200 nm, conformally covering the Cu line. The schematic of the fabrication is shown as Figure 3.3.

The Si_3N_4-Si substrate coated with the metal films was cleaned with acetone, isopropanol, and dH_2O, followed by drying under N_2 gas flow. Double-layer anodization was performed at a constant dc bias of 20 V in 0.3 M H_2SO_4 solution. After the anodization, the sample was rinsed with dH_2O and dried under N_2 gas flow.

The barrier oxide layer on the sample was removed by soaking the PAA film in 5% H_3PO_4 for 10 min at room temperature. After the H_3PO_4 treatment the PAA film was rinsed with dH_2O and dried under N_2 gas flow.

To verify that the Cu line was anodized as the sacrificial layer, producing a partly freestanding PAA structure on the top, the sample was cleaved across the line and inspected under SEM.

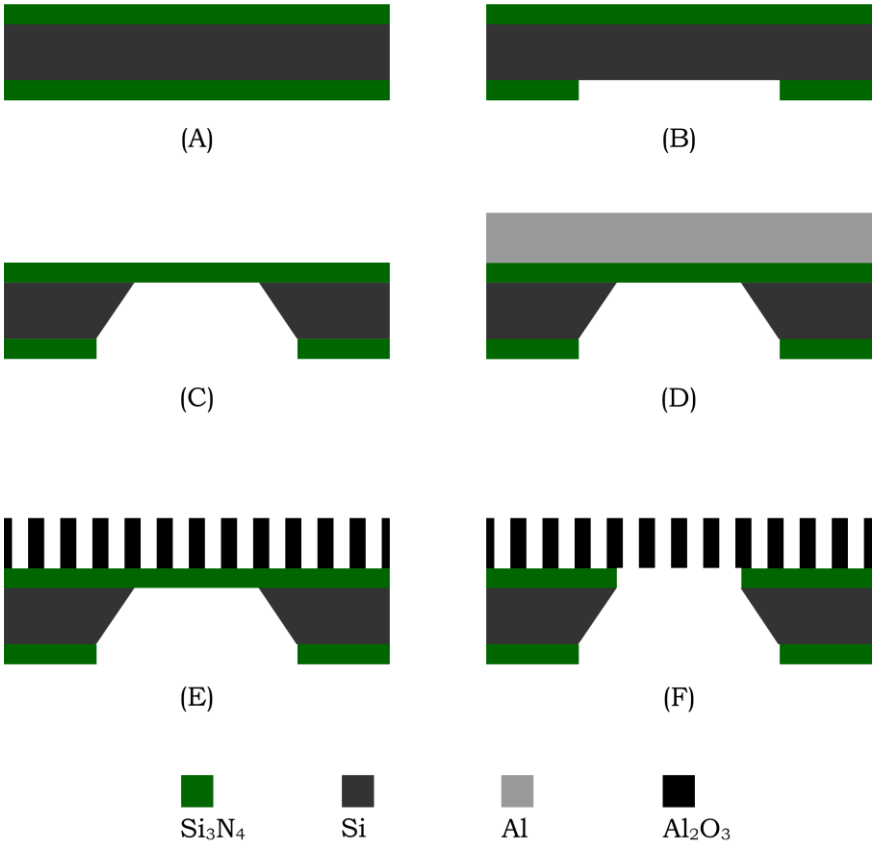

Figure 3.1. Fabrication of Partly Freestanding PAA. (A) A Si substrate coated with a 250-nm-thick Si_3N_4 film by LPCVD. (B) The Si_3N_4 patterned by CF_4 dry etch on the backside. (C) The bulk Si removal by KOH anisotropic etch. (D) A 1.2-μm-thick Al deposited on the front side. (E) The Al anodization, producing a PAA film on the top. (F) A freestanding PAA structure, achieved by removing the supporting Si_3N_4 layer from the backside by CF_4 dry etch.

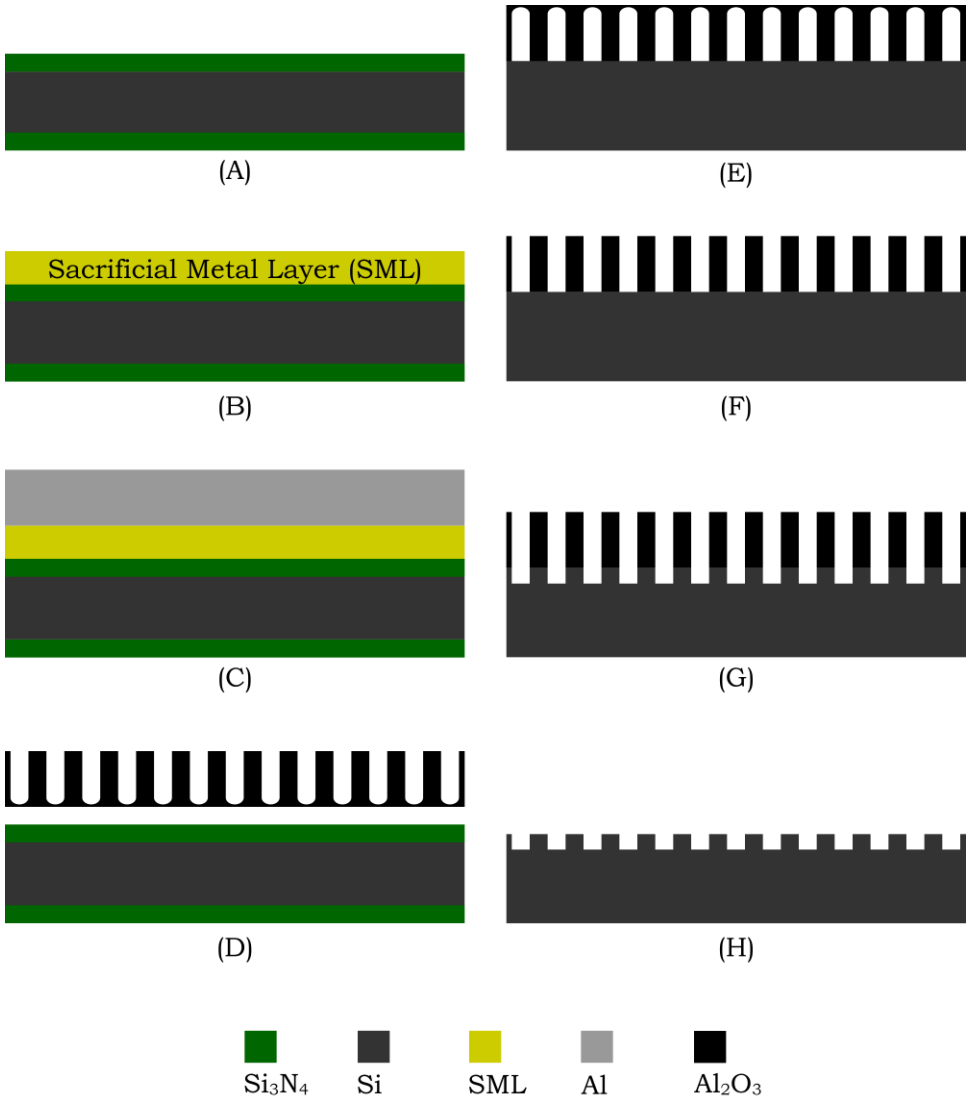

Figure 3.2. Fabrication of Fully Freestanding PAA by DLA. (A) A Si substrate coated with a 300-nm-thick Si_3N_4 film as a protection layer. (B) A sacrificial metal layer (Cu or Ag) deposited on the Si_3N_4-Si substrate. (C) A 200-nm-thick Al deposited on the sacrificial layer. (D) A PAA film produced by the Al anodization, detached from the substrate during the anodic oxidation of the sacrificial metal layer. (E) The freestanding PAA transferred onto a Si substrate with bottom side up. (F) The barrier layer removal by H_3PO_4 wet etch (for Cu-PAA) or by CF_4 dry etch (for Ag-PAA). (G) The transfer of the porous pattern of the Cu-PAA to the Si substrate by CF_4 dry etch. (H) The removal of the PAA mask by H_3PO_4 wet etch.

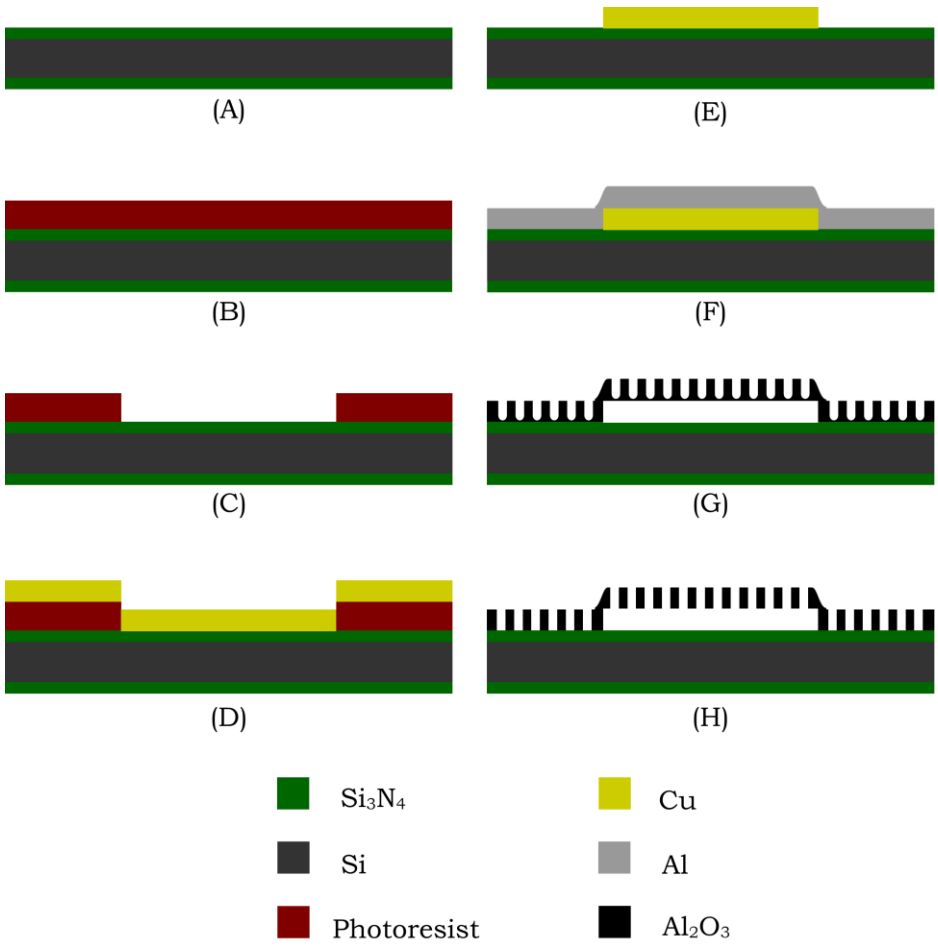

Figure 3.3. Fabrication of Partly Freestanding PAA by DLA. (A) A Si substrate coated with a 300-nm-thick Si_3N_4 film as a protection layer. (B) LOR-5A and the photoresist S1818 spun on the Si_3N_4 substrate. (C) The photoresist patterned with a 4-μm-wide trench. (D) The deposition of 200-nm-thick Cu on the photoresist. (E) A Cu line formed by the lift-off process. (F) A 200-nm-thick Al conformally deposited on the substrate. (G) A partly freestanding PAA film formed on the top of a microfluidic channel by the DLA process. (H) The removal of the barrier oxide by H_3PO_4 wet etch.

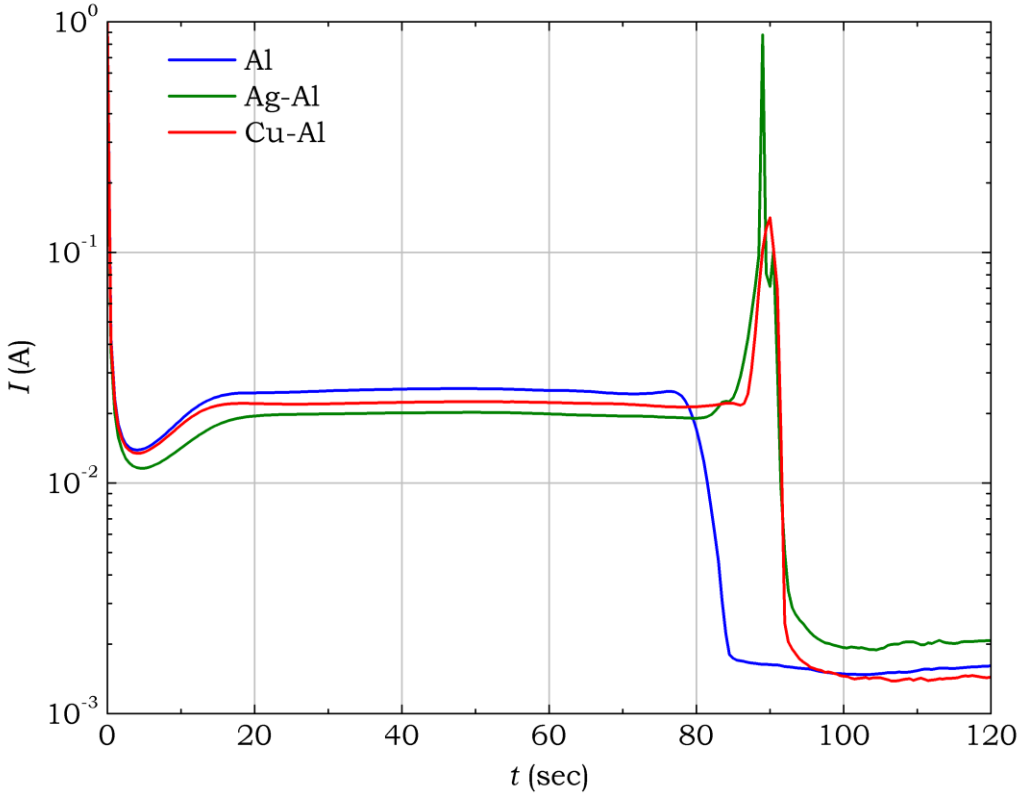

Figure 3.4. I-t Curves of DLA. The I-t curves were obtained in real time during the anodization of three different samples: A single Al layer (blue), a double layer of Ag-Al, and a double layer of Cu-Al. The thickness of Al, Ag, and Cu was 200 nm, 50 nm, and 50 nm, respectively. The flatland between 15 sec and 80 sec corresponded to the steady-state Al anodization. For a single Al layer the current decreased rapidly after 80 sec due to the Al depletion. For Ag-Al or Cu-Al, a sharp current peak occurred at ~90 sec, corresponding to the anodization of Ag or Cu. Each sample had an anodization area of ~3 cm^2.

3.3 Results and Discussion

Fabrication of freestanding PAA films with open pores is challenging as PAA films attach firmly to their substrates. The freestanding PAA film fabricated by the first method here was supported by a Si_3N_4-Si substrate. An opening window was first patterned on the Si_3N_4 layer on the backside, followed by removing the silicon substrate by KOH anisotropic etch. Finally, the Si_3N_4 supporting layer on the front side was removed by CF_4 reactive ion etch. SEM images were taken from the sample's backside to verify that the alumina pores were opened after the CF_4 dry etch (Figure 3.5). The 90° corner structure in the image was the intersection of two silicon [111] planes generated by the anisotropic KOH etch. Because KOH had a high etch selectivity[149] between the silicon orientation [100] and [111] (~600), it etched the [100] planes and stopped at [111] planes. The Si_3N_4 layer served for two purposes in the fabrication. First, it defined the opening window by protecting the bulk silicon substrate during the KOH etch. The KOH etch only attacked the silicon substrate but not the Si_3N_4 film. The 300-nm-thick Si_3N_4 film was sufficient to sustain in the KOH etch at 95 ºC until the silicon substrate was etched through. Second, it served as a supporting layer to hold the deposited aluminum film. After the anodization this supporting layer needed to be removed to achieve a freestanding PAA film over the window. It was important to remove this Si_3N_4 layer only after the aluminum film was converted to the alumina. Because the Si_3N_4 layer benefitted to the Al_2O_3-Al film for resisting against the thermal stress introduced during the anodization.

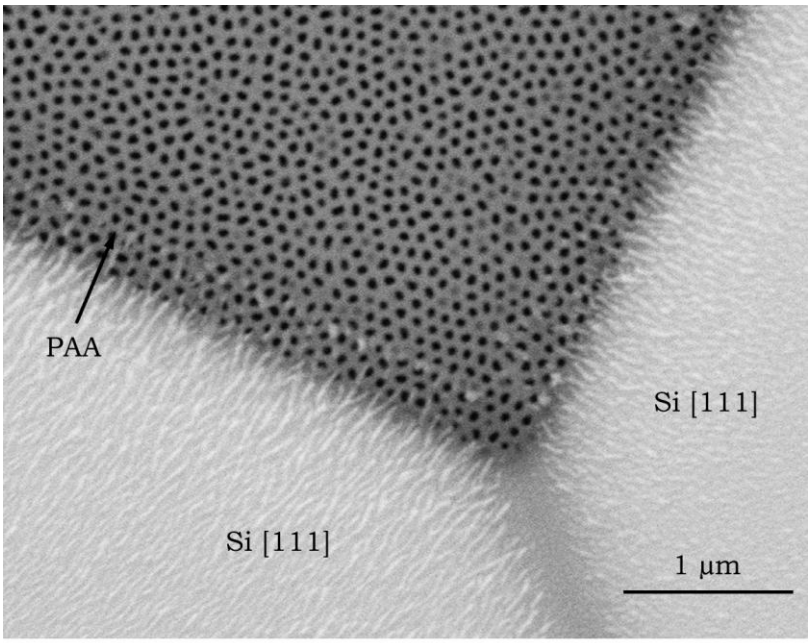

Figure 3.5. SEM Image of Partly Freestanding PAA. The image was taken from the backside of the freestanding PAA shown as Figure 3.1 (F). The PAA pores were verified to be open after the supporting Si_3N_4 layer was removed by CF_4 dry etch. The 90° corner structure was formed by the intersection of two Si [111] planes, which were generated by the KOH anisotropic etch.

In addition, if this Si_3N_4 layer was removed prior to the anodization, the aluminum film would be anodized from both sides simultaneously. Since the pore positions were randomly initialized on the surface, pores generated from two sides would not be aligned to each other, probably resulting in many blind holes.The fabrication of the partly freestanding PAA film by this method was relatively simple. It utilized the KOH anisotropic etch to remove the bulk supporting substrate. The CF_4 dry etch served as an efficient approach for removing the barrier oxide layer. The etch was performed directly from the bottom side of the pores. All the pores were well opened after the CF_4 etch. The freestanding part over the window had a high aspect ratio of width to height, ~1000. The freestanding PAA was visually transparent. This freestanding structure on the silicon substrate served as an excellent model of thin-film PAA filter on chip. It would be interesting to the future on-chip applications.

The freestanding PAA structure by this method was reported by Toh et al.,[163] as well as the author of this dissertation and his colleagues.[166] The latter group also used this structure in their investigations of molecular diffusions in nanopores.[167]

The second method, DLA, was a continuous anodization of two deposited metal films for the purpose of releasing the PAA from the substrate. Figure 3.4 shows the current-time profiles recorded during the anodization process. The blue curve was the anodization of 200-nm-thick aluminum directly on Si_3N_4 substrate. After the initialization step, a steady-state anodization lasted from t=15 s to t=80 s, during which the aluminum film was oxidized to a PAA. After t=80 s the

aluminum film started to be depleted and the current decreased to the leakage current level in a few seconds and the anodization reached the completion point. The DLA processes of Ag-Al and Cu-Al were presented as the green and red curves, respectively. Their profiles were similar to the blue curve before t=80 s because the aluminum films used in these processes were the same. After the aluminum was depleted, the DLA current increased by 1–2 orders of magnitude and then dropped back to the completion point, forming a current peak around t=90 s. These current peaks indicated the electrochemical oxidations of the sacrificial films (Ag and Cu). For a thickness of 50 nm, the anodization of Ag and Cu was mainly done in 2 and 4 s, respectively. Therefore in Figure 3.4 the green curve had a sharper current impulse and a higher peak value than the red curve.

In the previous reports,[64,156] a similar structure, Ti-Al, was used in the PAA preparations, and the Ti oxidation was also observed. However, in those applications the motivation of inserting a Ti layer was to improve the adhesion between the aluminum film and the substrate. The PAAs fabricated by their approaches were firmly attached to the substrates through a TiO_2 layer. In the experiments here it was noticed that either the aluminum film or the PAA adhered well to the Si_3N_4 substrate. No adhesive layer was needed. In the DLA, Ag or Cu served two different purposes. First, it acted as a conductive sheet to ensure a uniform and complete aluminum anodization. Second, upon its own oxidation it promoted the separation of the PAA film from the Si_3N_4 substrate, due to the weak adhesion of Ag_2O or CuO. The anodization of the SML layers was similar to the field-

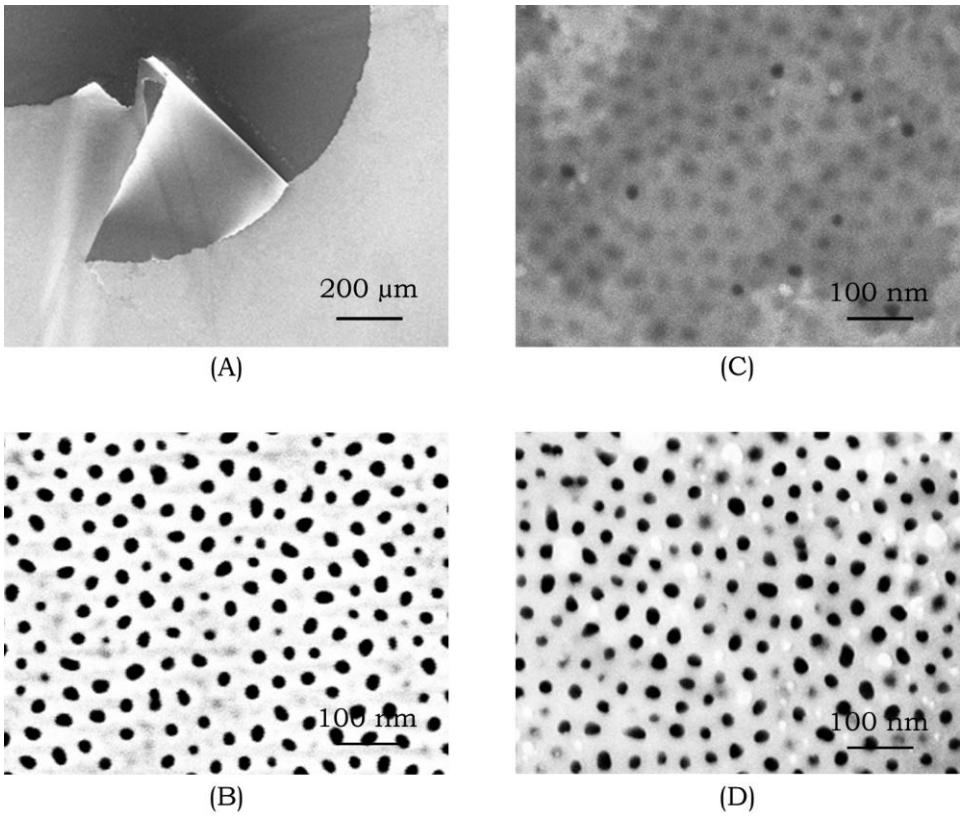

Figure 3.6. Fully Freestanding PAA Films by DLA. (A) A freestanding PAA made by DLA. The film was torn to show its freestanding structure. (B) The backside of Cu-PAA after 10-min H_3PO_4 etch, showing that the pores were opened. (C) The backside of Ag-PAA after 10-min H_3PO_4 etch, showing that the most pores were still closed. (D) The Ag-PAA pores opened by an additional CF_4 dry etch.

assisted oxidation of aluminum, having the following reactions:

$$Cu+2OH^{-}=CuO+H_2O+2e \quad (3.1)$$

$$Ag+2OH^{-}=Ag_2O+H_2O+2e \quad (3.2)$$

In the DLA, the barrier oxide of the PAA film might consist of two components: the native Al_2O_3 barrier oxide and the SML oxide (CuO or Ag_2O). To minimize the latter type, H_2SO_4 was used as the electrolyte because metal oxides generally have a higher solubility in H_2SO_4 than the other common electrolytes such as H_3PO_4 and $(COOH)_2$. As shown in Figure 3.6 (B), the pores on the Cu–PAA were well opened after the H_3PO_4 etch, with no barrier layer observed. In comparison, most pores on the Ag–PAA were still closed (Figure 3.6 (C)). This was possibly because Ag_2O had a lower solubility in H_2SO_4 or H_3PO_4 than CuO. It remained on the PAA even after the H_3PO_4 treatment. However, this barrier oxide could be effectively removed by an additional CF_4 dry etch (Figure 3.6 (D)). The CF_4 etch here was referenced from a process for etching Si or SiO_2. Its cleaning effects on Ag-PAA were presumably due to the high-energy bombardment by the reactive ions generated in the RF plasma.

Besides Cu and Ag, Ni was also tested as the SML as its oxide had a reasonable solubility in H_2SO_4. But the combination of Ni-Al failed to produce a freestanding PAA as voids and cracks were generated on the surface during the DLA process, preventing a uniform detachment of the PAA from the substrate. It was possibly because of the relatively high chemical activity of Ni in comparison with Cu and Ag. The voids and cracks were introduced probably as a result of the intensive

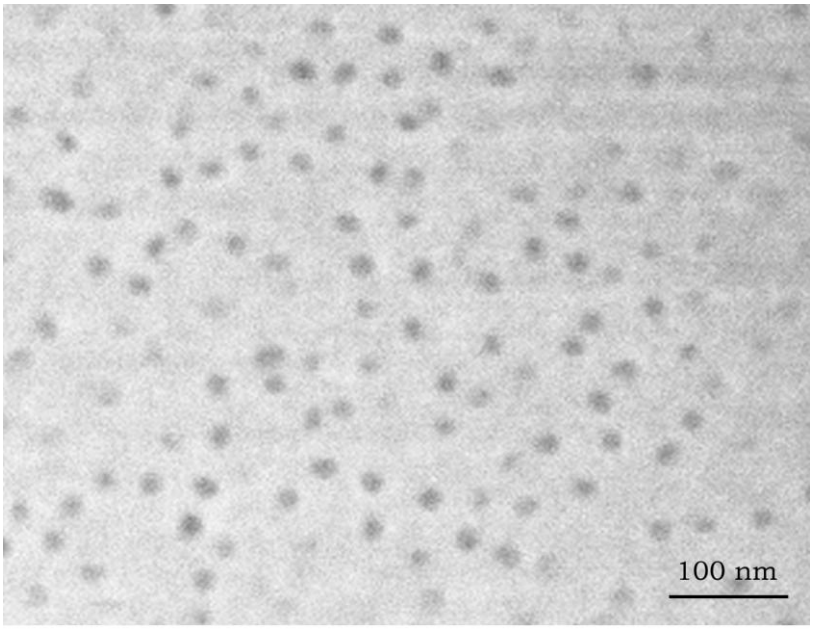

Figure 3.7. Pattern Transfer by Freestanding PAA. The SEM image shows a Si substrate transferred with a porous pattern from a Cu-PAA freestanding film. The Si substrate was under the CF_4 dry etch for 15 min, covered with the Cu-PAA film. Afterwards, the Cu-PAA film was removed by soaking the sample in 5% H_3PO_4 for 4 hours.

oxidation of Ni under the described anodization conditions.

To be used as an etch mask, the Cu–PAA (Figure 3.6 (B)) was transferred onto a silicon substrate and etched by CF_4 for 15 min. The Cu–PAA was then removed by a long soaking in 5% H_3PO_4. The nanoporous pattern of the Cu-PAA was successfully transferred to the silicon substrate, as shown in Figure 3.7. Generally, if the substrate was compatible with the aluminum deposition and the anodization process, the direct transfer with an attached PAA film was straightforward.[168,169] Otherwise, the freestanding PAA mask would be preferred should the substrate be sensitive to the aluminum deposition, anodic oxidation, or ionic contamination. Using aluminum foils to make freestanding masks[125,170] had its drawbacks as it required laborious fabrications and generated hazardous chemical wastes. The DLA simplified the production of freestanding PAAs as a one-step anodization, and made the process environmentally safe and fully compatible with nanofabrication.

Another advantage of the DLA was its capability of fabricating partly freestanding PAAs, which were difficult to achieve with the previously reported methods. By slightly changing the double layer structure, a unique microfluidic channel integrated with a partly freestanding PAA film has been demonstrated. The difference from the normal DLA process was that the Cu layer was lithographically patterned to be a 4-μm-wide line, instead of a uniform film over the substrate. The line length was arbitrary, being a few centimeters here. The Cu line was then buried by a conformal deposition of aluminum. The fabrication schematic is shown as Figure 3.3, in a cross-sectional

view. The anodization process was performed under the same conditions as previously described. Afterwards, the device was soaked in 5% H_3PO_4 for 10 min, and subsequently rinsed with dH_2O and dried under N_2 gas flow. The sample was cleaved along the cross section of the Cu line and was inspected under SEM from a 45° viewing angle, shown as Figure 3.8. Region (1) was a single PAA layer that was directly attached to the substrate. The DLA occurred within the line area, producing a microfluidic channel as region (2) due to the depletion of Cu sacrificial layer. The freestanding PAA marked as (3) was left over the channel. In this structure, the lateral channel was connected to the outside through the vertical PAA pores, forming a unique hybrid of microscale and nanoscale structures.

This structure could be used for applications such as drug delivery and patterned cell culture by utilizing the microfluidic channel as an underground pipeline for supplying the drug or media source, and the freestanding PAA film as a speed-limiting layer for controlling the molecular release. The release rate could be tuned by the PAA thickness and the pore size. With a patterned SiO_2 deposition on the PAA film for pore closing, the open area for the molecular release could be further customized. Lastly, this structure could also be interesting to other applications such as size-exclusion filtration and chromatographic separation on chip.[40] The DLA method discussed here was reported on *IEEE Transactions on Nanotechnology* in 2007.[171]

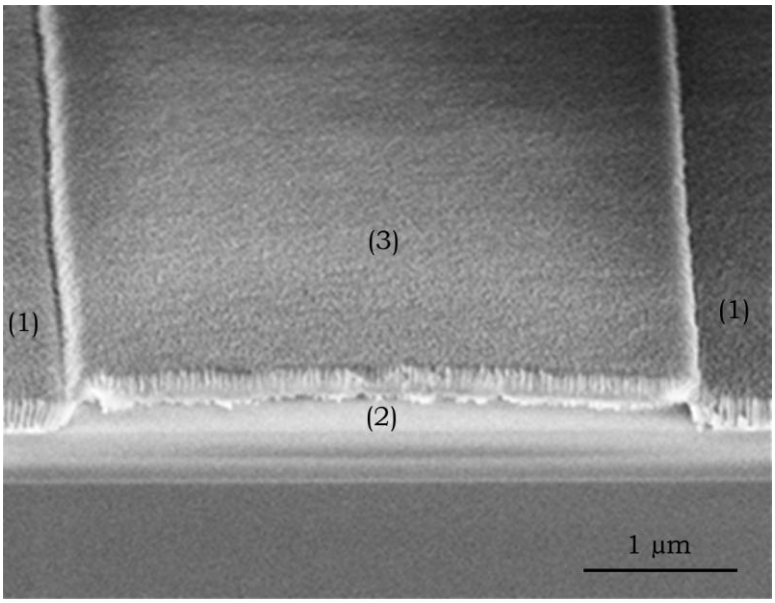

(A)

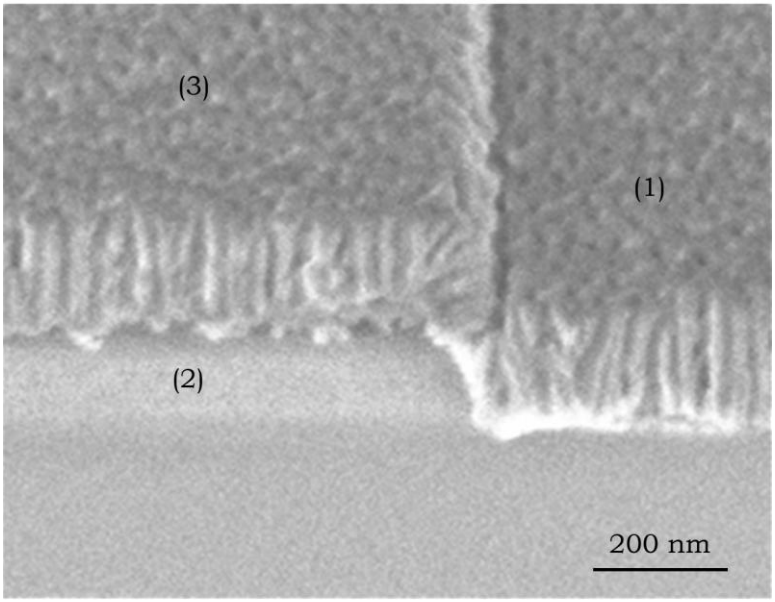

(B)

Figure 3.8. SEM Images of Partly Freestanding PAA by DLA. (A) A partly freestanding PAA formed on the top of a microfluidic channel by DLA. In region (1), the PAA film was formed directly on the substrate. In region (2), a microfluidic channel was formed by the anodization of the sacrificial metal layer. In region (3), a partly freestanding PAA film was formed on the top of the microfluidic channel. (B) A high-magnification view of the microfluidic channel as well as the porous structure of the freestanding PAA film.

3.4 Conclusion

In this chapter, two methods have been developed to fabricate freestanding PAA thin films on silicon substrates. In the first method, the freestanding structure was achieved by removing the silicon substrate from the backside by KOH wet etch. A Si_3N_4 film served as a temporary supporting layer for holding the PAA film. This Si_3N_4 layer, as well as the PAA barrier oxide, was removed by CF_4 anisotropic etch. A freestanding PAA with a width-to-thickness ratio of ~1000 was demonstrated. The structure has been successfully utilized in the molecular diffusion experiments in the next chapter.

The challenge of fabricating freestanding PAA films is essentially the difficulty of stripping of the PAA from the substrate. As a novel method, DLA made this stripping process simple by adding an extra metal layer between the aluminum film and the substrate. The PAA film was automatically detached from the substrate by the anodization of the sacrificial metal layer. The removal of the barrier oxide was done by H_3PO_4 wet etch or CF_4 dry etch. Importantly, DLA was able to achieve freestanding PAA thin films directly on silicon chips, with great flexibilities in pattern designs. This feature will be particularly useful for developing on-chip nanofluidic systems.

For many applications of nanobiotechnology, on-chip freestanding PAA with through pores is simply necessary. Two methods have been developed to address the possible solutions. With the freestanding structures produced by these two methods, more interesting applications will possibly be developed in the future.

CHAPTER 4

DIFFUSION OF SUB-1000-DALTON MOLECULES IN 40-NM ALUMINA NANOPORES

4.1 Background

Anodic alumina is a popular nanomaterial due to its unique porous structure. Its fabrication is achieved by anodizing a high-purity aluminum film in an acidic solution.[1,76] During the anodization, a hexagonal array of cylindrical pores with a uniform size is formed perpendicular to the film surface. Depending on the anodization conditions, the pore diameter ranges from sub-10 nm[2] to hundreds of nm,[3] yielding a pore density as high as 10^{8-11} pores cm^{-2}. The pore length is proportional to the anodizing time, varying from tens of nm to the scale of millimeter.[164,172] As a host material for patterning nanocomposites, anodic alumina has been used in electronic, optical, or magnetic devices.[18,173,174] Nanoparticles and nanowires[155,175] can be effectively realized by filling alumina pores with metals or semiconductors. In recent years, the nanoporous structure of anodic alumina has been increasingly used for the controlled molecular release in diverse fields, particularly, in biology. For example, in cell culture on chip,[41,176] alumina membranes were used as a porous support for the cell growth. Nutrition media were provided from the opposite side and were diffused through the alumina pores. In drug delivery,[34] alumina pores were used for transporting drug molecules with the speed controlled by the pore size. With biochemical modifications, alumina membranes were used for selective separations of drug enantiomers[29] and DNA oligonucleotides.[31] Among these applications, molecules were confined to travel along the nanoscale alumina pores, driven by the concentration gradient across the

membrane. Characterizations of this hindered diffusion are crucial for understanding the fundamentals of the nanofluidics in alumina pores. It can provide valuable information for the study of other nanopores and nanotubes. However, available reports focusing on experimentally characterizing the diffusion dynamics in alumina pores are very limited, despite an abundance of applications using alumina membranes for biosensors and bioseparations. Most reports only presented the characterizations by plotting the amount or concentration of the diffused molecules as a function of time, without having the diffusion coefficient characterized[29,34,35] or assuming the same diffusion coefficient in both pore water and bulk solution.[36] Only a few investigations, such as the diffusion experiments of glucose oxidase[68] and metal ions,[69,70] interpreted the diffusion characteristics in terms of diffusion coefficient.

In this chapter a new diffusion system has been established based on a micrometer-thick freestanding PAA film. The confined diffusion of organic molecules through the alumina pores was investigated, and the diffusion dynamics was characterized using diffusion coefficient and molecular flux. The PAA film with open pores was fabricated on a silicon substrate with a controlled thickness (1.2 μm) and pore size (40 nm). The diffusion course was recorded by monitoring the optical absorbances of the diffused molecules. Due to the well defined porous structure of the PAA film, the diffusion process was modeled as a one-dimensional Fickian flow, from which the characteristic parameter, diffusion coefficient, was calculated. The diffusion behaviors in the nanopores showed to be significantly different from the bulk solution.

4.2 Methods

4-inch double-side polished silicon wafers with an orientation [100] (Silicon Quest, Inc) were cleaned in APM ($NH_4OH:H_2O_2:H_2O$ =1:1:6 at 70 °C) for 10 min and in HPM ($HCl:H_2O_2:H_2O$ =1:1:6 at 70 °C) for 10 min. A 250-nm-thick low-stress Si_3N_4 film was deposited on the silicon substrate by LPCVD ($DCS:NH_3$=84:22 sccm, 200 mTorr, 800 °C). Photoresist S-1818 (Shipley, Corp) was spun on the backside at 4000 rpm for 30 sec, and baked at 90 °C for 60 sec. A square window of 0.97 mm by 0.97 mm was patterned by the contact UV exposure of the photoresist at 12 mW cm^{-2} for 7 sec, followed by the development in 300 MIF (AZ Electronic Materials, Corp) for 60 sec. After removing the Si_3N_4 layer within the window area by CF_4 reactive ion etch (chamber pressure: 40 mTorr, RF power: 150 watts, CF_4 flow rate: 30 sccm; etch time: 15 min), the exposed silicon substrate was etched in 40% KOH (Mallinckrodt Baker, Inc) at 95 ºC for several hours until it was stopped at the front Si_3N_4 layer. The etched region was shaped as a truncated pyramid with a front window of 900 μm by 900 μm. High-purity (99.999%) aluminum (Research and PVD Material, Corp) was evaporated on the front side at 5 Å sec^{-1} for 1200 nm. The anodization was performed at one of the optimal conditions reported,[3] briefly, in 0.3 M oxalic acid at a dc bias of 40 V, until the entire aluminum film was converted to alumina. The sample was rinsed with dH_2O thoroughly and soaked in 5% H_3PO_4 for 30 min to widen the pores and remove the barrier oxide. After rinsed with dH_2O and dried under N_2 gas flow, the sample was etched from the backside by the CF_4 etch for

15 min (chamber pressure: 40 mTorr, RF power: 150 watts, CF_4 flow rate: 30 sccm), in order to remove the supporting Si_3N_4 layer to achieve a freestanding structure over the diffusion window. Finally the sample was diced into individual square chips, with each of them having one diffusion window in the center. The fabrication process flow is shown as Figure 3.1. SEM images were taken from the sample's backside to verify that the alumina pores were opened after the CF_4 dry etch (Figure 4.1). The 90° corner structure in the image was the intersection of two silicon [111] planes generated by the anisotropic KOH etch.

Caffeine, methyl orange (MO), and malachite green oxalate (MGO) (Sigma Aldrich, Co) were prepared in dH_2O with a final concentration of 1 mM, 0.1 mM, and 1.67×10^{-2} mM, respectively. These organic molecules served as the molecular indicators for the diffusion experiments. They were relatively small (<1000 Da) and could be easily detected by their optical absorbance. The chemical structures and the physical properties of these three molecules are shown as Figure 4.2 (A) and Table 4.1, respectively. For the diffusion system, a commercial 12-well cell culture plate (Costar®) was used as the base of the diffusion device. The culture plate consisted of an outer well and a small insert. The insert originally had a polycarbonate membrane at the bottom. For the diffusion experiment, the membrane was manually removed by tweezer. A PAA filter chip was attached to the bottom of the insert using instant glue. The device was left at room temperature over night to let the instant glue completely dry, as residual instant glue was found to have severe interferences on the absorbance

measurements. The insert was carefully placed in a well in the plate. 150 μl of dH_2O was added into the insert, pre-wetting the PAA film for 5 min with encapsulation. Afterwards, 1 ml of the prepared diffusion sample was loaded into the well. The schematic of the diffusion device is shown as Figure 4.2 (B). The device was covered with the lid and encapsulated with Parafilm and aluminum foil, to minimize the water evaporation and the exposure to light. The device was left at room temperature for days without stirrings. The concentration of the molecules diffused into the insert was monitored by the absorbance measurements over time. For taking the absorbance measurement, 100 μl of the solution in the insert was transferred to a 96-well plate by pipette. The absorbances of caffeine, MO, and MGO were read by a spectrophotometer (SpectraMax®, Plus384) at 285 nm, 465 nm, and 620 nm, respectively. The absorbance was approximately linear to the concentration of the diffused molecules. Each time the absorbance reading took ~2min. Afterwards the solution was immediately transferred back into the insert, resuming the static diffusion with encapsulation. Since the entire diffusion course lasted for days, and the interval between two consecutive readings was at least several hours, the delay of the diffusion caused by the absorbance measurement was negligible. For the negative control, an insert was attached with a blank silicon chip using instant glue and left over night. The same diffusion experiment was performed on this device. Any detected diffusion in the device would be due to the molecular leakage between the insert and the silicon chip.

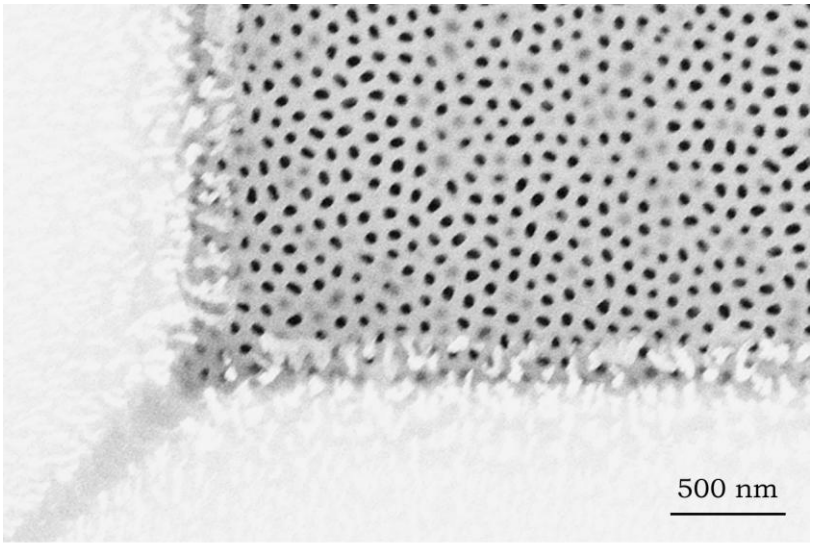

(A)

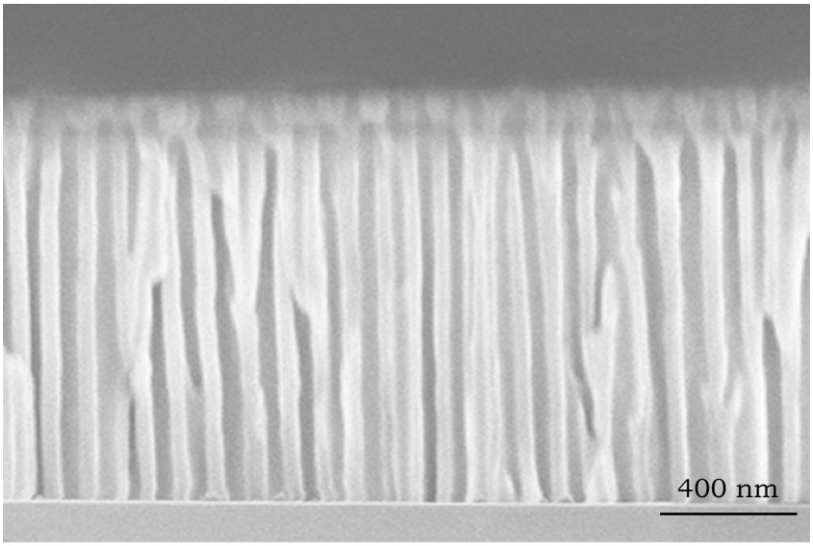

(B)

Figure 4.1. SEM Images of Thin-Film PAA Filter. (A) The bottom view of the thin-film PAA filter. The alumina pores were opened after the Si_3N_4 supporting layer was removed by CF_4 dry etch. (B) The cross section of the PAA filter, showing a thickness of 1.2 μm.

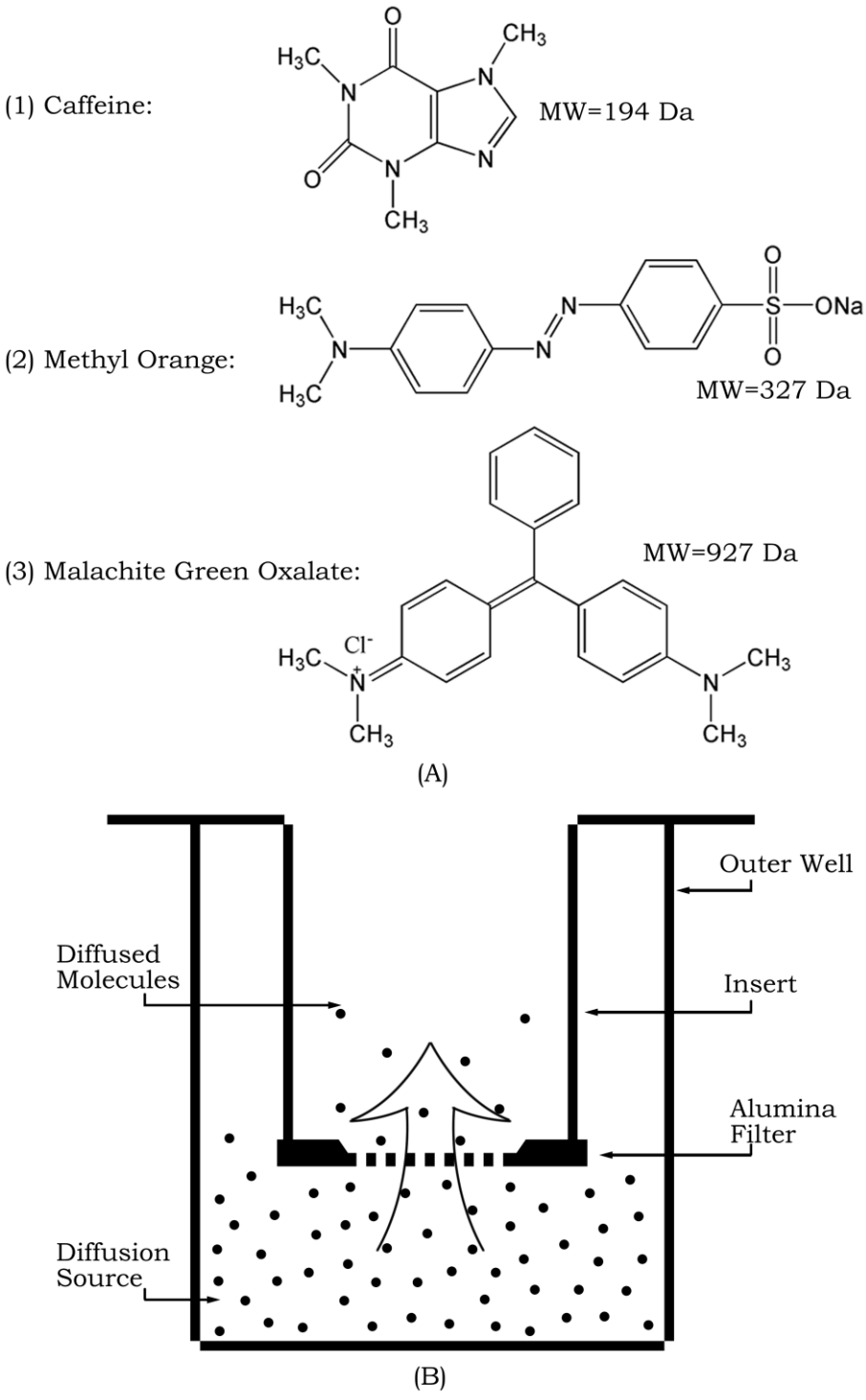

Figure 4.2. Molecular Indicators and Diffusion Device. (A) The chemical structures of the three molecular indicators used in the diffusion experiments. (B) The diffusion device based on a thin-film PAA filter.

4.3 Results and Discussion

The physical structure of the freestanding alumina membrane was verified by SEM images. Figure 4.1 (A) was taken from the backside of the membrane, around a corner of the diffusion window. It was clear from the image that the pores were opened after the CF_4 etch. Figure 4.1 (B) is the cross section of the membrane, showing vertically aligned alumina pores with straight channel profiles. The membrane thickness was 1.2 μm. The histogram in Figure 4.3 shows the distribution of the alumina pore sizes, based upon the measurements on 430 individual pores in an SEM image. The mean pore diameter was 40 nm, with a σ of 3.1 nm.

Figure 4.4 shows the time course of the normalized concentration of the diffused molecules, which was the ratio of the time-dependent absorbance in the insert (OD_i) to the time-independent absorbance in the outer well (OD_o). As the alumina pores were quite small and had a high aspect ratio, the confined molecular diffusion could be reasonably approximated as one-dimensional diffusion process obeying Fickian's Law, having the following equations:

$$\int_0^t J\varepsilon A dt = C_i V_i \tag{4.1}$$

$$J = -D\frac{C_i - C_o}{\tau T} \tag{4.2}$$

Where J is the molecular flux; D is the effective diffusion coefficient; C_o is the concentration in the outer well; C_i is the concentration in the insert at time t; τ is the channel tortuosity; T is the membrane

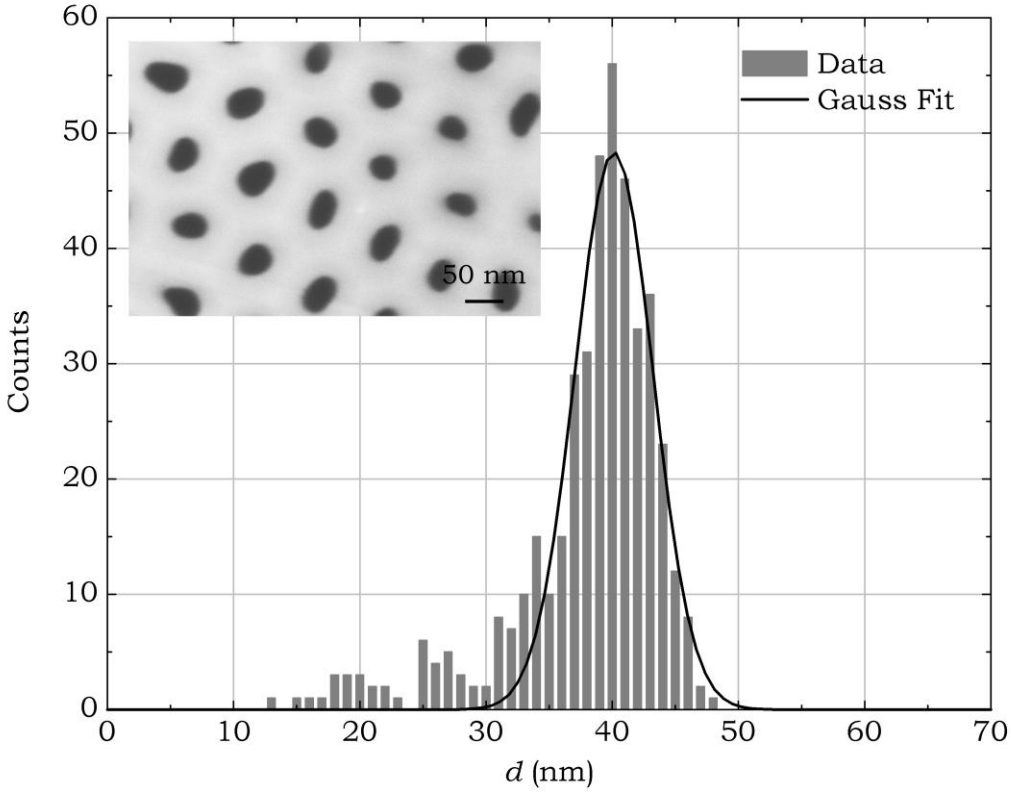

Figure 4.3. Pore Size Distribution of PAA Filter. The histogram shows the distribution of the pore diameter of the PAA filter, together with its Gauss fit (solid line). The pore diameters (d) were calculated from an SEM image (partly seen as the inset) using Equation 2.3, having a mean value of 40 nm, with a standard deviation of 3.1 nm.

thickness; ε is the membrane porosity; A is the diffusion window area; V_i is the water volume in the insert. Substituting J in equation (2) with equation (1) and solving the integral yields:

$$C_i = C_o\left(1 - e^{-\frac{\varepsilon DA}{\tau TV_i}t}\right) \tag{4.3}$$

or

$$\frac{C_i}{C_o} = \frac{OD_i}{OD_o} = 1 - e^{-\frac{\varepsilon DA}{\tau TV_i}t} \tag{4.4}$$

For our diffusion device, the diffusion window area A was 8.1×10^{-3} cm^2; ε was 14.2%, calculated from the SEM images by Matlab; the tortuosity τ was set to 1 for simplicity; T was 1200 nm; V_i was 150 µl. With the terms above, the diffusion coefficient D was calculated by fitting equation (4.4) to data in Figure 4.4. The calculation results are summarized in Table 4.1.

For our diffusion device, the water surface inside the insert was 2 mm lower than the surface in the outer well. During the diffusion process this height difference was compensated by placing an O-ring of appropriate size between the insert and the outer well. When measuring the absorbance, 100 µl of solution was taken out the insert, introducing a water pressure difference of 2 mm. The corresponding pressure-driven water flow was calculated to be 9.6×10^{-5} µl s^{-1} based on the Poiseuille equation for cylindrical tubes:

$$Q = \frac{\pi d^4 \Delta P}{128\mu L}N \tag{4.5}$$

where d is the pore diameter; ΔP is the pressure difference; L is the pore length; μ is the dynamic viscosity of water; N is the number of

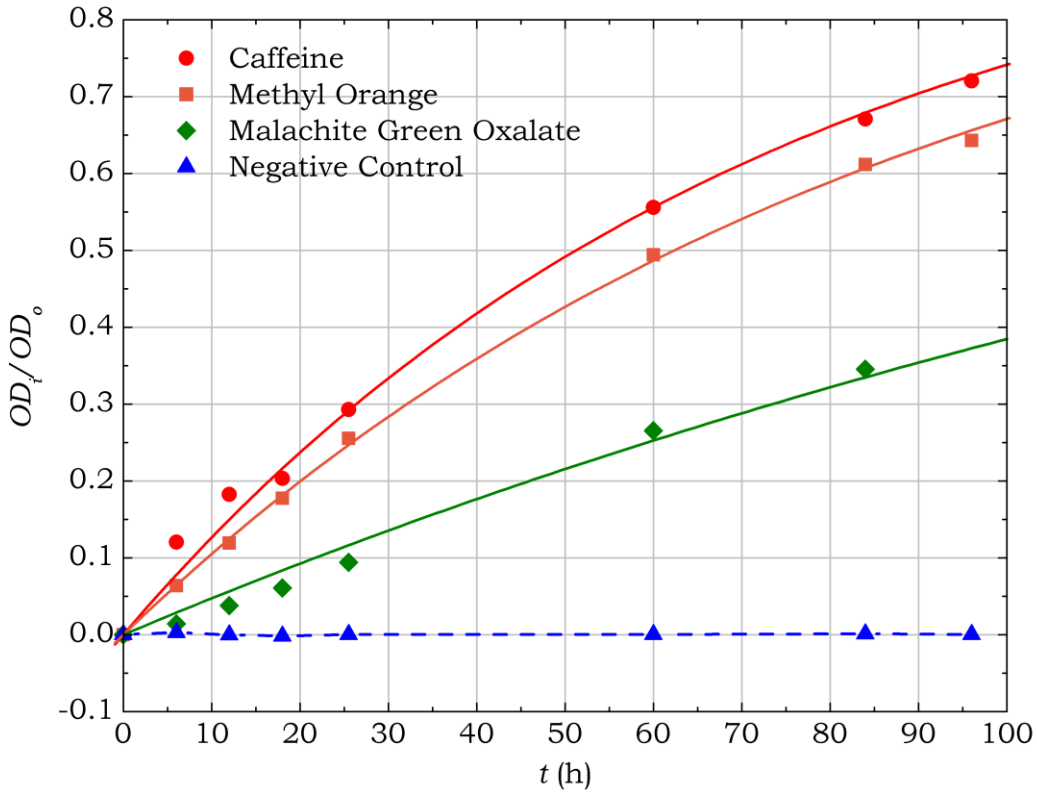

Figure 4.4. Diffusion Dynamics in PAA Pores. The plot shows the normalized absorbance (OD_i/OD_o) as a function of the diffusion time, for each molecular indicator. Solid lines are the fitted curves based on Equation 4.4. Blue points are for the negative control, with a linearly interpolated dash line.

Table 4.1. Physical Properties of Molecular Indicators

	Caffeine	Methyl Orange	Malachite Green Oxalate
Formula	$C_8H_{10}N_4O_2$	$C_{14}H_{14}N_3NaO_3S$	$[C_{23}H_{25}N_2{\cdot}C_2HO_4\ ]_2{\cdot}C_2H_2O_4$
M	194	327	927
M_e	194	304	749
λ	285	465	620
C	1.00	0.10	1.67×10^{-2}
pH	6.1	6.2	4.5
D	5.88×10^{-8}	4.83×10^{-8}	2.11×10^{-8}
J	1.76×10^{-6}	1.45×10^{-7}	1.06×10^{-8}

Footnote: M is for the molecular weight in the unit of Da; M_e is the effective molecular weight in the unit of Da. λ for the wavelength at the peak absorbance in the unit of nm, C for the concentration in the unit of mM; D for the diffusion coefficient in the unit of $cm^2\ s^{-1}$, and J for the molecular flux in the unit of mol $cm^2\ h^{-1}$.

alumina pores in one diffusion window ($N = \frac{4\varepsilon A}{\pi d^2} = 9.2\times10^7$). As each absorbance measurement took ~2 min, the pressure-driven water flow during each reading was ~0.01 μl, which was negligible compared to the base volumes in the insert and the outer well. Therefore the molecular transportation in our experiment could be safely regarded as a diffusion-only process.

The stocks of caffeine, MO, and MGO were prepared in dH_2O with no salts and diluted to the desired concentrations before every experiment, having a final pH value of 6.1, 6.2, and 4.5, respectively. Caffeine was neutral in charge. MO had a pKa~4, so it was negatively charged at pH=6.2 and had an effective molecular weight of 304 Da due to the dissociation of Na^+. With a pKa~7, MGO was assumed to be dissociated as $[(C_{23}H_{25}N_2)^+]_2{\cdot}C_2H_2O_4$ and $2C_2HO_4^-$. Therefore its main body was positively charged at pH=4.5, having an effective molecular weight of 749 Da. Calculated from the model above, the diffusion coefficient was 5.88×10^{-8} cm^2 s^{-1} for caffeine, 4.83×10^{-8} cm^2 s^{-1} for MO, and 2.11×10^{-8} cm^2 s^{-1} for MGO. In our experiments, the diffusion molecules were relatively small and could be reasonably treated as spherical particles. Therefore the molecular radius could be represented as $(M_e)^{-1/3}$, M_e for the effective molecular weight. The solid points in Figure 4.5 show the plot of the diffusion coefficient as a function of $(M_e)^{-1/3}$. As the isoelectric point of unmodified alumina surfaces was at pH~8,[177] the membranes in our experiments were all positively charged. The excessive charge on the alumina surface could significantly affect the transportation of the charged species MO and MGO since the pore diameter was only 40 nm. To investigate this

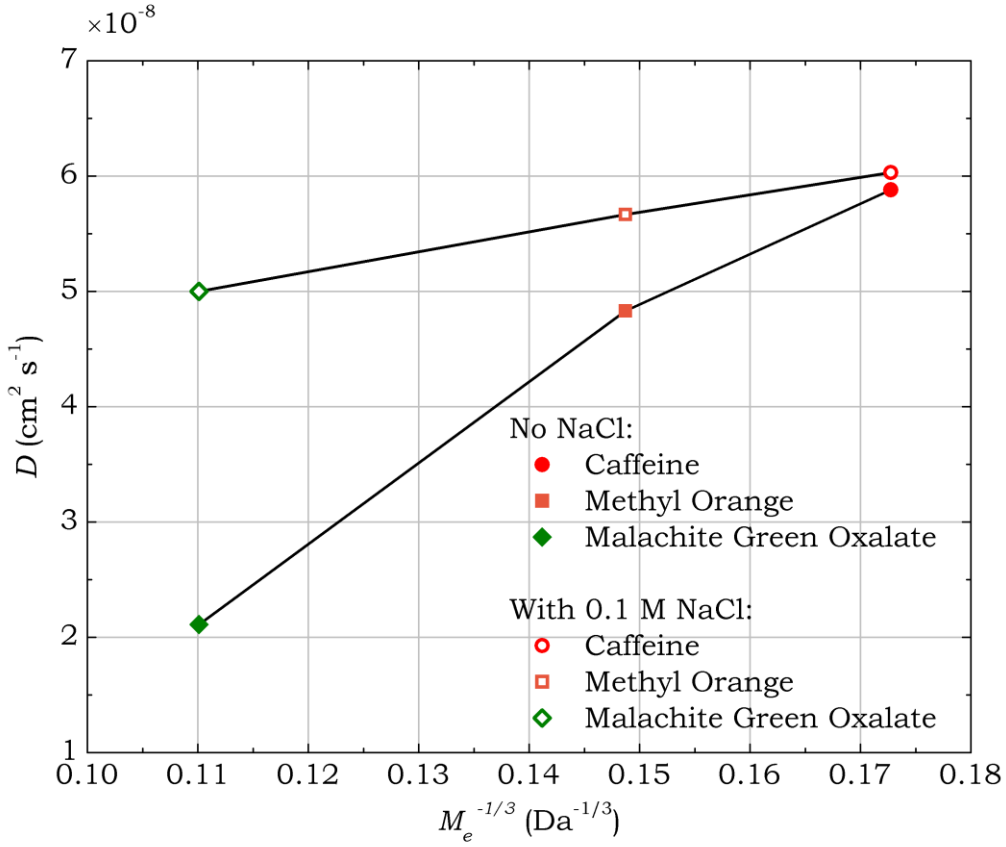

Figure 4.5. Charge Effects on Confined Diffusivity. The plot shows the diffusion coefficient D as a function of $(M_e)^{-1/3}$, with (open) and without (solid) the presence of 0.1 M NaCl in the diffusion solution, M_e for the effective molecular weight. The solid lines are the linear interpolations.

electrostatic effect, NaCl was added in the three samples with a final concentration of 0.1 M. The corresponding diffusion coefficients were plotted as the open points in Figure 4.5. The diffusivity of MGO was significantly enhanced by a factor of 2.37, suggesting that the MGO cations without NaCl experienced a strong repelling effect[65,178,179] from the positively charged alumina surface. The addition of NaCl increased the ionic strength of the solution and minimized the electric double layer near the alumina surface. The Debye length was reduced to ~1 nm based on Gouy-Chapman equation.[180] The diffusion of the MO anions was slightly improved by a factor of 1.17 whereas the neutral caffeine was basically unaffected by the addition of NaCl. The calculated diffusion coefficients were on the order of 10^{-8} cm^2 s^{-1}. In the bulk solution, molecules of similar size typically had a diffusion coefficient of 10^{-6} cm^2 s^{-1}.[181,182] Our results were in reasonable agreement with the metal ion diffusion experiment by Bluhm et al.,[69] in which the diffusion of ions such as Sr^{2+} in 20-100 nm alumina pores was reduced by about two orders of magnitude. In the work of Vlassiouk et al.,[45] the diffusivity of $Fe(CN)_6^{3-}$ was measured to be on the order of 10^{-7} cm^2 s^{-1} when passing through the alumina pores modified with hybridized DNAs. When the pore diameter is close to the molecular size, the decrease in diffusivity can be dramatic. For instance, a reduction factor of 10^{10} was observed in the diffusion of dye molecules pyronine and oxonine in Zeolite L.[183] In the report by Hinds et al.,[184] on the other hand, the diffusion of $Ru(NH_3)^{3+}$ confined in 4.3 nm carbon nanotubes was measured to be on the order of 10^{-6} cm^2 s^{-1}, which was comparable to the diffusivity in the bulk solution.

Therefore the characterizations of molecular diffusion confined in nanopores have not been all conclusive yet and remain for future study. In another experiment, we attempted to diffuse a larger molecular marker (dyed microspheres, 20 nm in diameter, Interfacial Dynamics, Corp) through the same alumina membrane but the concentration in the insert remained zero over days (data not shown), indicating the diffusion was extremely slow or even blocked when the molecular size was comparable to the pore diameter. On the other hand, the calculated molecular flux were 1.76×10^{-6} mol cm^2 h^{-1}, 1.45×10^{-7} mol cm^2 h^{-1}, and 1.06×10^{-8} mol cm^2 h^{-1}, for 1 mM caffeine, 0.1 mM MO, and 16.7 μM MGO, respectively. The thin-film alumina was favorable for achieving faster molecular transport as the molecular flux is significantly higher than that on the conventional membranes [29]. The integration of the alumina film with the silicon chip provided the possibility of adding microelectronic circuits for signal digitalization. With all these features, the on-chip diffusion system using the thin-film alumina membrane will be interesting to many fields, for example, “Lab-on-a-chip”, which emphasizes time efficiency, operation performance, and device miniaturization. The characterizations reported here have provided a baseline for the analysis of the diffusion dynamics in alumina pores, and will serve as a useful reference for applications that involve molecular transports in nanoporous structures, such as drug deliveries, cell cultures, and membrane biosensors.

4.4 Conclusion

A micrometer-thick freestanding PAA film has been fabricated on a silicon substrate and utilized as a thin-film filter in the investigation of the molecular diffusion in nanopores. Sub-1000-Da molecules, caffeine, methyl orange, and malachite green oxalate, were diffused through a 1.2-μm-thick PAA film with a pore size of 40 nm. The diffusion dynamics was modeled as one-dimensional Fickian flow. Due to the well-defined physical structure of the PAA film, the characteristic parameter of the diffusion process, diffusion coefficient was calculated from the model. The diffusion rate differed by the molecular weight. The confined diffusivities were characterized to be on the scale of 10^{-8} cm^2 s^{-1}, about two orders of magnitude lower the diffusivities in the bulk solution. It was found that the presence of ions in the diffusion solution significantly enhanced the diffusion rate of the charged molecules, by minimizing the thickness of the electric double layer at the vicinity of the pore walls. The molecular flux obtained on the PAA thin film was relatively high due to the ultra small thickness of the PAA film. The diffusion system built on the PAA thin film, as well as the dynamics characterizations, will be valuable for future applications that involve any molecular transports in alumina nanopores, such as separations, drug delivery, and on-chip cell culture.

CHAPTER 5

DNA BIOSENSOR BY METAL-ALUMINA-METAL STRUCTURE

5.1 Background

Deoxyribonucleic acid (DNA) is a subject of great research interest. Base on the Watson-Crick structure model,[185] ssDNA nucleotides hybridize through hydrogen bonds between complimentary base pairs, forming double-stranded DNA (dsDNA) helix. To nanotechnology, this natural and precise self assembly presents DNA as a biological example of constructing high-level function systems from primary building blocks in a "bottom-up" approach. In the future, biomolecular electronic devices could be possibly built on the DNA structure or based on its self-assembly mechanism. Because DNA nucleotides carry the essential genetic information that regulates the development and functioning of living organisms, understanding and controlling the genes encoded in DNA sequences is crucial to life science. Numerous DNA biosensors have been developed to sense DNA behaviors such as hybridization and sequence mutation. Nanotechnology provides a powerful system for studying and manipulating DNA at the nanoscale. Many nanomaterials and nanostructures have been used in the development of DNA biosensors. In recent years, several works have been reported using PAA as the core material in the DNA sensor devices. In this chapter, major works of PAA-based DNA biosensors are introduced, followed by the report of a new DNA biosensor based on a thin-film PAA capacitor structure.

Several biosensors using electrical detections have been reported. Steinle et al.[44] reported that alumina pores could serve as ion channels with a switchable gate controlled by the surface

hydrophilicity. After the alumina membranes (200 nm in pore diameter; 60 μm in thickness) were modified with a hydrophobic C_{18} silane layer, the alumina pore walls became highly hydrophobic. The pores were in an "off" state, preventing water and ions ($Ru(bpy)_3^{2+}$) passing through the pores. The state was turned to "on" by adding hydrophobic ions (dodecylbenzene sulfonate (DBS)) in the ionic solution to a sufficiently high concentration. XPS studies proved that the added DBS were presented on the C_{18}-modifed surface. At low DBS concentrations ($<10^{-6}$ M), the membrane resistance was in the range of 10^7 Ω, but rapidly decreased to the scale of 10^3 Ω when the DBS concentration was above 10^{-6} M. Vlassiouk et al.[45] monitored the DNA hybridization on the alumina sidewalls by measuring the ionic conductance through alumina pores, using cyclic voltammetry (CV), DC time course, and impedance microscopy. The alumina pores (20 nm or 200 nm in diameter; 60 μm in length) were chemically modified with 21-mer ssDNAs. Complementary DNA nucleotides flowed through the alumina pores to hybridize with the anchored DNA probes. The CV measurements showed that both oxidative and reductive currents decreased after the hybridization in the 20-nm pores, whereas no noticeable changes observed in 200-nm pores because of the larger current paths. In the dc current measurements, these 20-nm pores with the hybridization lowered the charge diffusion rate by a factor of ~2, compared to the pores modified with ssDNAs only. Similarly, an impedance increase was also observed in both 20-nm and 200-nm pores coated with hybridized DNAs. Based on a sensor dimension of $5\times5\times0.5$ μm^3, a theoretical limit of detection was estimated to be 10^{-17}

mol of complementary DNA, for immobilized ssDNA molecules with an area density of 10^{12} cm^{-2}. Takmokov et al.[46] shrunk the alumina pore size by the hydrothermal treatment to less than 10 nm in diameter and 2-4 μm in length. The measurements showed that the impedance increased by more than 50% when the hybridization occurred on the alumina sidewalls.

Several other PAA-based DNA biosensors sensed the hybridization using optical methods. In the work by Vlassiouk et al.,[31] the alumina pore walls were coated with 21-mer or 41-mer ssDNAs through the crosslinking system using amino-silane and glutaraldehyde. The hybridizations with complementary DNAs were directly detected by measuring UV and IR absorption spectra. The absorbances in these optical regions increased after the hybridization process. The surface density of the bound DNA molecules was on the order of 10^{12} cm^{-2}, and the hybridization efficiency was ~70%. In the method by Matsumoto et al.,[42] ssDNA molecules were labeled with fluorescent Cy2 or Cy3 dyes, and the hybridization was detected by fluorescence microscopy. DNA molecules fixed in the alumina pores with an inter-pore distance larger than 400 nm were able to be resolved as individual bright spots under fluorescence microscope, showing a pattern similar to the alumina's hexagonal array. A similar detection approach using fluorescent dyes was reported by Cloutier et al.,[43] who utilized the intercalation of fluorescent TOTO-1 dyes with DNA molecules.

In this chapter, a new DNA biosensor has been developed based on a thin-film PAA capacitor. A metal-aluminum-metal (MAM) structure

was constructed by partially anodizing an aluminum thin film, followed by depositing another aluminum layer on the top. The residual aluminum layer during the anodization process served as a bottom electrode whereas the second aluminum layer deposited on the top served as a top electrode. The sidewalls of the PAA film were chemically modified with ssDNA oligonucleotides. Complementary DNA oligonucleotides were loaded into the alumina pores to hybridize with the ssDNA probes on the sidewalls. The impedance spectra of the DNA-coated PAA film were measured in the solid state. The impedance characteristics before and after the DNA hybridization were analyzed by modeling the equivalent circuit of the MAM structure. It was found that the DNA hybridization occurred on the sidewalls introduced a dc resistance reduction along the sidewall surface, probably because the DNA immobilization facilitated the electron transport along the pore wall surface between the two electrodes. In addition, the impedance characteristics of the barrier-type oxide, which was modeled as a constant-phase element, were found to be sensitive to the DNA attachment, possibly due to the redistribution of the excessive mobile ions inside the barrier-type oxide.

The biosensor device reported here showed an exploration of utilizing PAA thin films for on-chip biosensing applications. The MAM structure served as a structure model of nanogap electrode pairs with large surface of the interior dielectric layer. The impedance characteristics of the alumina film, especially the barrier-type oxide showed to be sensitive to the molecular coatings on the surface. It will possibly be generally useful in the future biosensor designs.

5.2 Methods

5.2.1 Fabrication of MAM Structure

Glass wafers were used as the substrate of the DNA biosensor. The MAM structure was fabricated by four layers of aluminum depositions, together with a time-controlled aluminum anodization. Figure 5.1 and 5.2 show the schematic of the device fabrication in the cross-sectional view and the top view, respectively. The first aluminum layer was 100 nm thick, serving as the bottom electrode in the MAM structure. The second aluminum layer was 200 nm thick, use for producing the PAA film in the MAM structure. The anodization was controlled in time such that it only anodized the second aluminum layer, without affecting the bottom 100-nm-thick aluminum. The third aluminum layer was 20 nm thick, deposited on the PAA film as the top electrode. The last aluminum layer was 250 nm thick, serving as the contact areas.

(1) Layer 1: Bottom Electrode

4-inch double-side-polished soda-lime glass wafers (Silicon Quest, Inc) were spun at 4000 rpm and cleaned with acetone and ethanol for 30 sec. LOR-5A (MicroChem, Corp) was spun on the wafers at 4000 rpm for 30 sec and baked at 180 °C for 5 min. Photoresist SPR955-CM 0.9 (MEGAPOSIT™) was spun on the LOR-5A at 4000 rpm for 30 sec and baked at 90 °C for 1 min. The photoresist was patterned under the contact exposure mode, with an exposure dosage of 14 sec at 12 mW cm^{-2}. The wafers were developed in the developer 300 MIF (AZ Electronic Materials, Corp) for 65 sec. After rinsing with dH_2O and

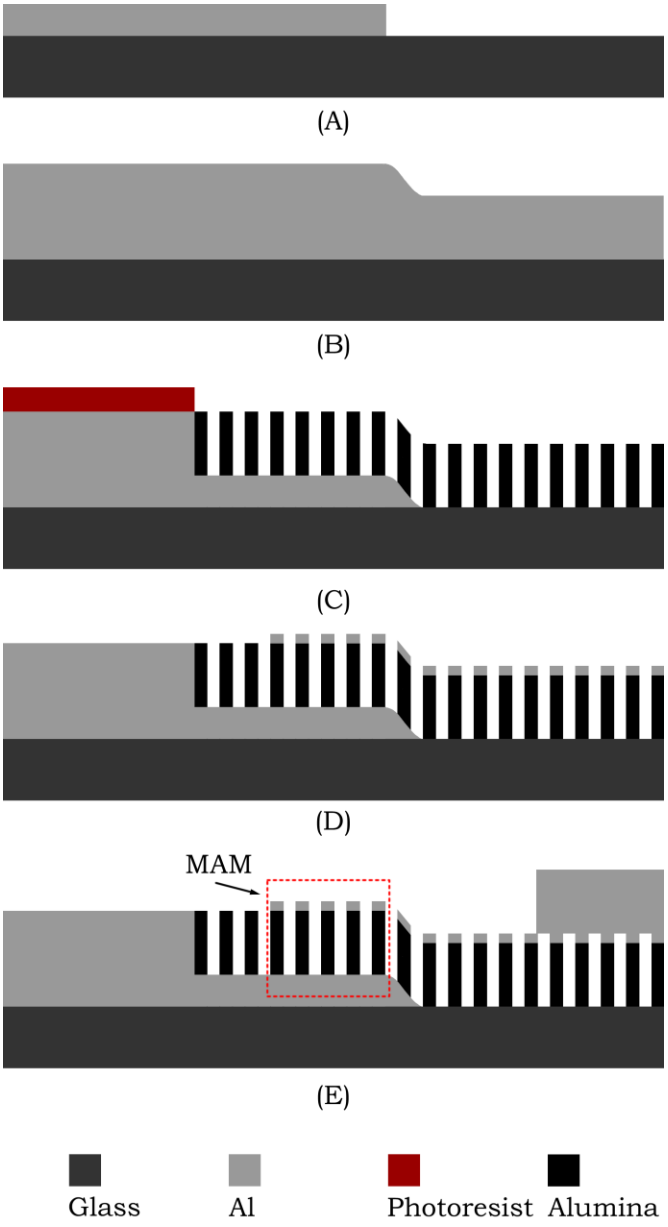

Figure 5.1. Fabrication of MAM DNA Biosensor (1). (A) A deposition of 100-nm-thick Al for the bottom electrode. (B) A conformal deposition of 200-nm-thick Al. (C) A time-controlled anodization, patterned with photoresist. (D) A deposition of 20-nm-thick Al for the top electrode. (E) A deposition of 200-nm-thick Al for the contact areas.

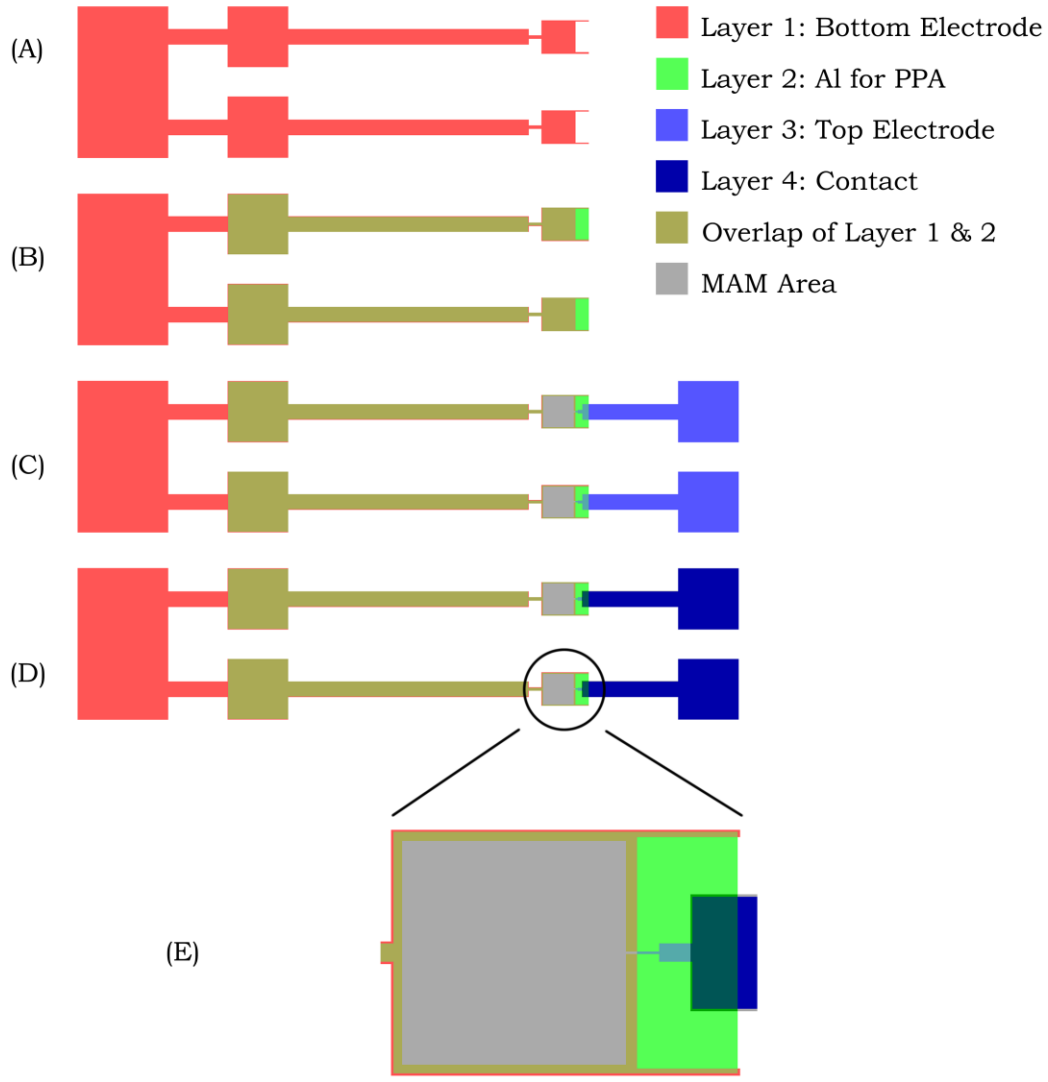

Figure 5.2. Fabrication of MAM DNA Biosensor (2). (A) A deposition of 100-nm-thick Al for the bottom electrode. (B) A conformal deposition of 200-nm-thick Al for producing the PAA film. (C) A deposition of 20-nm-thick Al for the top electrode. (D) A deposition of 200-nm-thick Al for the contact area. (E) A zoom-in view of the MAM structure as circled in (D).

drying under N_2 gas flow, the wafers were descumed by oxygen plasma cleaning at 80 °C for 1 min to remove the residual photoresist. High-purity (99.999%) aluminum (Research and PVD Material, Corp) was evaporated on the photoresist-coated wafers at 1.5 Å sec^{-1} for 100 nm. The aluminum deposited on the photoresist was lifted off by soaking in the photoresist stripper 1165 (Rohm and Haas Electronic Materials, LLC) overnight, followed by rinsing with dH_2O and drying under N_2 gas flow.

(2) Layer 2: Aluminum for PAA

After the process of layer 1, LOR-5A was spun on the wafers at 4000 rpm for 30 sec and baked at 180 °C for 5 min. Photoresist SPR955-CM 0.9 was spun on the LOR-5A at 4000 rpm for 30 sec and baked at 90 °C for 1 min. The photoresist was patterned under the contact exposure mode, with an exposure dosage of 14 sec at 12 mW cm^{-2}. Wafers were developed in 300 MIF for 65 sec. After rinsing with dH_2O and drying under N_2 gas flow, the wafers were descumed by oxygen plasma cleaning at 80 °C for 1 min to remove the residual photoresist. High-purity (99.999%) aluminum was evaporated on the photoresist-coated wafers at 4 Å sec^{-1} for 200 nm. The aluminum deposited on the photoresist was lifted off by soaking in the photoresist stripper 1165 overnight, followed by rinsing with dH_2O and drying under N_2 gas flow.

(3) Aluminum Anodization

The aluminum anodization was performed in 0.3 M oxalic acid at room temperature, with an anodizing voltage of 40 V. The anodizing time was controlled such that the process stopped after the 200-nm-

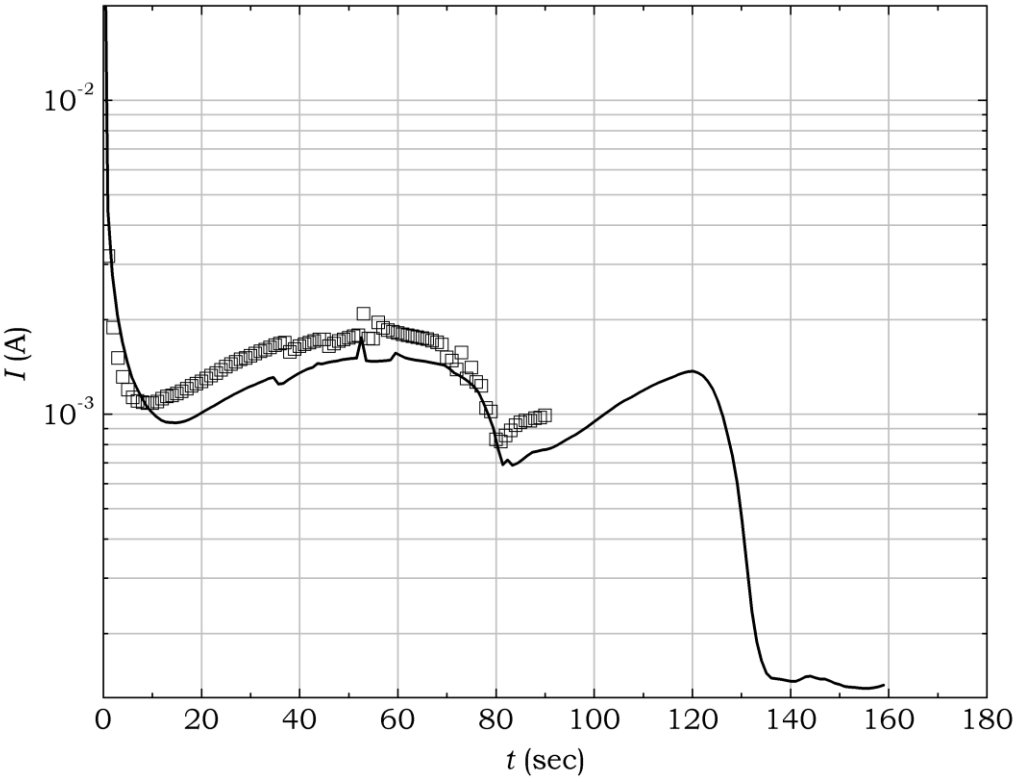

Figure 5.3. I-t Curve of Time-Controlled Anodization. The solid curve is a complete anodization of the 300-nm-thick aluminum layer (Figure 5.1 (B) or Figure 5.2 (B)). The curve with squares is a time-controlled anodization, which was stopped when 200 nm of aluminum was anodized.

thick aluminum layer was completely anodized, leaving the 100-nm-thick aluminum layer as the bottom electrode. The recorded current-time profiles are shown as Figure 5.3. Based on the plot, the anodization of the 200-nm-thick aluminum layer completed around 85 sec. The anodizing time was set to be 90 sec to ensure that the 200-nm-thick layer was fully anodized. The slight over etch (5 sec) did not affect the 100-nm-thick layer significantly as it was in the pore initiation stage of the second aluminum layer. After the anodization, the wafers were rinsed with dH_2O and dried under N_2 gas flow.

(4) Layer 3: Top Electrode

After the aluminum anodization, LOR-5A was spun on the wafers at 4000 rpm for 30 sec and baked at 180 °C for 5 min. Photoresist SPR955-CM 0.9 was spun on the LOR-5A at 4000 rpm for 30 sec and baked at 90 °C for 1 min. The photoresist was patterned under the contact exposure mode, with an exposure dosage of 14 sec at 12 mW cm^{-2}. Wafers were developed in the developer 300 MIF for 65 sec. After rinsing with dH_2O and drying under N_2 gas flow, the wafers were descumed by oxygen plasma cleaning at 80 °C for 1 min to remove the residual photoresist. High-purity (99.999%) aluminum was evaporated on the photoresist-coated wafers at 1 Å sec^{-1} for 20 nm. The aluminum deposited on the photoresist was lifted off by soaking in 1165 overnight, followed by rinsing with dH_2O and drying under N_2 gas flow.

(5) Layer 4: Contact Area

After the top electrode was patterned, LOR-5A was spun on the wafers at 4000 rpm for 30 sec and baked at 180 °C for 5 min. Photoresist SPR955-CM 0.9 was spun on the LOR-5A at 4000 rpm for

30 sec and baked at 90 °C for 1 min. The photoresist was patterned with under the contact exposure mode, with an exposure dosage of 14 sec at 12 mW cm^{-2}. Wafers were developed in 300 MIF for 65 sec. After rinsing with dH_2O and drying under N_2 gas flow, the wafers were descumed by oxygen plasma cleaning at 80 °C for 1 min to remove the residual photoresist. High-purity (99.999%) aluminum was evaporated on the photoresist-coated wafers at 5 Å sec^{-1} for 250 nm. The aluminum deposited on the photoresist was lifted off by soaking in 1165 overnight, followed by rinsing with dH_2O and drying under N_2 gas flow.

5.2.2 PAA Surface Modification

The oxide nature of the PAA film was utilized to achieve the surface functionalization. The hydroxyl bonds (-OH) on the alumina surface could first be activated by amino-silane to introduce an amino group on the surface. The amino group ($-NH_2$) was further linked with glutaraldehyde, turning the active end from the amino group to a carbonyl group (-C=O). ssDNA oligonucleotides were then immobilized on the alumina sidewalls by the dehydration between the amino group and the carbonyl group. Through these three steps of chemical modifications, the ssDNA molecules were attached on the alumina surface through covalent bindings, serving as anchored probes for capturing the ssDNA targets that had a complementary sequence. The immobilization of the ssDNA probes is illustrated in Figure 5.4.

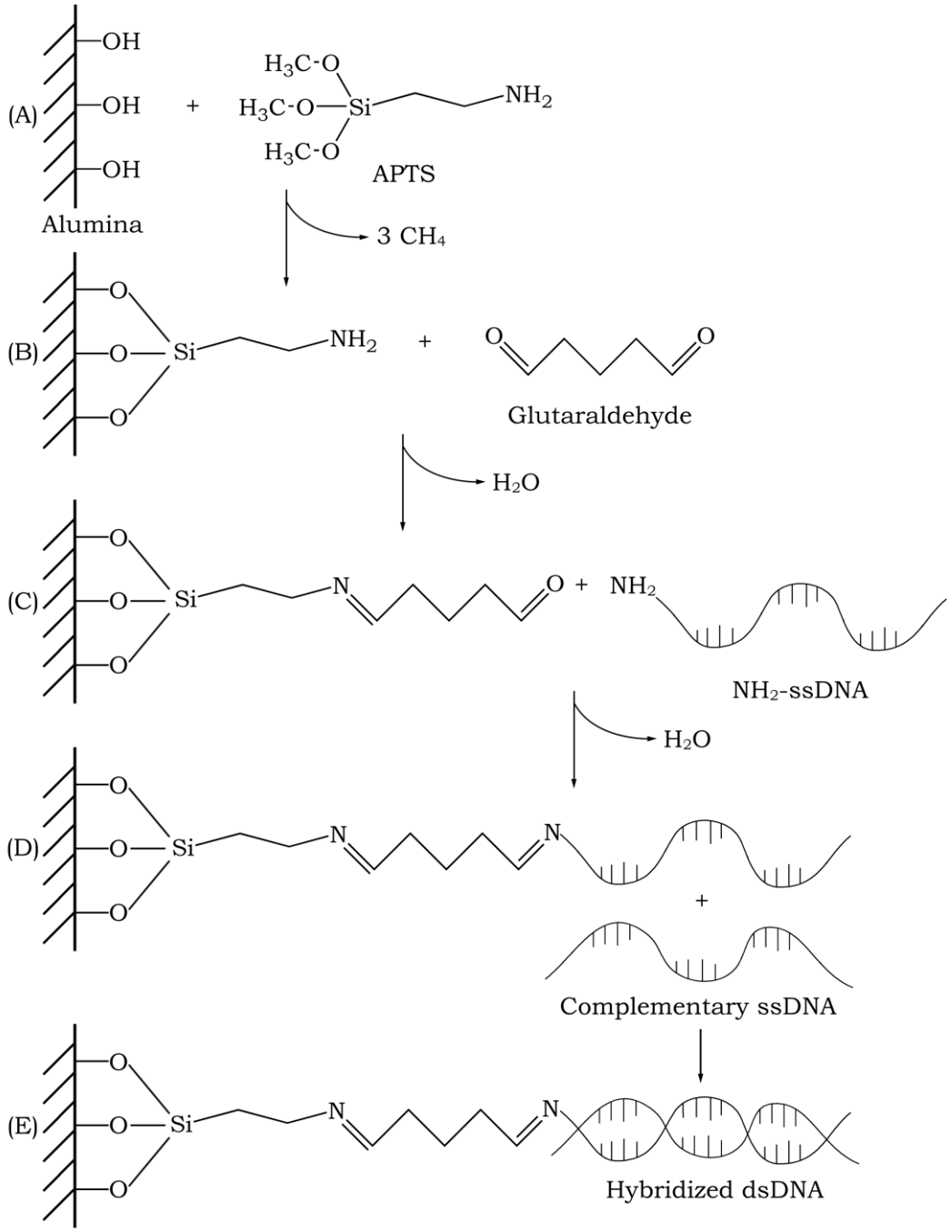

Figure 5.4. Surface Chemistry on MAM Structure. (A) The alumina surface silanization by APTS. (B) The attachment of glutaraldehyde to APTS. (C) The immobilization of the amino-ssDNAs to glutaraldehyde. (D) The hybridization of the ssDNA targets with the anchored ssDNA probes. (E) The hybridized DNA on the alumina pore walls.

(1) Surface Silanization

The MAM devices were cleaned with dH_2O thoroughly and dried under N_2 gas flow. To remove residual organic contaminants, the devices were under plasma oxygen cleaning for 5 min. The surface of the alumina sidewalls were silanized by soaking the devices in 5% (3-aminopropyl)trimethoxysilane (APTS) (Sigma-Aldrich, Co) in acetone and leaving at room temperature for 1 h with encapsulation. The devices were then rinsed with acetone and baked at 120 °C for 30 min.

(2) Glutaraldehyde Attachment

After the baking, the APTS-silanized MAM devices were soaked in 25% aqueous glutaraldehyde solution (Sigma-Aldrich, Co) at room temperature for 1 h with encapsulation, followed by rinsing with dH_2O thoroughly and drying under N_2 gas flow.

(3) ssDNA Immobilization

20-mer ssDNA oligonucleotides with the following sequence were used as the sensing probes: 5'-amino-ATG GGT GCG AGA GCG TCA GT-3'. The oligonucleotides were modified with an amino group at their 5' ends, which could react with a carboxyl group to form an amide structure. Complementary DNA oligonucleotides (5'-ACT GAC GCT CTC GCA CCC AT-3') were used as the target molecules for the detection of the hybridization process. The DNA oligonucleotides were purchased from Integrated DNA Technologies, Inc, purified with standard desalting. The samples were stored at -20 °C before use.

After the MAM devices were treated with glutaraldehyde, 5 μl of the amino-ssDNA (1 mM in dH_2O) was applied on each MAM capacitor. The devices were encapsulated and left at room temperature overnight

(~12 h). The devices were then rinsed with dH_2O and dried under N_2 gas flow.

(4) DNA Hybridization

After the MAM devices were functionalized with the ssDNA probes, 5 µl of 1 µM complementary ssDNA prepared in TE buffer (TEKnova, Inc) containing 1 M NaCl was applied on each MAM device and incubated with encapsulation at room temperature for 1 h. The devices were then rinsed with dH_2O and dried under N_2 gas flow.

(5) Negative Controls

In order to justify the signal change was introduced from the DNA molecules, instead of from the buffer environment, two sets of negative control experiments were performed as follows:

(A): An identical MAM capacitor underwent the amino-silane and glutaraldehyde treatments as described in step (1) and (2). Afterwards, 5 µl of dH_2O was applied on the capacitor and left at room temperature for 1 h with encapsulation. The samples were then rinsed with dH_2O and dried under N_2 gas flow. This severed as a negative control for the immobilization of ssDNAs on the alumina pore walls, as described in step (3).

(B): An identical MAM capacitor underwent the silanization, glutaraldehyde crosslinking, and ssDNA immobilization as described in step (1), (2), and (3). 5 µl of TE buffer containing 1 M NaCl was applied on the capacitor and left at room temperature for 1 h with encapsulation. The samples were then rinsed with dH_2O and dried under N_2 gas flow. This served as a negative control for the DNA hybridization process, as described in step (4).

5.2.3 Impedance Spectroscopy

The DNA hybridization on the alumina pore walls was sensed by impedance spectroscopy. More specifically, the hybridization was detected by monitoring the changes of the impedance spectrum of the MAM structure before and after the hybridization process. The impedance measurements were performed under the two-electrode mode. The working electrode and the counter electrode were connected to the top and the bottom aluminum layers, respectively. The measurement was performed in the solid phase, meaning no buffer solution was applied between the two electrodes.

The instrument used for the impedance measurements was FAS2 Femtostat from Gamry, Inc. The measurements were operated by the Gamry software "Framework" version.4.35. The impedance data and the equivalent circuit model were analyzed using the Gamry software "Echem Analyst" Version.1.35

The sweeping frequency range was set from 0.1 Hz to 300 kHz. The applied ac voltage was 10 mV. The dc bias was set to 0 V relative to the open circuit potential. The initial delay for the system stabilization was set to be 100 sec. Impedance data were collected 10 points per decade of the frequency. The measurements were performed at room temperature with minimized vibration noise.

The MAM structure underwent the APTS silanization, glutaraldehyde coating, and ssDNA immobilization, and finally captured the complimentary DNA targets. The impedance spectrum was measured after each of these steps, starting from an unmodified MAM structure.

5.3 Results and Discussion

The sensor device reported here was based on a metal-alumina-metal structure in the vertical direction. In this MAM structure, fabricating a bottom electrode underneath the PAA film was a challenge. Other metal materials such as Au and Pt were tried for the bottom electrode. However, these metal films were attacked by the electrolyte after the aluminum layer was anodized, causing the PAA film to peel off the substrate. To solve this problem, a time-controlled anodization was adopted to anodize a 300-nm-thick aluminum film such that the process paused when 200 nm of aluminum was oxidized to PAA, leaving the rest 100 nm of aluminum as the bottom electrode. Another 20-nm-thick aluminum film was deposited on the PAA as the top electrode. In this vertical MAM structure, direct probing on the top electrode would potentially cause a short circuit by penetrating through the PAA layer. Therefore it was important to extend the top electrode out of the MAM capacitor area for the contact purpose. For this reason, the 300-nm-thick aluminum layer was made by two steps of patterned depositions. In the first step, a 100-nm-thick aluminum film was deposited on the substrate (red in Figure 5.2), defining the bottom electrode and its contact area. In the second step, a 200-nm-thick aluminum film was patterned on the previous layer. The aluminum in the yellow region in Figure 5.2 had a total thickness of 300 nm. In the green region in Figure 5.2, the 200-nm-thick film was directly deposited on the glass substrate. A time-controlled anodization was performed on the deposited aluminum films such that the green

region was completely anodized whereas in the yellow region an aluminum layer of 100 nm thick was left as the bottom electrode. This partial anodization was verified by the current-time profile recorded during the process (Figure 5.3). The solid curve was obtained from a complete anodization. It clearly showed two distinct anodization stages, one was from 0 sec to 85 sec and the other from 85 sec to 135 sec, corresponding to the anodizations of the 200-nm-thick and the 100-nm-thick aluminum films, respectively. The valley around 85 sec indicated the completion of the first layer and the pore initialization on the second layer. The curve with squares showed the current profile of the time-controlled anodization. The process was stopped at 90 sec to ensure that the second aluminum layer was completely anodized.

Since the deposition of the 200-nm-thick aluminum film was conformal, the deposited film was continuous around the step area (Figure 5.1 (B)). This surface continuity was utilized to extend the top electrode to the contact area (Figure 5.1 (E)) without disruptions. The thickness of the top electrode was chosen to be 20 nm such that it was adequate to be a continuous conduction film but still insufficient to clog the alumina pores or connect the two electrodes.

The MAM structure was verified by the optical images in Figure 5.5 and the SEM images in Figure 5.6. Figure 5.5 (B) and (C) were the optical images taken under the differential-interference-contrast (DIC) mode and the dark-field mode, respectively, in which the top and bottom electrodes were clearly verified. The top view and the cross-sectional view of the MAM structure are shown as the SEM images in Figure 5.6.

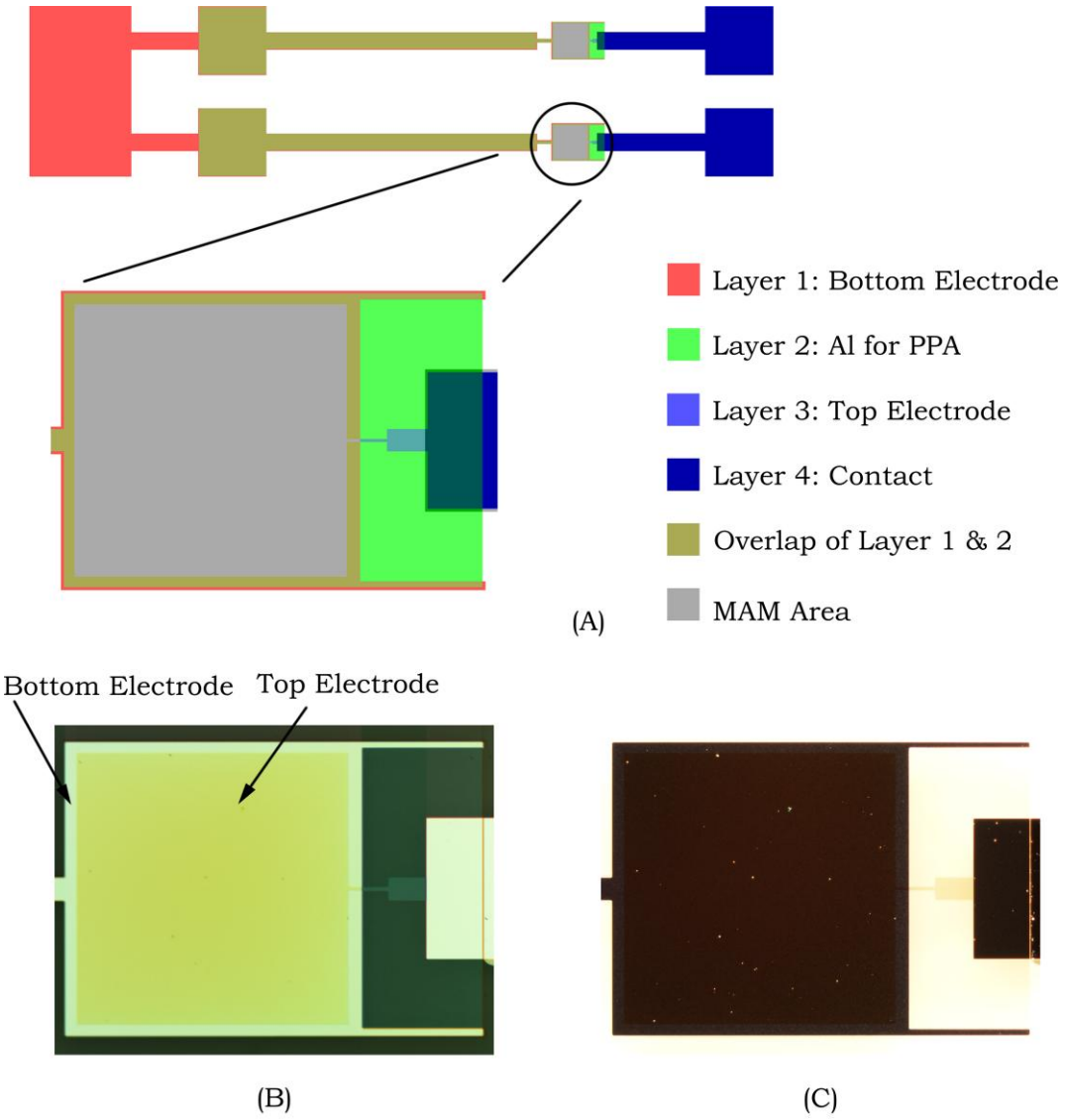

Figure 5.5. Optical Images of MAM Structure. (A) The CAD of the DNA biosensor with an MAM core structure. (B) The optical image of the MAM structure taken under the DIC mode, showing the top and to bottom electrodes. (C) The optical image of the MAM structure taken under the dark-field mode.

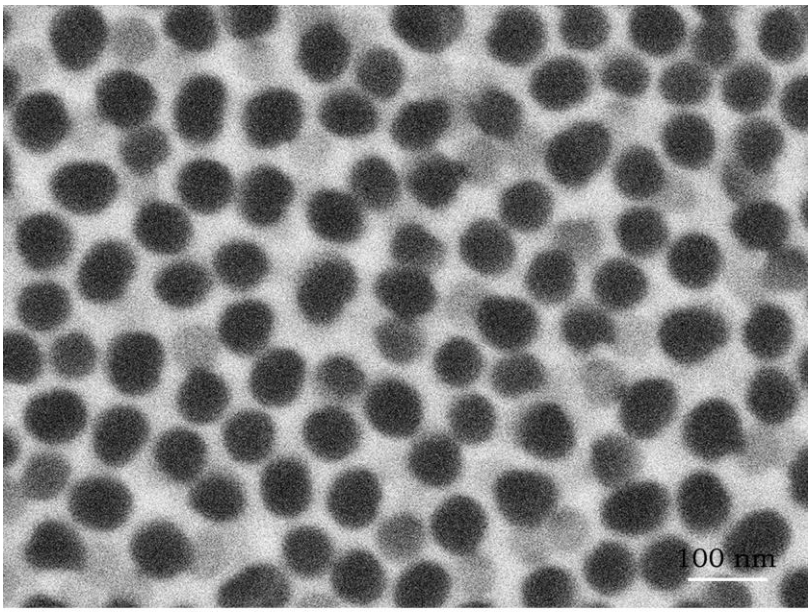

(A)

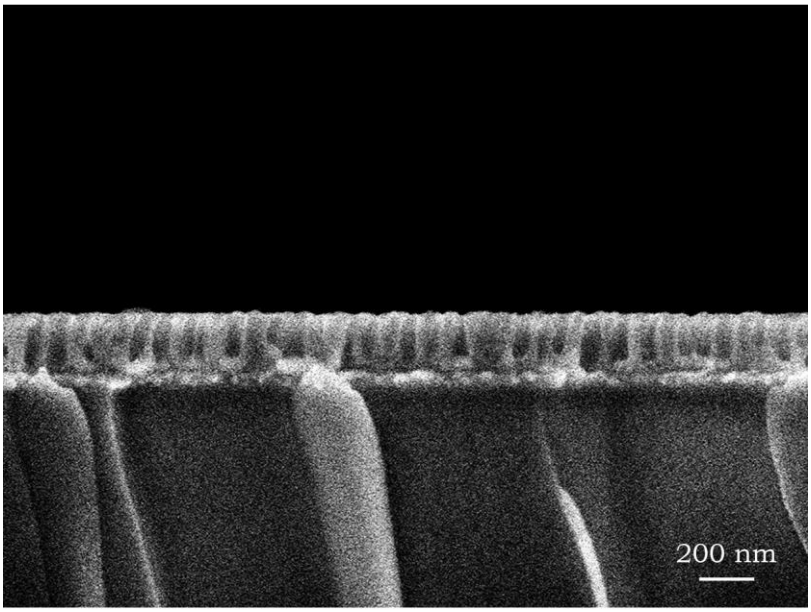

(B)

Figure 5.6. SEM Images of MAM Structure. (A) The top view of the PAA film. The average pore diameter and the overall porosity were measured to be 67 nm and 58.8%, respectively. (B) The cross section of the MAM structure. The total thickness of the PAA film, plus the top electrode, was ~220 nm. The bottom electrode was clearly seen underneath the PAA film.

In the final MAM structure, the effective capacitor area (A) was 1×1 mm^2. Based on Figure 5.6, the thickness of the alumina film, including the top electrode, was ~220 nm. The average pore diameter (d) and the overall porosity (p) were 67 nm and 58.8%, respectively, calculated from the SEM image using Matlab.

The total number of the alumina pores (N_{pore}) was calculated to be 1.67×10^8 by the following equation:

$$N_{pore} = \frac{4Ap}{\pi d^2} \tag{5.1}$$

The area density of the alumina pores (ρ_{pore}) was calculated to be 1.67×10^{10} cm^{-2} by the following equation:

$$\rho_{pore} = \frac{N_{pore}}{A} \tag{5.2}$$

The ssDNA oligonucleotides were covalently immobilized on the PAA pore walls through three steps of chemical reactions. First, the PAA pore walls were activated with the amino-silane APTS. Prior to it, the device was under oxygen plasma cleaning for 5 min to remove the possible organic contaminants and refresh the hydroxyl (–OH) bonds on the PAA surface. APTS attached to the PAA surface through the dehydration reaction between the –OH groups on the PAA and the $–OCH_3$ groups on APTS. The devices were then were baked at 120 °C to improve the stability of the attached APTS molecules. Glutaraldehyde molecule had two carbonyl (–C=O) terminals, serving as a homobifunctional crosslinker. At one end, the –C=O group reacted with the amino ($–NH_2$) group on the APTS, forming a stable amide structure. At the other end, the –C=O group reacted with the $–NH_2$

group on the amino-ssDNA nucleotides. Thus the ssDNA oligonucleotides were immobilized on the APTS-modified PAA surface through the glutaraldehyde crosslinking. The further hybridization with complementary ssDNA targets took place in the TE buffer at room temperature.

Figure 5.7 shows the structure model of the MAM capacitor. (A) is the alumina film as anodized. It consisted of a porous-type layer and a barrier-type oxide at the bottom. During the anodization, the barrier oxide served as an active frontier where the field-assisted oxidation and dissolution take place simultaneously. Under a high electric field, cations such as Al^{3+} migrated from the Al-Al_2O_3 interface to the Al_2O_3-electrolyte interface, whereas anions such as OH^- and O^{2-} migrated in the opposite direction. These cations and anions met within the barrier oxide layer to form new alumina. If the anodization was paused in the middle of the process, the electric field across the barrier oxide disappeared instantly. Therefore it was expected that there were a significant amount of free cations and anions inside the barrier oxide. The concentration of these free ions was represented by the red color gradient in Figure 5.7 (A). After the alumina film was treated by H_3PO_4 acid, the pores were widened and the barrier oxide at the pore bottoms was etched away, showing a structure as Figure 5.7 (B). Now the sidewalls consisted of the porous-type alumina and a small portion of the barrier-type oxide at the bottom of the sidewalls. For the convenience of circuit modeling, the geometry was further simplified as Figure 5.7 (C), in which both the porous-type alumina and the barrier-type alumina were regarded as planar layers with a flat interface.

Figure 5.8 shows the equivalent circuit of the MAM device. The porous part of the alumina film was modeled as a capacitor C_p. Because the PAA film was highly insulative, the resistance coupled with C_p was regarded as infinite.

The thin barrier-type oxide at the bottom of the porous-type alumina was considered as another capacitor in series with C_p. Since this barrier-type oxide had a non-planar geometry and were embedded with ions, its capacitance was modeled as a constant phase element (CPE) ϕ_b in parallel with a resistance R_b. The impedance of the CPE, Z_{ϕ_b}, is defined as:

$$Z_{\phi_b} = \frac{1}{Q_b(2\pi f \cdot i)^n} \tag{5.3}$$

Where n is an empirical factor representing the ideality of the capacitance. The capacitor behaves ideally when $n = 1$. Non-ideal capacitors are associated with an n between 0 and 1. Q_b is the numerical value of the admittance $\left|Z_{\phi_b}\right|^{-1}$ when $2\pi f = 1$ rad s^{-1}. The unit of Q_b is S s^n

The corresponding capacitance of the CPE (C_b) can be calculated by the following equation:

$$C_b = \frac{(Q_b R_b)^{1/n}}{R_b} \tag{5.4}$$

If the ssDNA oligonucleotides were conductive, their immobilization on the PAA pore walls, could potentially facilitate the electron transport along the surface of the pore walls, from one electrode to the other. This possible “leakage” current introduced by the DNA immobilization was considered in the equivalent circuit by adding a

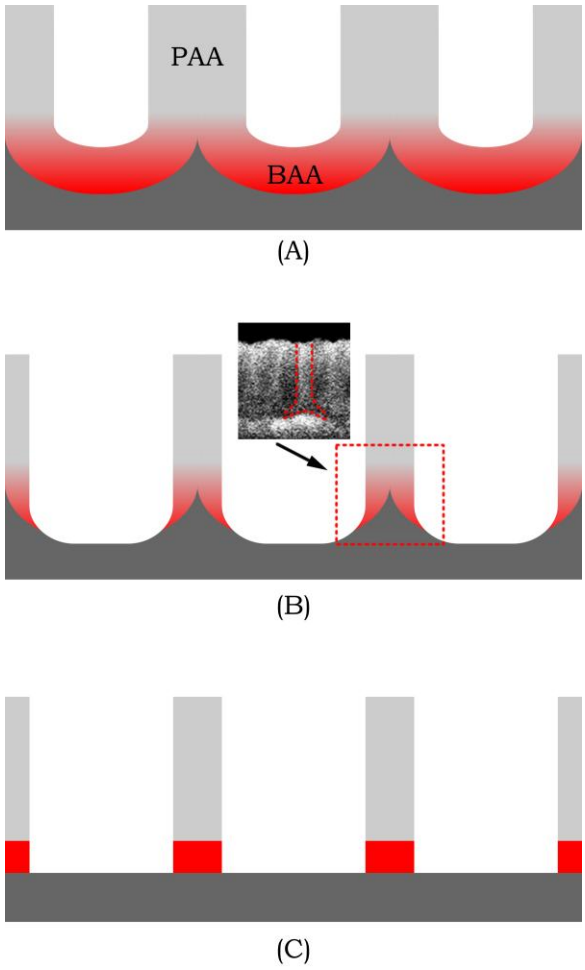

Figure 5.7. Structure Model of PAA Film in MAM. (A) The alumina film as anodized. It contained a porous-type anodic alumina (PAA) and a barrier-type anodic alumina (BAA). In the BAA, there were significant amount of mobile ions such as Al^{3+}, H^{+}, O^{2-} and OH^{-}, as discussed in Figure 1.3. In the senior PAA layer, the mobile ions were minimal as most of them formed to Al_2O_3. The ionic concentration was represented by the color gradient in red. (B) The alumina film after the pore-widening process. The sidewall structure close to the pore bottom was verified by the inserted SEM image. (C) A structure model simplified from (B). It contained two flat layers, one being an ion-free porous-type alumina film and the other being ion-rich barrier-type alumina layer underneath. The barrier layer at the pore bottoms was etched in the pore-widening process.

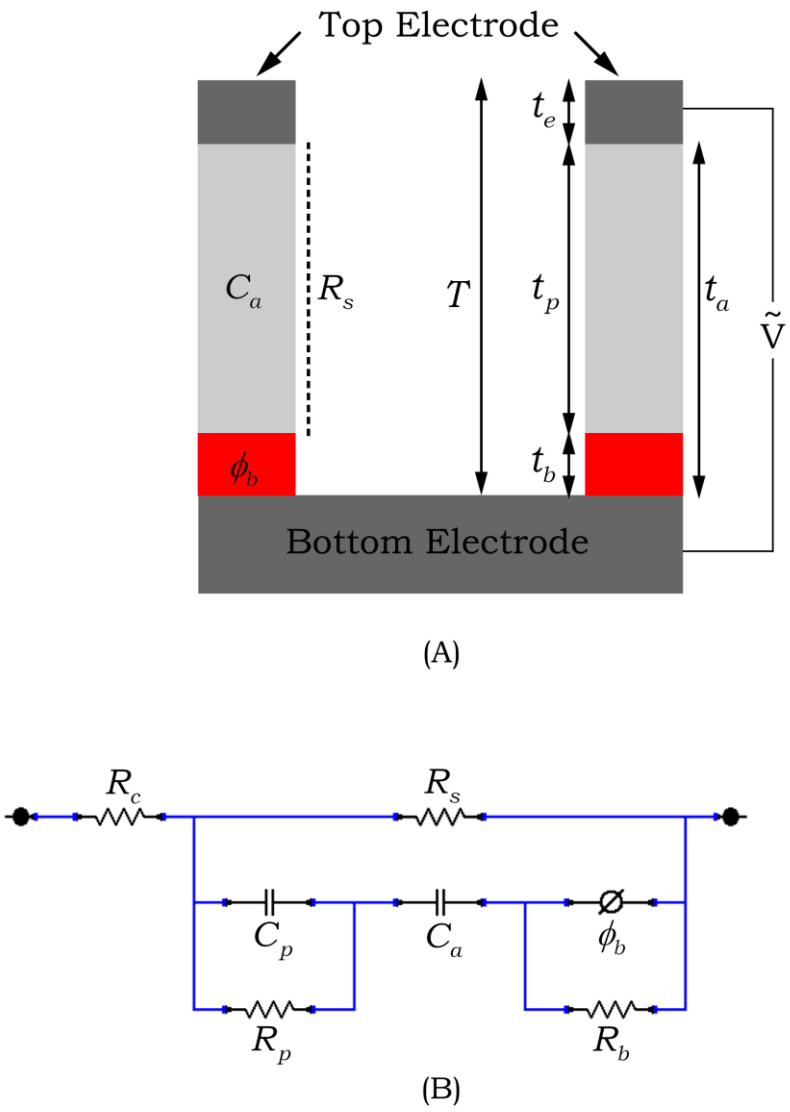

Figure 5.8. Circuit Model of MAM Structure. (A) The physical structure of the MAM device and its essential circuit components. The thickness of the top electrode, the porous-type alumina, and the barrier-type alumina was labeled as t_e , t_p , and t_b , respectively. $t_a = t_p + t_b$; $T = t_e + t_p + t_b$. (B) The equivalent circuit for the MAM structure. The porous-type alumina was modeled as C_p whereas the barrier-type oxide was modeled as a constant-phase element ϕ_b, coupled with a resistance R_b. R_s was the resistance to the current leakage along the pore walls introduced by the DNA coatings. C' and R' were considered as parasitic elements in the circuit for optimistic data fittings. R_c was the contact resistance of the circuit.

resistant component R_s between the two electrodes. If there was no current passing along the PAA pore walls, R_s should be infinitely large. Otherwise, any surface "leakage" current should cause a decrease of R_s. R_c represented the contact resistance in series with the MAM structure. The couple of C' and R' was added in the circuit to represent the possible parasitic components. Figure 5.9 shows the impedance spectrum of the unmodified MAM structure, after the oxygen plasma cleaning. The sweeping frequency range was from 0.1 Hz to 3×10^5 Hz. 10^5 Hz was the upper limit of the instrument (FAS2 Femtostat, Gamry, Inc). The lower bound was set to 0.1 Hz to best balance the frequency range and the experiment duration. The impedance and the phase angle were plotted using circles and squares, respectively. The solid lines were fitted curves based on the equivalent circuit model.

The dielectric constant for barrier-type anodic alumina ε_b was reported to be ~8.[7-9] Taking this value, the calculation of the barrier-type oxide thickness t_b was calculated to be 3.79×10^{-8} m, or ~38 nm:

$$t_b = \frac{\varepsilon_0 \varepsilon_b}{C_b} \tag{5.5}$$

This value fell in the typical thickness range of the barrier oxide fabricated under the anodization conditions described previously.

In Figure 5.8, T was 220 nm, measured from the SEM image in Figure 5.6 (B). t_e was 20 nm. Therefore t_a was 200 nm. Since t_b was ~38 nm, t_p was ~162 nm. Recall that the MAM structure had the following geometric dimensions: the capacitor area A=0.01 cm^2; the alumina porosity p =58.8%. The capacitance of the porous-type

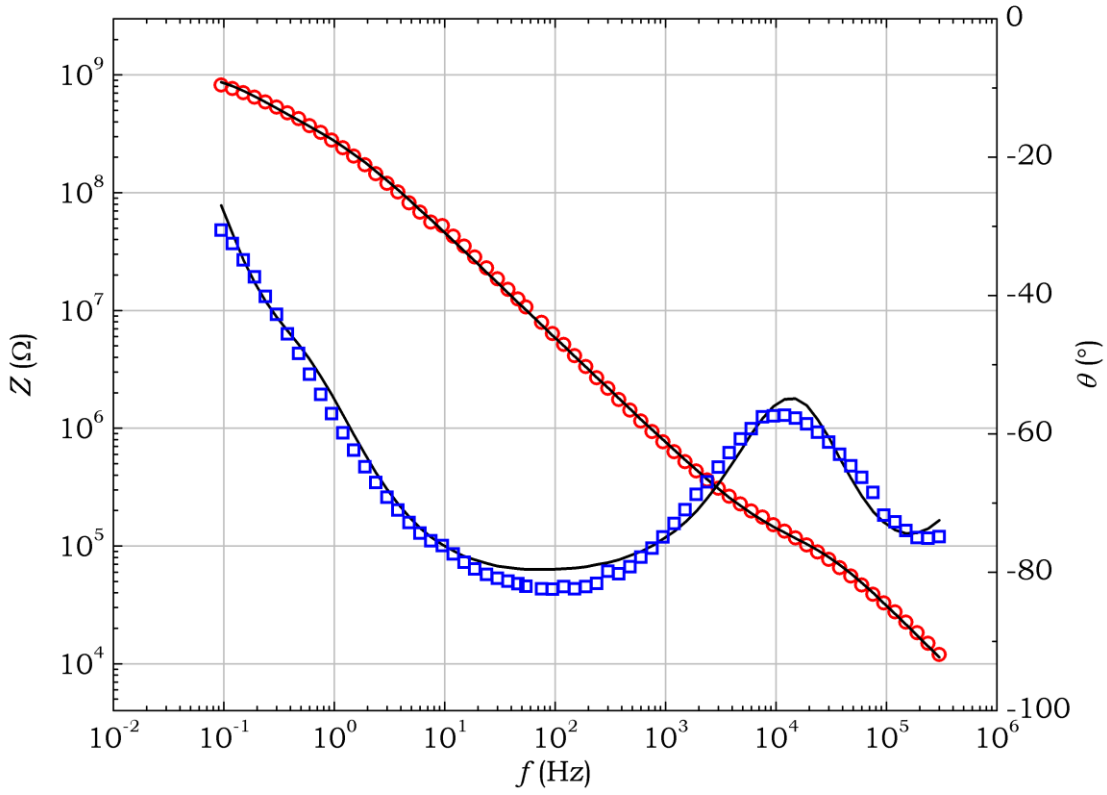

Figure 5.9. Impedance Spectrum of MAM DNA Biosensor (1). The plot shows the frequency (f) spectrum of the impedance Z (circles) and the corresponding phase angle θ (squares) of the MAM structure without chemical modifications. The solid lines are the curves fitted based on the circuit model in Figure 5.8 (B).

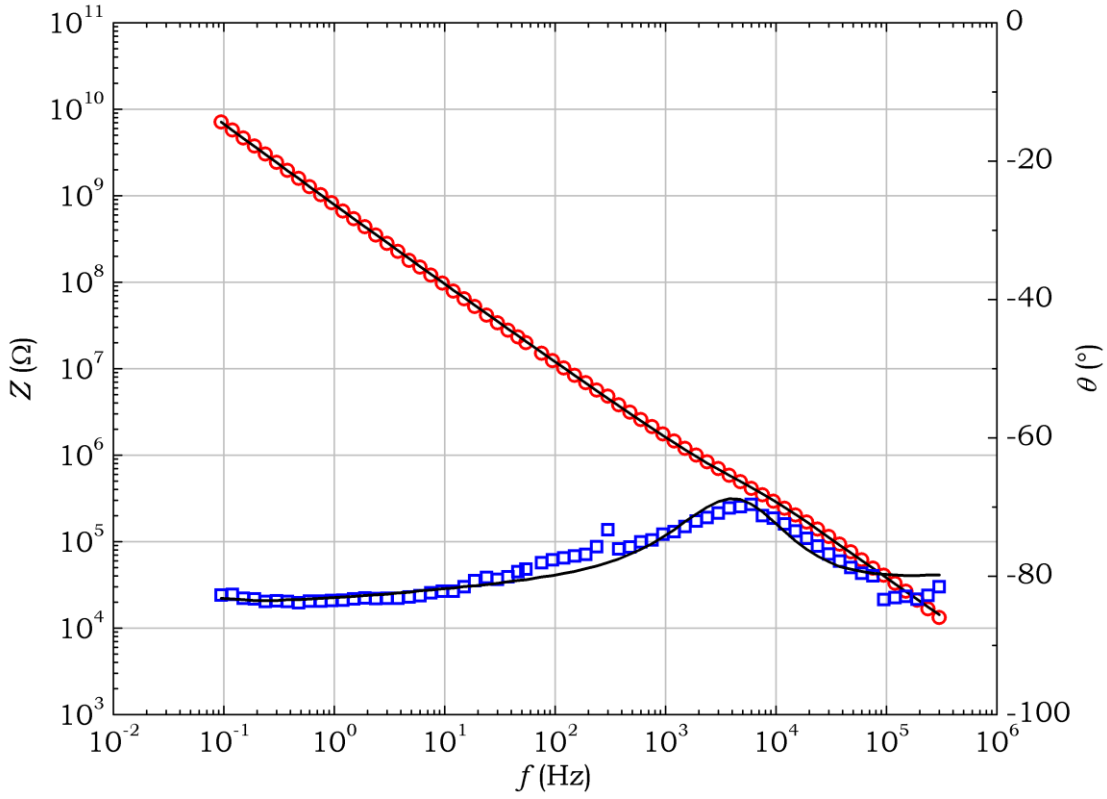

Figure 5.10. Impedance Spectrum of MAM DNA Biosensor (2). The plot shows the frequency (f) spectrum of the impedance Z (circles) and the corresponding phase angle θ (squares) of the MAM structure after the APTS silanization. The solid lines are the curves fitted based on the circuit model in Figure 5.8 (B).

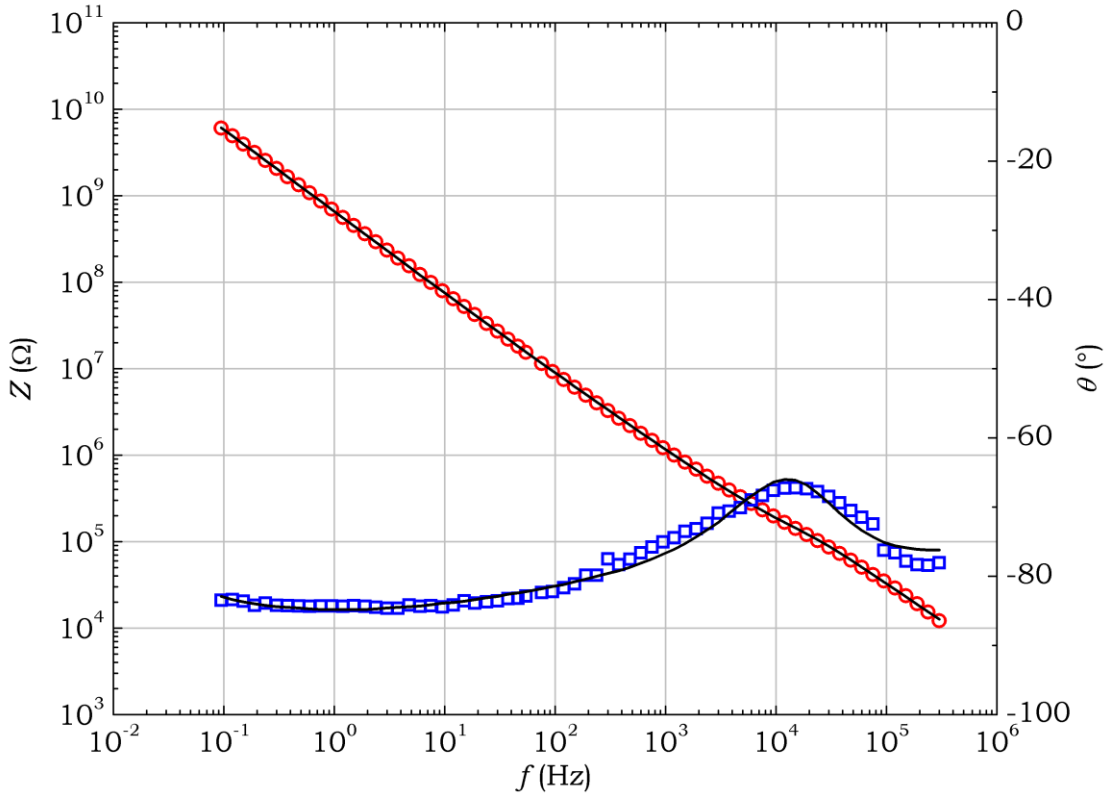

Figure 5.11. Impedance Spectrum of MAM DNA Biosensor (3). The plot shows the frequency (f) spectrum of the impedance Z (circles) and the corresponding phase angle θ (squares) of the MAM structure after the glutaraldehyde coating. The solid lines are the curves fitted based on the circuit model in Figure 5.8 (B).

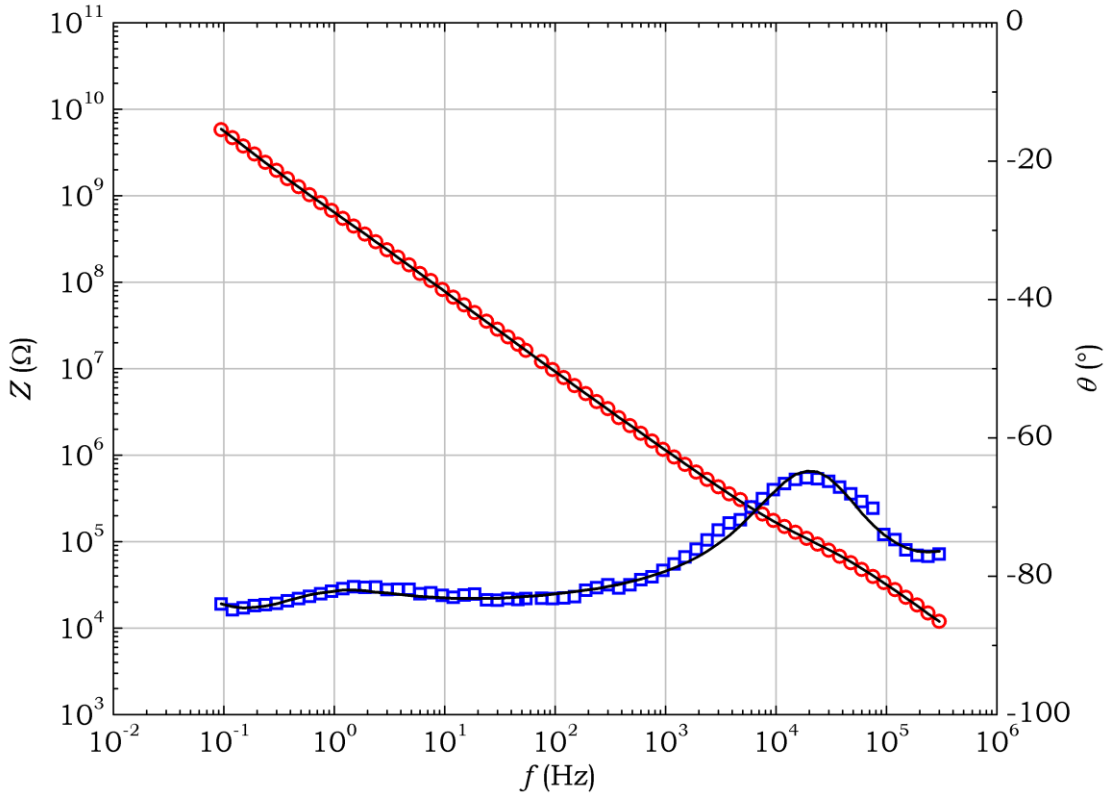

Figure 5.12. Impedance Spectrum of MAM DNA Biosensor (4). The plot shows the frequency (f) spectrum of the impedance Z (circles) and the corresponding phase angle θ (squares) of the MAM structure after the immobilization of ssDNA. The solid lines are the curves fitted based on the circuit model in Figure 5.8 (B).

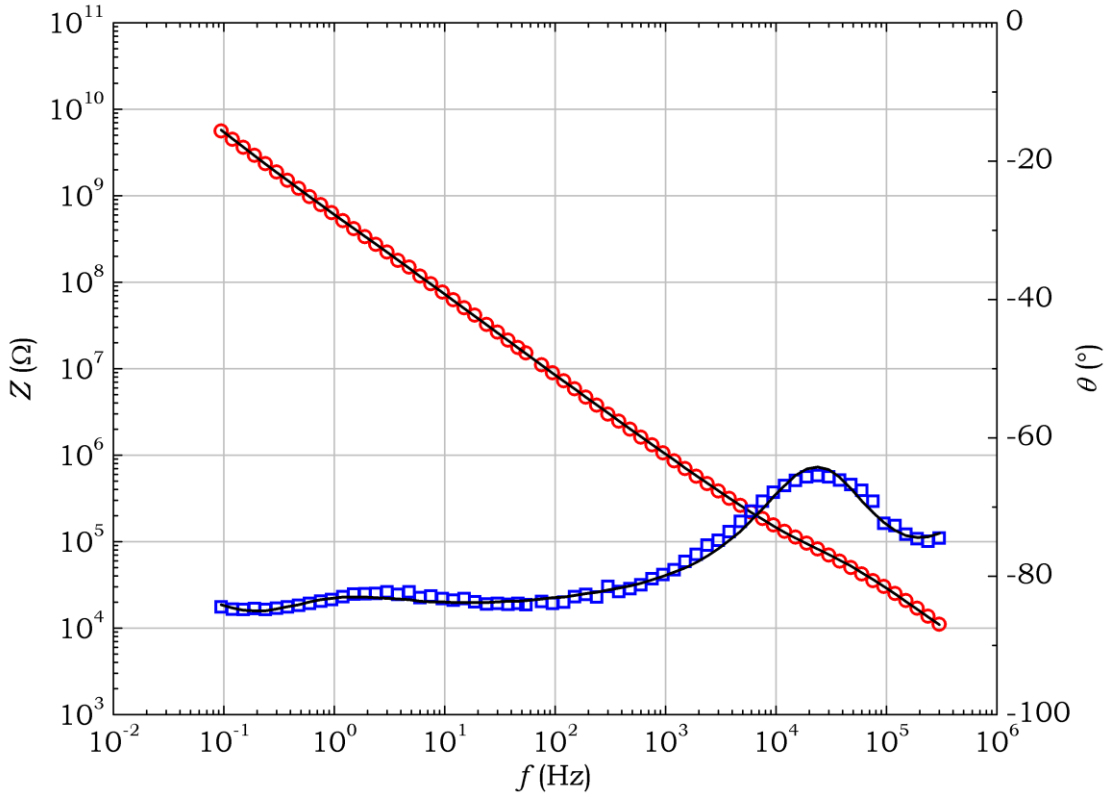

Figure 5.13. Impedance Spectrum of MAM DNA Biosensor (5). The plot shows the frequency (f) spectrum of the impedance Z (circles) and the corresponding phase angle θ (squares) of the MAM structure after the DNA hybridization. The solid lines are the curves fitted based on the circuit model in Figure 5.8 (B).

Table 5.1. Circuit Parameters of MAM Structure

	(1)	(2)	(3)	(4)	(5)
R_s (Ω)	1.06×10^{9}	5.82×10^{11}	9.76×10^{10}	8.21×10^{10}	7.50×10^{10}
Q_b (S s^n)	9.36×10^{-10}	6.05×10^{-10}	2.02×10^{-9}	1.41×10^{-9}	1.73×10^{-9}
C_b (F cm^{-2})	1.87×10^{-7}	2.91×10^{-7}	5.64×10^{-7}	2.59×10^{-7}	3.13×10^{-7}
R_b (Ω)	3.17×10^{8}	5.19×10^{10}	7.80×10^{8}	2.15×10^{8}	1.66×10^{8}
n	8.61×10^{-1}	8.35×10^{-1}	7.66×10^{-1}	8.12×10^{-1}	8.08×10^{-1}
C_p (F cm^{-2})	2.24×10^{-7}	8.73×10^{-8}	6.92×10^{-8}	6.90×10^{-8}	7.10×10^{-8}
R' (Ω)	6.89×10^{4}	1.58×10^{5}	4.73×10^{4}	3.98×10^{4}	3.28×10^{4}
C' (F cm^{-2})	2.07×10^{-8}	3.88×10^{-8}	4.03×10^{-8}	2.94×10^{-8}	3.13×10^{-8}
R_c (Ω)	1.96×10^{3}	2.54×10^{-1}	5.18×10^{-3}	6.90×10^{2}	1.10×10^{3}
ε	3.01×10^{-3}	1.39×10^{-3}	5.70×10^{-4}	3.78×10^{-4}	4.22×10^{-4}

Footnote: The table lists the circuit parameters of the MAM structure with no modifications (1), APTS silanization (2), glutaraldehyde coating (3), ssDNA immobilization (4), and DNA hybridization (5). The values were calculated by fitting the circuit model in Figure 5.8 (B) to the experiment data in Figure 5.9-5.13. ε is the goodness of fit.

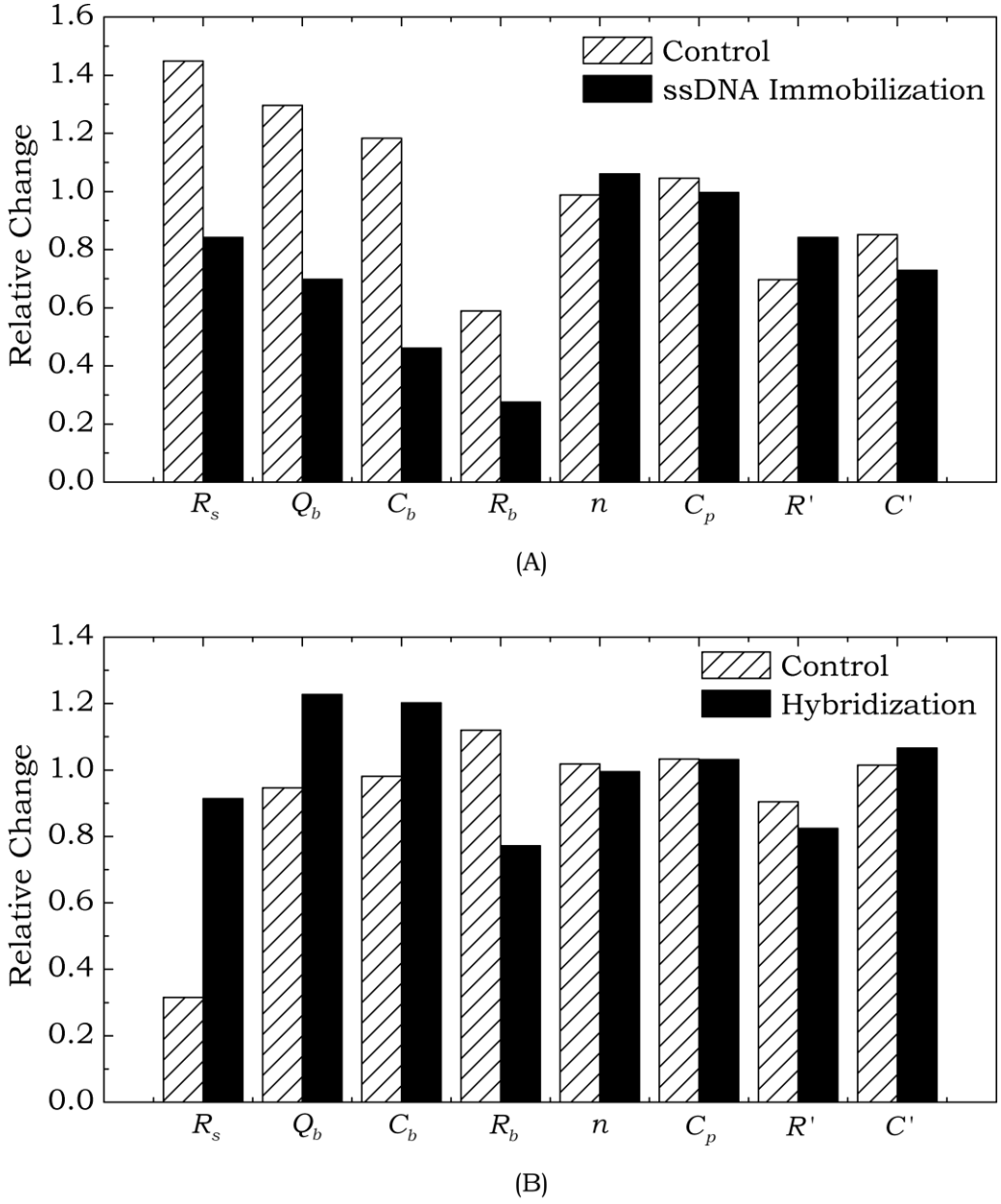

Figure 5.14. Circuit Parameters of MAM Structure. (A) The relative changes of the circuit parameters before and after the immobilization of the ssDNA probes (black) and the corresponding changes in the control experiment (textured). (B). The relative changes of the circuit parameters before and after the DNA hybridization (black) and the corresponding changes in the control experiment (textured).

alumina C_p was calculated to be 2.24×10^{-7} F cm^{-2}. The corresponding dielectric constant ε_p was calculated to be ~41:

$$\varepsilon_p = \frac{C_p \cdot t_p}{\varepsilon_0} \tag{5.6}$$

where ε_0 is the permittivity of free space. The calculated value was in a reasonable agreement with the previous work by Hitzig et al.[10], in which a high dielectric constant of ~55 was observed on the porous-type alumina because of the hydration.

R_s was calculated to be 1.06×10^{9} Ω. This resistance agreed well with the results obtained by Lee et.al.[186] who measured an off-state resistance of 10^{8}-10^{9} Ω on a non-volatile memory device that was based on a 180-nm-thick alumina membrane fabricated under the same anodization conditions. The calculated R_s corresponded to a leakage current of 9.43×10^{-12} A.

From the calculations, the parasitic capacitance C' and resistance R' were 2.07×10^{-8} F cm^{-2} and 6.89×10^{4} Ω, respectively. Compared to C_p and C_b, C' was about one order of magnitude smaller. R' was negligible in comparison with R_b. The circuit resistance R_c, was calculated to be a reasonable value of 1.96×10^{3} Ω.

The impedance spectra of the MAM structure after the APTS and glutaraldehyde treatments were recorded as Figure 5.10 and 5.11, respectively. As seen in the Figure 5.10, the impedance spectrum profiles differed greatly after the APTS treatment. The most obvious change was that the impedance increase at the low-frequency end. In the silane treatment, the PAA pore walls were coated with an organic APTS film. The wall surfaces became highly hydrophobic after the

APTS coating. Consequently, R_s increased from 1.06×10^{9} Ω to 5.82×10^{11} Ω, indicating that the leakage current along the pore surfaces was significantly diminished by the APTS passivation. The subsequent glutaraldehyde treatment reduced R_s from 5.82×10^{11} Ω to 9.76×10^{10} Ω, suggesting that the attachment of glutaraldehyde on the APTS layer facilitated the surface conduction to certain extent, possibly because of the hydrophilic –COOH groups on glutaraldehyde. But R_s was still about two orders of magnitude higher than that of the unmodified MAM structure. Similarly, R_b and R' increased in the APTS treatment but decreased in the glutaraldehyde treatment. The capacitance of the porous-type alumina C_p decreased from 2.24×10^{-7} F cm^{-2} to 8.73×10^{-8} F cm^{-2} after the APTS treatment, and further down to 6.92×10^{-8} F cm^{-2} after the glutaraldehyde treatment. The effective capacitance of the barrier-type oxide (C_b) increased from 1.87×10^{-7} F cm^{-2} to 5.64×10^{-7} F cm^{-2} after the APTS and glutaraldehyde treatments, with the ideality factor n decreased from 0.86 to 0.77. The parasitic capacitance C' increased from 2.01×10^{-8} F cm^{-2} to 4.03×10^{-8} F cm^{-2}

The ssDNA oligonucleotides were attached to glutaraldehyde though the amine-carbonyl reaction. The impedance spectrum after the ssDNA immobilization is shown in Figure 5.12. The relative changes of the circuit parameters before and after the ssDNA immobilization are presented in Figure 5.14 (A), in comparison with their corresponding changes in the control experiment. The contact resistance (R_c) was omitted in Figure 5.14, because as shown in Table 5.1, the calculation of this parameters in step (2) and step (3) yielded

values at a different scale from those in step (1), (4), and (5). This was understandable for two reasons. First, R_c could only be modeled accurately at an infinitely high frequency. However, the sweeping frequency was limited to 300 kHz at the high-frequency end. More importantly, after the APTS silanization (step (2)) and the glutaraldehyde coating (step (3)), the MAM structure was modified with the organic layers, having a very high impedance at the low-frequency end. However, R_c was a very small resistance. The curve fitting balanced over the entire frequency range and had relatively large errors on R_c. Fortunately, R_c was not the essential part of the MAM devices. Therefore it was omitted in the comparisons in Figure 5.14 without affecting the analysis on the MAM structure.

From the curve fitting, R_s decreased from 9.76×10^{10} Ω to 8.21×10^{10} Ω, by a factor of 15.9%. In comparison, the control experiment showed that R_s increased by 44.8% after the glutaraldehyde coated device was soaked in dH_2O for 1 h at room temperature. This increase of R_s was possibly due to the partial loss of the anchored glutaraldehyde molecules during the water soaking and rinsing. In contrast to this increase in the background, the decrease of R_s by 15.9% during the DNA immobilization suggested that the ssDNA oligonucleotides significantly enhanced the surface conductivity. These oligonucleotides anchored on the pore sidewalls possibly served as molecular stations, facilitating the electron transport along the pore wall surfaces. The impedance differences between the positive experiment and the negative control confirmed that the ssDNA oligonucleotides were attached to the glutaraldehyde molecules.

Another important point from the calculations was that the impedance characteristics of the barrier-type oxide changed significantly upon the ssDNA attachment. The effective capacitance of the barrier-type oxide C_b decreased by 53.9%, from 5.64×10^{-7} F cm^{-2} to 2.59×10^{-7} F cm^{-2} , whereas in the control experiment, C_b increased by 18.3%. The parallel resistance R_b decreased by 72.4%, with a decrease of 31.1% in the background. The capacitance of the porous-type alumina C_p remained almost unchanged during the ssDNA immobilization. The exact mechanism for how the ssDNA oligonucleotides changed the impedance characteristics of the barrier-type oxide still remained unclear. A plausible reason was because of the excessive mobile ions in the barrier-type oxide. During the anodization, the barrier oxide served as an active frontier where the field-assisted oxidation and dissolution took place simultaneously. Under a high electric field, cations such as Al^{3+} migrated from the Al-alumina interface to the alumina-electrolyte interface, whereas anions such as OH^- and O^{2-} migrated in the opposite direction. These cations and anions met within the barrier oxide layer to form new alumina. If the anodization was paused in the middle of the process, the electric field across the barrier oxide disappeared instantly. It was expected that there were a significant amount of free cations and anions inside the barrier oxide. Because these ions had not formed Al_2O_3 yet, the Al_2O_3 lattice of the barrier oxide was supposed to be relatively sparse compared to the regular Al_2O_3. Therefore the free ions left inside were expected to have a remarkable mobility. The distribution of these ions might change when the negatively-charged ssDNA molecules were

immobilized on the pore walls, making the barrier-type oxide behave as a variable capacitor with dynamic capacitive characteristics. On the other hand, the alumina in the bulk PAA part was much more senior in age. It was reasonable to consider that the residual cations and anions were minimal as most of them had formed to Al_2O_3. Therefore its capacitive characteristics were insensitive to the immobilization of the ssDNA molecules.

The DNA hybridization was achieved by adding the complementary ssDNA oligonucleotides into the alumina pores that were modified with the ssDNA probes. The DNA targets were prepared in TE buffer containing 1 M NaCl. The hybridization lasted for 1 h at room temperature. In the control experiment, an MAM device attached with ssDNAs was soaked in the same TE buffer without DNA targets for 1 h at room temperature. The impedance spectrum after the hybridization is shown in Figure 5.13. The relative changes of the circuit parameters before and after the hybridization are presented in Figure 5.14 (B), in comparison with their corresponding changes in the control experiment.

In the hybridization, R_s decreased from 8.21×10^{10} Ω to 7.50×10^{10} Ω, only a factor of 8.6%. However, the control experiment showed that R_s decreased by 68.5%. A possible reason for this decrease was that a trace amount of salts (NaCl) from the TE buffer were crystallized on the PAA pore sidewalls during the rinsing and drying processes. These ionic crystals could possibly facilitate the surface electron transport. Compared to the decrease of R_s by 68.5% in the control, the decrease of R_s by 8.6% in the hybridization was much less significant,

suggesting that the formation of the DNA duplex actually made the pore surface less favorable for the electron transport.

Again, the impedance characteristics of the barrier-type oxide changed significantly in the DNA hybridization. The effective capacitance of the barrier-type oxide C_b increased by 20.6%, from 2.59×10^{-7} F cm^{-2} to 3.13×10^{-7} F cm^{-2}, whereas in the control experiment C_b stayed almost unchanged. The parallel resistance R_b decreased by 22.8% but increased by 12.0% in the control experiment. The capacitance of the porous-type alumina C_p remained almost unaffected in the hybridization.

The data analysis above showed that the barrier-type oxide layer was sensitive to the DNA hybridization. The PAA film in the MAM structure had an average pore diameter (d) of 67 nm, and the thickness of the barrier-type oxide t_b was ~38 nm. Since the rise in the helix per base was 0.34 nm,[187] the 20-mer DNA molecules used in the experiments had a helix length (l) of 6.8 nm. The radius of DNA duplex molecules (r) was ~1 nm. The ssDNA immobilization procedure used in the experiments was similar to the approach by Perterlinz et al.,[188] therefore the surface density (C_s) of the ssDNA was assumed to be comparable to their result, being about 5×10^{12} cm^{-2}, or 20 nm^2 per ssDNA. Assuming the immobilized ssDNA had a hexagonal array, the separation distance (d_s) between adjacent ssDNA molecules was calculated to be 4.8 nm by the following equation:

$$d_s = \sqrt{\frac{2}{\sqrt{3}C_s}} \tag{5.7}$$

For dsDNA molecules, the minimal separation distance was $2r$, or

2 nm. However, this ideal packing density was unlikely in reality because of the strong steric hindrance for the hybridization. For this reason, the area density of the immobilized ssDNA molecules with a separation distance of 4.8 nm was reasonably high.

Since the DNA oligonucleotides were 6.8 nm in length, whereas the separation distance between adjacent molecules was 4.8 nm. If the ssDNA probes were laid down on the alumina surface, the free end of one ssDNA molecule was able to reach the base of its adjacent ssDNA. Thus the anchored ssDNAs formed a networking-like structure, which could possibly facilitate the electron transport along the surface. However, when some ssDNA probes were hybridized with the complementary DNA targets, the bridges between adjacent ssDNA probes were expected to be less as the hybridized DNA molecules were stiffer than the ssDNA probes and could possibly stand up instead of lying on the surface. This could explain the changes of R_s in the hybridization experiment and its negative control.

The amount of the ssDNA probes immobilized on the sidewalls of one single alumina pore (n^{probe}) was calculated to ~2100 by the following equation. The ssDNA immobilized on the sidewalls of the barrier-type oxide (n_b^{probe}) was a fraction (t_b/t_p) of n^{probe}, being ~400.

$$n^{probe} = \pi d t_a C_s \tag{5.8}$$

These immobilized ssDNA molecules captured the complementary ssDNA targets from the solution, forming dsDNA helix on the surface. Peterson et al.[189] reported that the capture efficiency was dependent on the area density of the immobilized ssDNA probes. The capture

efficiency was nearly 100% when the probe density was 1.5×10^{12} cm^{-2}, but less than 50% when the probe density increased to 3.0×10^{12} cm^{-2}. The hybridizations saturated after a couple of hours. In the experiments here, the probe density was assumed to be 5×10^{12} cm^{-2}. Therefore a reasonable hybridization efficiency was estimated to be ~25%. The complementary ssDNA targets captured on the sidewalls of one single alumina pore (n^{target}) was 2100×25%=525. Correspondingly, the captured targets on the sidewalls of the barrier-type oxide (n_b^{target}) were (t_b/t_p)×525, being ~100.

The sample concentration of the complementary ssDNA (C_0) was 1 μM. When the alumina pores were filled with the target solution for the hybridization, the ssDNA targets initially filled in each single pore, $\frac{1}{4}\pi d^2 T C_0 N_A$, was only ~0.4, where N_A is the Avogadro constant. The calculation indicated that there were almost no ssDNA target molecules brought in the pores by the initial filling. The ssDNA target molecules needed to diffuse into the alumina pores to be captured by the ssDNA probes on the alumina sidewalls. A concern was which step was the speed-limiting process, the diffusion or the hybridization? The diffusivity of 20-mer ssDNA was ~1×10^{-6} cm^2 s^{-1} in free solution.[190] In similar alumina pores, the confined diffusivity was reported to be 6.2×10^{-7} cm^2 s^{-1}.[45] In the analysis here, the diffusion coefficient (D) of the 20-mer ssDNA in 67-nm alumina pores was conservatively estimated to be 1×10^{-7} cm^2 s^{-1}. If the diffusion rate was slower than the hybridization rate, all the diffused DNA molecules would be captured on the alumina surface, with no excessive targets left in the pores until the hybridization was saturated. A diffusion model was established

with the following conditions: (1) the concentration of the ssDNA targets decreased linearly from C_t at the pore openings to zero at the pore bottoms, at any time t. (2) the diffusion was source limited, meaning C_t decreased as a function of time t. A guiding equation was expressed as below based on the mass conservation:

$$V(C_0 - C_t) = \int_0^t pAD\frac{C_t}{T}dt \tag{5.9}$$

where V is the sample volume of the ssDNA target solution. From this equation, the time-dependent C_t could be expressed as:

$$C_t = C_0 e^{-\frac{pAD}{VT}t} \tag{5.10}$$

The ssDNA targets diffused into each single alumina pore (n_d) within time t could be calculated as below:

$$n_d = \frac{N_A V C_0}{N_{pore}}\left(1 - e^{-\frac{pAD}{VT}t}\right) \tag{5.11}$$

Since the hybridization incubation time was 1 h, the ssDNA target molecules diffused in a single pore was calculated to be 1.8×10^4. From the previous analysis, the capture capacity of a single pore was only 525. The saturation time was on the scale of 1 h.[189] Based on these calculations, the diffusion of the target ssDNA molecules was much faster than the hybridization rate. Therefore the hybridization was the speed-limiting step, other than the DNA diffusion.

Since the ssDNA targets captured on the sidewalls of the barrier-type oxide in single pore (n_b^{target}) were ~100. The total amount of the ssDNA targets detected by the barrier-type oxide in one MAM device (N_b^{target}) was calculated to be 2.76×10^{-14} mole by the following equation:

$$N_b^{target} = \frac{n_b^{target} \cdot N_{pore}}{N_A} \tag{5.12}$$

All the captured ssDNA targets in the pore, on the sidewalls of both the porous-type alumina and the barrier-type oxide, contributed to the changes of the leakage current along the sidewall surface. Therefore the target ssDNA molecules sensed by the leakage current (N^{target}) were calculated to be 1.46×10^{-13} mole.

In the current MAM structure, the capacitor area was 1×1 mm^2. With the conventional photolithography, the area can reasonably be reduced to 1×1 μm^2. Therefore the theoretical limits of the detection by the barrier-type oxide and by the leakage current can be estimated to be another 6 orders of magnitude smaller than the current values, being 2.76×10^{-20} mole, and 1.46×10^{-19} mole, respectively. The current sample consumption of the target ssDNA was 5 µl at 1 µM, totally 5×10^{-12} mole. Based on the diffusion analysis previously, the diffused ssDNA targets in single pore within 1 h were 1.8×10^4 whereas the captured ssDNA targets were only ~525. So the concentration of the ssDNA targets can be safely reduced by one more order (5×10^{-13} mole) while still providing sufficient DNA targets for the hybridization process. For a future MAM device of 1×1 μm^2, the theoretical limit of the sample consumption will be 5×10^{-19} mole.

For a practical DNA biosensor, the limit of detection should not be the only key factor in evaluating the overall feasibility of the sensor system. Other aspects such as the detection reliability, the sensing selectivity, and the operation simplicity are often more important for achieving a realistic sensor device.

5.4 Conclusion

A DNA biosensor has been developed based on an metal-alumina-metal sandwich strcture. The sidewalls of the alumina pores were chemically activated with APTS silane and glutaradehyde, and further attached with ssDNA probe molecules. Complementary ssDNA molecules were diffused into the pores and hybridized with the immobilized ssDNA probes. The hybridization was sensed by monitoring the impedance characteristics of the MAM structure in the solid state. Based on the data analysis using an equivalent circuit model, the existance of the immoblized ssDNAs facilitated the electron transport along the surface of the pore walls, whereas the hybridization seemed to have an opposite impact. In addition, it was found that the impedance charateristics of the barrier-type oxide was sensitive to the DNA attachments possibly because of the embedded free ions. The theoretical limit of the detection was estimated to be on the order of 10^{-20} mole. The DNA biosensor developed here was featured with a full scalability, fast detection, and high resolution. The detection method was advantageous in the simplicity as it required no labellings on DNA samples and it was conducted in solid state. The device developed here provided an interesting approach for future practical DNA sensors oriented towards device miniaturization and high detection resolution. In addition, the MAM sandwich structure presented as a general system of nanogap electrode pair, with a large surface of the interior dielectric material. It will possibly be useful in the future biosensor applications.

CHAPTER 6

MICROSCALE $CD4^+$ CELL BIOSENSOR WITH SINGLE-CELL RESOLUTION FOR DIAGNOSIS OF HIV INFECTION

6.1 Background

Human immunodeficiency virus (HIV) is a lentivirus that leads to acquired immunodeficiency syndrome (AIDS). HIV primarily attacks $CD4^+$ T helper lymphocytes, macrophages, and dendritic cells in the human immune system. The progressive decline of the $CD4^+$ helper cells eventually leads to the loss of cell-mediated immunity, making the infected human bodies vulnerable to life-threatening opportunistic infections. According to the recent report by Joint United Nations Programme on HIV/AIDS (UNAIDS),[191] 30-36 million people were living with HIV in 2007, together with 2.7 million new HIV infections and 2 million HIV-related deaths. Since its first recognition in 1981, HIV has been spread globally nowadays, especially in the developing countries in sub-Saharan Africa, where it accounted for 67% of the total population living with HIV and 75% of AIDS deaths in 2007.

The number of $CD4^+$ helper cells correlates with the status of the HIV infection. Clinically, an adult is considered to be healthy (no HIV infection) if the $CD4^+$ helper cells are more than 500 μl^{-1}. If the cells are below 200 μl^{-1}, the person is defined to have AIDS as his immune system is considered to be no longer strong enough to prevent opportunistic infections. Therefore the quantification of the amount of $CD4^+$ helper cells is important for inspecting the HIV infection, diagnosing the infection stage of AIDS patients and determining the corresponding antiretroviral treatments. The standard technique used for counting $CD4^+$ helper cells is flow cytometry. In flow cytometers, fluorescence tagged cells form a line and pass through a detection

gate, scanned individually by a laser beam. The cell types are distinguished by the fluorescent chemicals that are attached to the cells through specific antigen-antibody recognitions. However, flow cytometry has its drawbacks such as sophisticated equipments, expensive costs and complicated operations. To meet the heavy needs of health care in resource-limited regions, affordable point-of-care diagnostic tools capable of quantifying $CD4^+$ cells with a minimum volume of whole blood sample are emphasized to be developed. Towards this direction, $CD4^+$ counting devices based on different detection methods have been reported in recent years. Rodriguez et al.[192] developed a membrane-based microchip, in which $CD4^+$ cells were harvested on porous polycarbonate membranes by filtering red blood cells through the membrane pores. Labeled with type-specific fluorescent antibodies, the $CD4^+$ cells were imaged under fluorescence microscope and were enumerated by digital image processing. In comparison with the flow cytometry, however, the fluorescence method existed with relatively large counting errors. Cheng et al.[193,194] fabricated a microfluidic device, in which blood samples flowed through a 50-μm-deep microfluidic channel that was modified with $CD4^+$ antibodies on the surface. The $CD4^+$ cells were separated from other types chromatographically and captured on the channel surface. The cell detection and counting was achieved by fluorescent labeling. Similar microfluidic channels were developed by Thorslund et al.,[195,196] who used polydimethylsiloxane (PDMS) as the primary material for the channel construction. In addition, semiconductor materials and structures were also used in the $CD4^+$ counting devices.

Jokerst et al.[197] labeled $CD4^+$ cells with quantum dots and detected the cells utilizing the unique optical properties of the quantum dots. Wang et al.[198] used a MOSFET to count the total cell passages by amplifying the resistive pulses when the cells passed through the detection gate. Besides the optical detections, electrical methods were also adopted in the $CD4^+$ counting devices. Mishra et al.[199] developed a microchip biosensor in which the $CD4^+$ cells were captured on antibody-coated microelectrodes and sensed by electrochemical impedance spectrum measurements. Cheng et al.[200] quantified the $CD4^+$ cells captured in the microfluidic channel by measuring the conductivity changes of the liquid medium caused by the release of ions from the cell lysis.

These reported methods could potentially be integrated in the future practical devices. However, the counting accuracies of these methods were not satisfactory yet. The quantification error was generally proportional to the total counted cells. On the other hand, it was also difficult to count cells precisely when the total cell amount was small (e.g. <100). Therefore, a precise quantification of $CD4^+$ cells, independent of the dynamic range of the cell population, still remains a challenge. To solve the problem, a new impedance biosensor has been developed here, in which the sensor core consisted of an array of densely packed working electrode pixels, each being able to independently sense one $CD4^+$ cell. With this biosensor, the detection of $CD4^+$ cells at a single-cell resolution has been successfully demonstrated.

6.2 Methods

6.2.1 Pixelated Three-Electrode System

4-inch double-side polished silicon wafers with an orientation [100] (Silicon Quest, Inc) were cleaned in APM (NH_4OH:H_2O_2:H_2O =1:1:6 at 70 °C) for 10 min and in HPM (HCl:H_2O_2:H_2O =1:1:6 at 70 °C) for 10 min. A 300-nm-thick low-stress Si_3N_4 film was deposited on the silicon substrate by LPCVD (DCS:NH_3=84 sccm: 22 sccm, 200 mTorr, 800 °C). The adhesion promoter MicroPrime MP-P20 (Shin-Etsu MicroSi, Inc) was spun on the wafers at 3000 rpm for 30 sec, followed by spin coating the photoresist SPR955-CM 0.9 (MEGAPOSIT™) at 3000 rpm for 30 sec. After baking at 90 °C for 90 sec, the photoresist was exposed by autostep for 0.25 sec. The wafers were then under the ammonia baking at 90 °C for 80 min, flood exposed for 60 sec, and developed in 300 MIF (AZ Electronic Materials, Corp) for 60 sec. To remove the residual photoresist, the wafers were descumed by oxygen plasma cleaning at 80 °C for 1 min. The wafers were deposited with Cr (Research and PVD Material, Corp) at 1 Å sec^{-1} for 20 nm, followed by depositing Au (Research and PVD Material, Corp) at 2 Å sec^{-1} for 200 nm. The Au electrode pattern was finalized by soaking the wafers in the photoresist stripper 1165 (Rohm and Haas Electronic Materials, LLC) overnight.

After rinsing with dH_2O and drying under N_2 gas flow, the wafers were descumed by oxygen plasma cleaning at 80 °C for 60 sec. A 2-μm-thick PECVD Si_3N_4 film was deposited on the wafers as a passivation layer (IPE system, 200 °C for 130 min). To open the

electrodes, the photoresist SPR955-CM 0.9 was spun on the wafers at 4000 rpm for 30 sec and baked at 90 °C for 90 sec. After exposing by autostep for 0.25 sec, the photoresist was developed in 300 MIF for 1 min, rinsed with dH_2O and dried under N_2 gas flow. After descumed by oxygen plasma cleaning at 80 °C for 1 min, the wafers were under a CF_4 reactive ion etch for 25 min (chamber pressure: 40 mTorr, RF power: 150 watts, CF_4 flow rate: 30 sccm) to remove the Si_3N_4 on the top of the electrodes. The fabrication schematic is shown in Figure 6.1.

6.2.2 Cell Culture

The J45.01 cells, purchased from American Type Culture Collection (ATCC), were used as the mimic human $CD4^+$ T lymphocytes. The cells were cultured in the RPMI-1640 medium (ATCC) containing 10% fetal bovine serum (FBS) (ATCC), at 37 °C with 5% CO_2. The medium was refreshed every 2 to 3 days. For measurements, the cells were harvested by centrifuging at 1200 rpm for 5 min. The supernatant fluid was disposed and the cells were resuspended in PBS buffer (Hyclone®) with a final concentration of ~100 μl^{-1}.

6.2.3 Cell Capture on Working Electrode

The Au working electrodes were rinsed thoroughly with acetone, isopropanol, and dH_2O in series, followed by drying under N_2 gas flow. Optionally, the electrodes were under the sonication in ethanol for 2 min. After the cleaning, the devices were soaked in the freshly prepared mixture of 25 mM 11-mercaptoundecanoic acid (MUA) (Sigma-Aldrich, Co) and 25 mM 3-mercaptopropionic acid (MPA)

(Sigma-Aldrich, Co) in ethanol (MUA:MPA=1:10 v/v) for 15 h at room temperature. The working electrodes were rinsed with acetone and dried under N_2 gas flow. The electrodes were then soaked in an aqueous solution of 100 mM *N*-(3-dimethylaminopropyl)-*N'*-ethylcarbodiimide hydrochloride (EDAC) (Sigma-Aldrich, Co) and 25 mM *N*-hydroxysulfosuccinimide sodium salt (sulfo-NHS) (Sigma-Aldrich, Co) for 1 h at room temperature. After rinsing with dH_2O, 1 µl of 0.5 µg μl^{-1} anti-human $CD4^+$ antibody (BD Biosciences, Inc) was applied on the array of working electrodes and incubated at room temperature for 1 h. Afterwards, the working electrodes were rinsed with PBS buffer, followed by applying 1µl of 0.1% bovine serum albumin (BSA) solution (Sigma-Aldrich, Co) and incubating at room temperature for 1 h. After rinsing the electrodes with PBS buffer carefully, the J45.01 cells were applied on the working electrodes and left at room temperature for 30 min. The excessive cells were removed by dipping the electrodes in PBS buffer carefully. The devices were then ready for the EIS measurements. The schematic of the surface modifications is shown as Figure 6.3.

6.2.4 Electrochemical Impedance Spectroscopy

The cells were detected by measuring the electrochemical impedance spectrum changes introduced by the cell attachment. The impedance measurements were taken under the three-electrode mode in the aqueous phase. The counter electrode, the reference electrode, and the cell-coated working electrode were connected through PBS buffer. A polydimethylsiloxane (PDMS) sheet patterned with an open

channel was placed on the sensor device to serve as a buffer container. The open channel was aligned with the array of the working electrode in the chip center. The three types of electrodes were within the channel, being expose to air. PBS buffer was added into the channel, connecting the three electrodes. Another PDMS sheet was then placed on the top of the previous one, covering the channel completely. This second PDMS layer was for preventing the evaporation of the PBS buffer. With this encapsulation, the device was able to last for hours without drying.

The instrument used for the EIS measurements was FAS2 Femtostat from Gamry, Inc. The measurements were operated by the Gamry software "Framework" version.4.35. The impedance data were analyzed using the Gamry software "Echem Analyst" Version.1.35

The sweeping frequency range was 0.1 Hz-300 kHz. The applied ac voltage was 10 mV. The dc bias was set to be 0 V relative to the open circuit potential. The initial delay for the system stabilization was set to be 100 sec. Impedance data were collected 10 points per decade of the frequency. The measurements were performed at room temperature with minimized vibration noise.

The impedance spectra of the working electrode pixels at the following stages were also measured for the characterization purpose: (1) the unmodified electrodes (2) the electrodes after the MUA/MPA treatment (3) the electrodes after the sulfo-NHS/EDAC treatment (4) the electrodes after the antibody attachment.

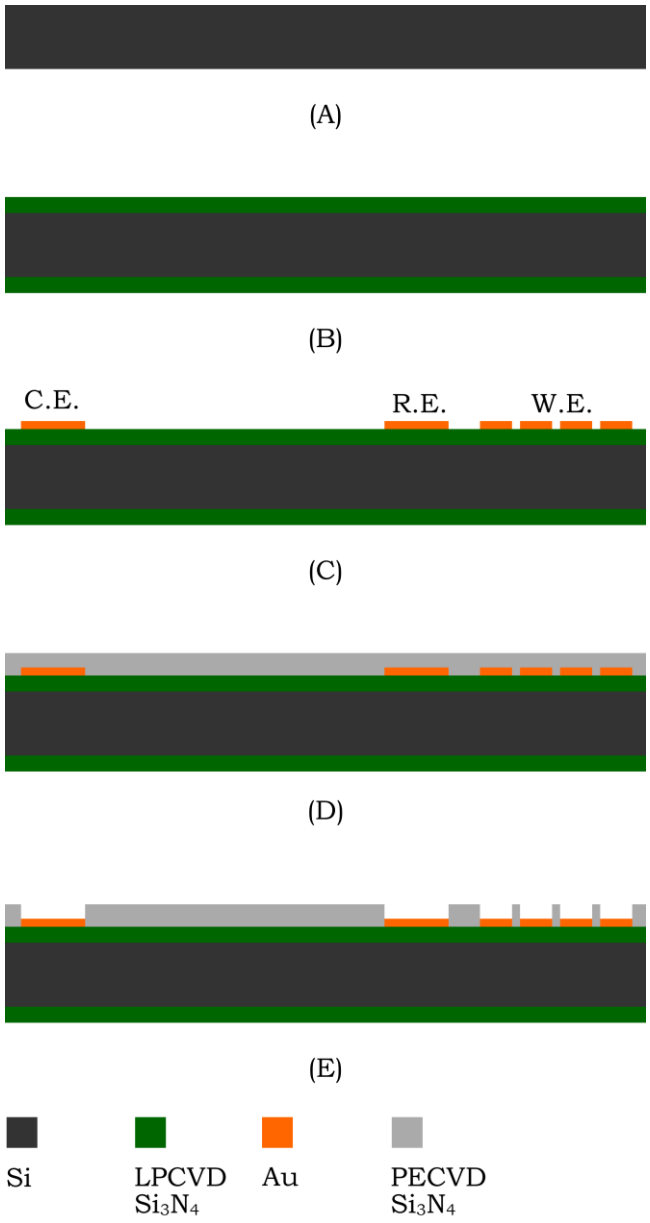

Figure 6.1. Fabrication of $CD4^+$ Cell Biosensor. (A) A Si substrate. (B) The Si substrate deposited with a 300-nm-thick LPCVD Si_3N_4 film. (C) The three-electrode system by a patterned deposition of 200-nm-thick Au film, consisting of a counter electrode (C.E.), a reference electrode (R.E.), and an array of working electrodes (R.E.). (D) The surface passivation by depositing a 2-μm-thick PECVD Si_3N_4 layer. (E) The Si_3N_4 removal on the top of the electrodes by CF_4 reactive ion etch.

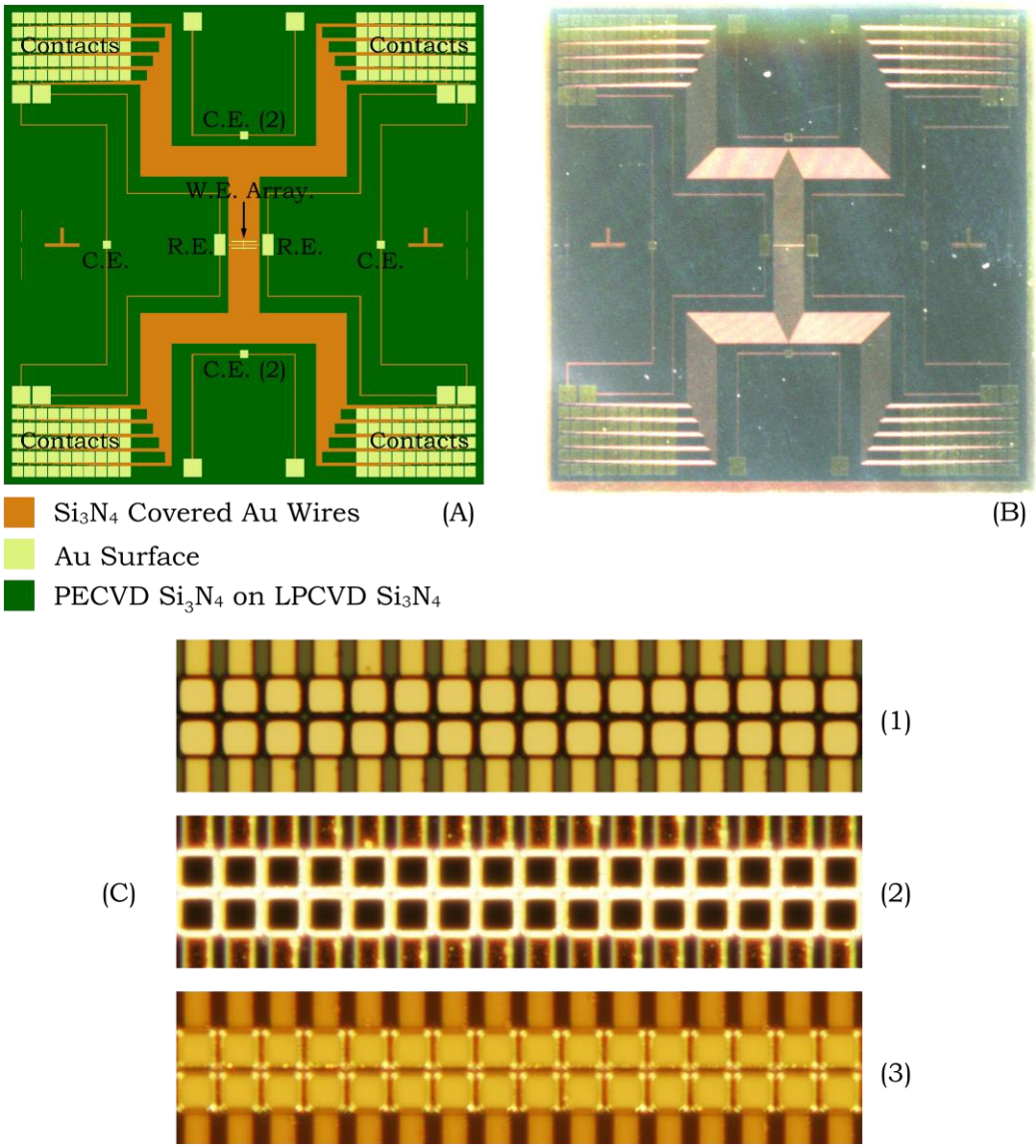

Figure 6.2. Top View of $CD4^+$ Cell Biosensor. (A) The CAD of a biosensor chip. 200 working electrodes (W.E.) were located in the chip center, each of which was connected to a contact pad at the corner. Reference electrodes (R.E.) were close to the W.E. array whereas the counter electrodes (C.E.) were far away from the center. A second set of C.E. was added for optional use. (B) An image scanned from a realistic biosensor chip. (C) The optical images of the W.E. array under the bright-field (1), dark-field (2), and DIC mode (3). Each working electrode was 7×7 μm^2 in size, with an interval distance of 9 μm. The black squares under mode 2 indicated that the working electrodes were flat and clean. In mode 3, the connection lines and the squares showed different colors, suggesting that the PECVD Si_3N_4 on the top of the working electrodes had been removed by the CF_4 dry etch.

6.3 Results and Discussion

Figure 6.2 (A) shows the CAD of the biosensor chip. The overall chip size was 1.4×1.4 cm^2. An array of 200 working electrodes was located in the center of the chip. The two rectangles near to the working electrodes were the reference electrodes, each having an area of 300×600 μm^2. Two sets of counter electrodes were located relatively far away from the working electrodes. One set was aligned with the center horizontally and the other vertically. Each counter electrode had a surface area of 300×300 μm^2. At each corner were arranged 50 identical contact pads, connecting to 50 working electrodes in the center individually through 4-μm-wide conduction lines. Each contact pad was 300×300 μm^2 in size. The contact pads for the reference and counter electrodes were 500×500 μm^2 each, connected to the corresponding electrodes through 20-μm-wide lines. Figure 6.2 (B) is the image scanned for a realistic biosensor chip.

Figure 6.2 (C) are the optical images of the working electrodes located in the center of the chip. Each working electrode was 7×7 μm^2, with a gap of 2 μm between any adjacent electrodes. Since the diameter of $CD4^+$ cells was typically 8-10 μm, the size of the working electrodes was designed to comparable to a single $CD4^+$ cell such that each working electrode was able to capture one cell only. Therefore, the “on” or “off” state of each working electrode could be represented by the binary status of the cell occupancy on the electrode (“occupied” or “empty”). The 200 working electrodes were arranged in two lanes, each having 100 electrodes. In this demonstration work, the electrodes

were designed with this “double-lane” layout such that the connection lines could be nicely arranged aside of the lanes. In the future, the electrode array can possibly be constructed by the “backplane” technique, which is used for fabricating the pixel array of LCD monitors. The entire chip was deposited with a 2-μm-thick Si_3N_4 layer to passivate all the connection lines. The Si_3N_4 on the top of the electrodes and the contact pads were removed by the CF_4 plasma etch. The opening windows were identical to the electrodes in size. The three electrodes were connected through PBS buffer. All the connection lines were covered with the 2-μm-thick Si_3N_4 layer, being insulated from PBS buffer.

The surface of the working electrodes was modified with $CD4^+$ antibodies through three steps of crosslinkings. The reaction mechanism is shown in Figure 6.3. First, the Au surface was modified with the carboxyl-terminated MUA/MPA through the Au-thiol affinitive binding. MUA/MPA was sensitive to moisture, so the reagent needed to be prepared freshly every time prior to the experiment. Second, with the presence of EDAC, sulfo-NHS reacted with the carboxyl group on MUA/MPA, forming a carboxylate intermediate. In the last, $CD4^+$ antibodies were attached to the MUA/MPA by replacing the sulfo-NHS in the carboxylate intermediate. The working electrodes were rinsed with PBS buffer and applied with 1μl of 0.1% BSA solution for 1 h to minimize the non-specific binding sites. 1 μl of J45.01 cells with a concentration of ~100 μl^{-1} was applied on the antibody-coated working electrodes for 30 min at the room temperature. The $CD4^+$ antibodies selectively captured the J45.01 cells through the antibody-antigen

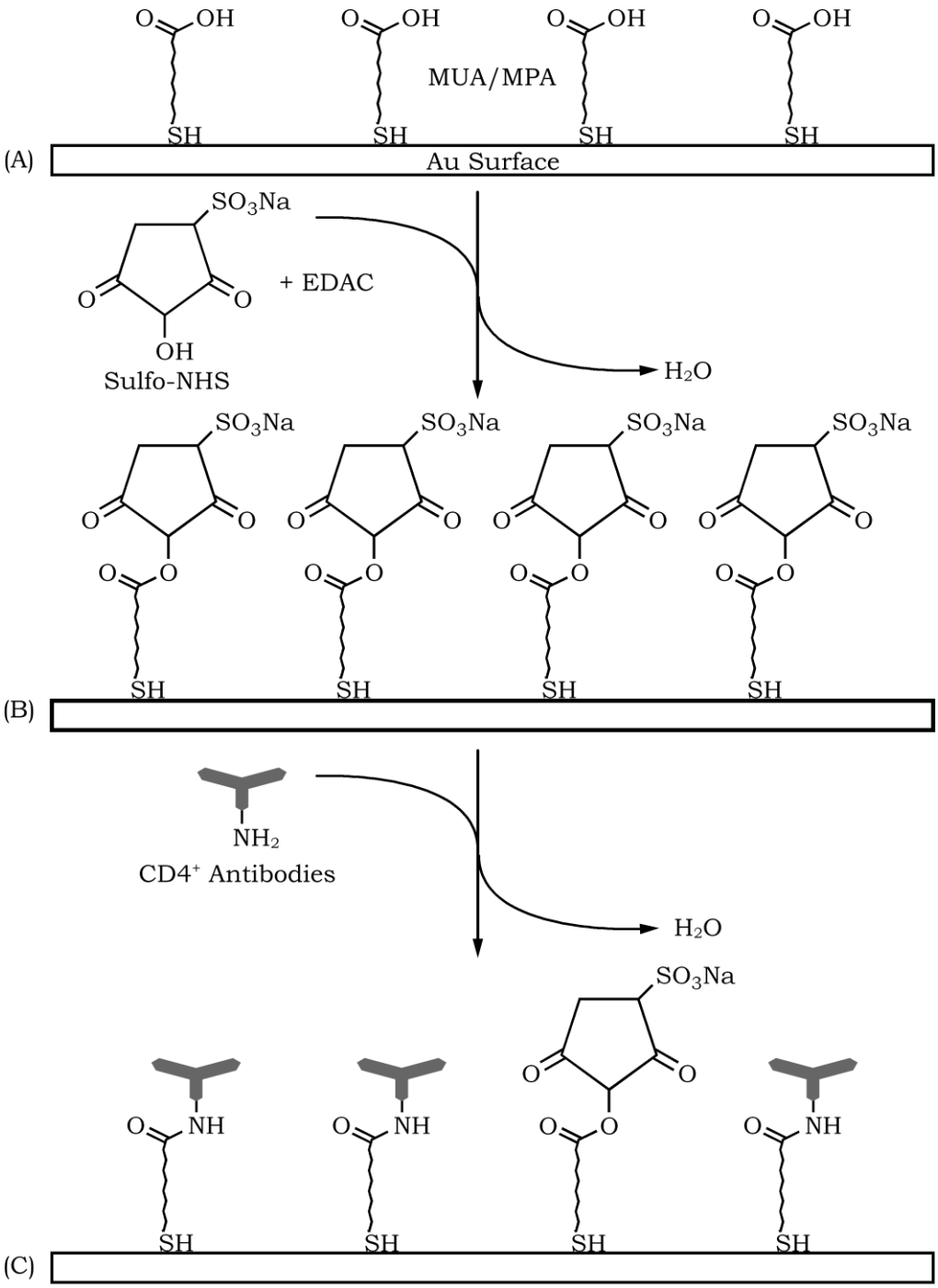

Figure 6.3. Surface Chemistry on $CD4^+$ Cell Biosensor. (A) MUA/MPA self assembled on the Au surface via the thiol-Au affinity. (B) The protection of the carboxyl group by sulfo-NHS, forming a sulfo-NHS ester intermediate. (C) The attachment of $CD4^+$ antibodies to the MUA/MPA layer by replacing sulfo-NHS, possibly with residual sulfo-NHS ester unreacted.

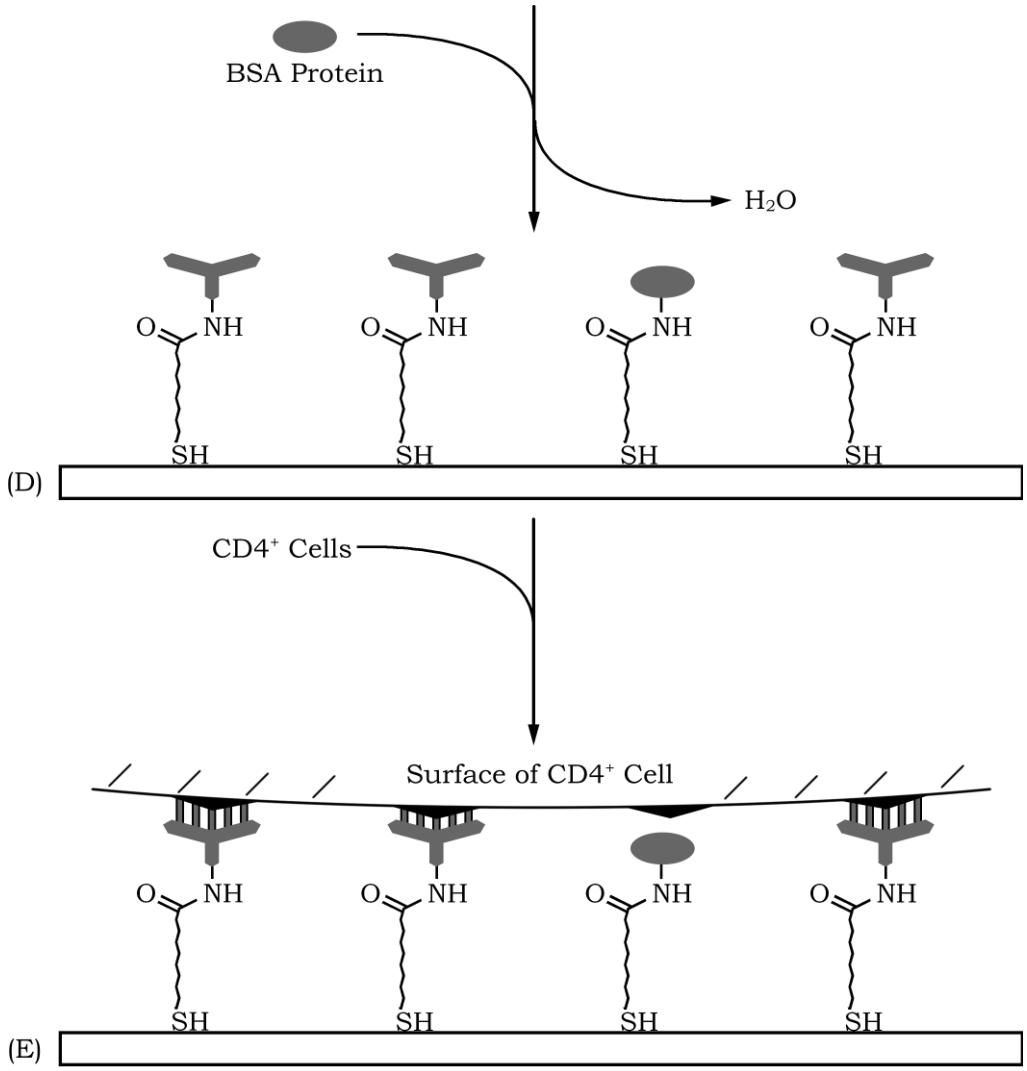

Figure 6.3. Surface Chemistry on $CD4^+$ Cell Biosensor (continued). (D) The addition of BSA proteins, blocking the non-specific binding sites by reacting with the residual sulfo-NHS ester. (E) The capture of $CD4^+$ cells (J45.01) on the electrode surface by the specific antigen-antibody recognition.

recognition. The electrodes were slowly immersed in PBS buffer to rinse off the cell solution. The working electrodes coated with the J45.01 cells were inspected under microscope in the dark-field mode, shown in Figure 6.4. In the image, each dark square was a single working electrode in the "off" state (no cell attached), whereas each bright spot was an electrode in the "on" state (attached with one single J45.01 cell on the surface). As the image shows, the surface area of each working electrode was comparable to the cell size. All the cells were well located in the center of the working electrode. The success of this precise alignment was primarily due to the surrounding Si_3N_4 layer. The Si_3N_4 grid between adjacent electrodes served as 2-μm-tall bounding walls, which was crucial for centering the cells on the electrodes when the cells landed on the electrodes. This aligned attachment was important for achieving the binary state of the cell occupancy. Figure 6.4 (B) is the surface profile across a few empty working electrodes, scanned by profilometer. It clearly showed the periodic Si_3N_4 grid structure.

The impedance spectrum of a blank sensor device, as well as that after each step of the surface modifications, was measured in PBS buffer, within a frequency range from 0.1 Hz to 300 kHz. The recorded spectra are displayed in Figure 6.5. The overall impedance spectra had an approximately linear dependence upon the frequency in the log-log Bode plot, ranging from ~10^{10} Ω at the low-frequency end to ~10^4 Ω at the high-frequency end. The associated phase angles (θ) were less than -70°, suggesting that the total impedances were dominated by the capacitive components in the circuit. For this type of three-

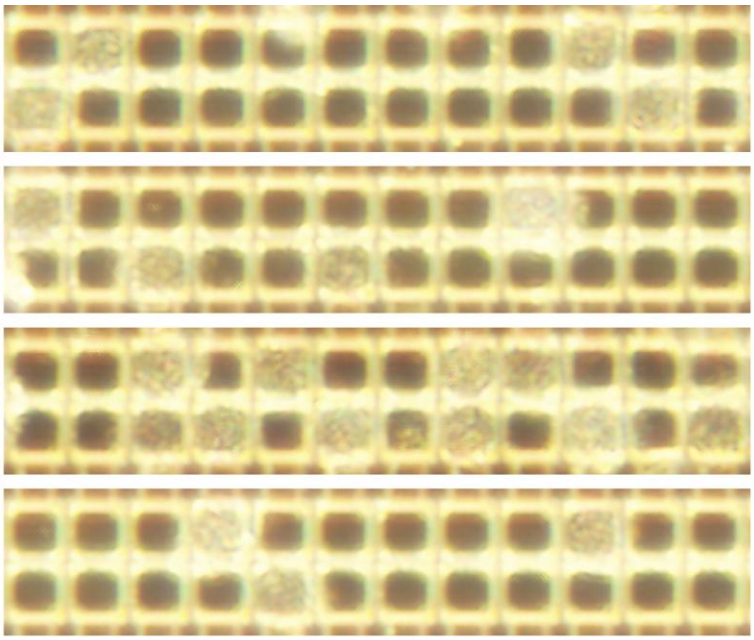

(A)

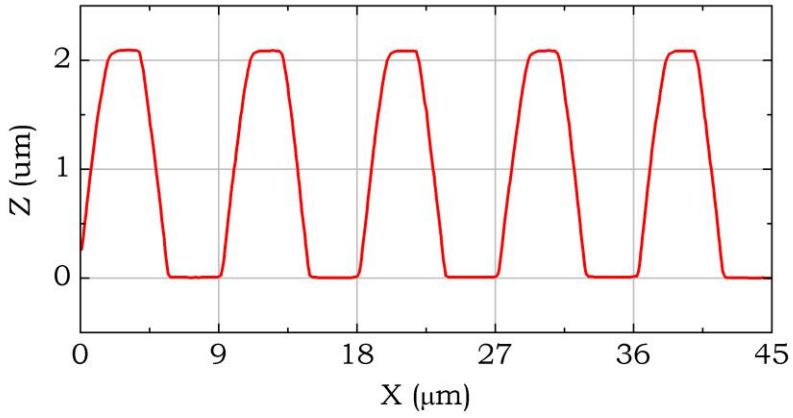

(B)

Figure 6.4. Cell Capture on $CD4^+$ Cell Biosensor. (A) The working electrodes captured with $CD4^+$ cells. The image was taken under the dark-field mode, showing the electrodes captured with a single cell on the surface (bright spots), as well as the electrodes with no cells captured (dark spots). The on-and-off state of the working electrodes was clearly represented by the binary status of the cell occupancy. (B) The cross-sectional profile scanned across a few empty working electrode pixels, showing the 2-μm-high PECVD Si_3N_4 grid structure between adjacent electrode pixels. Because of this grid structure, all the captured cells were well centered on the working electrodes.

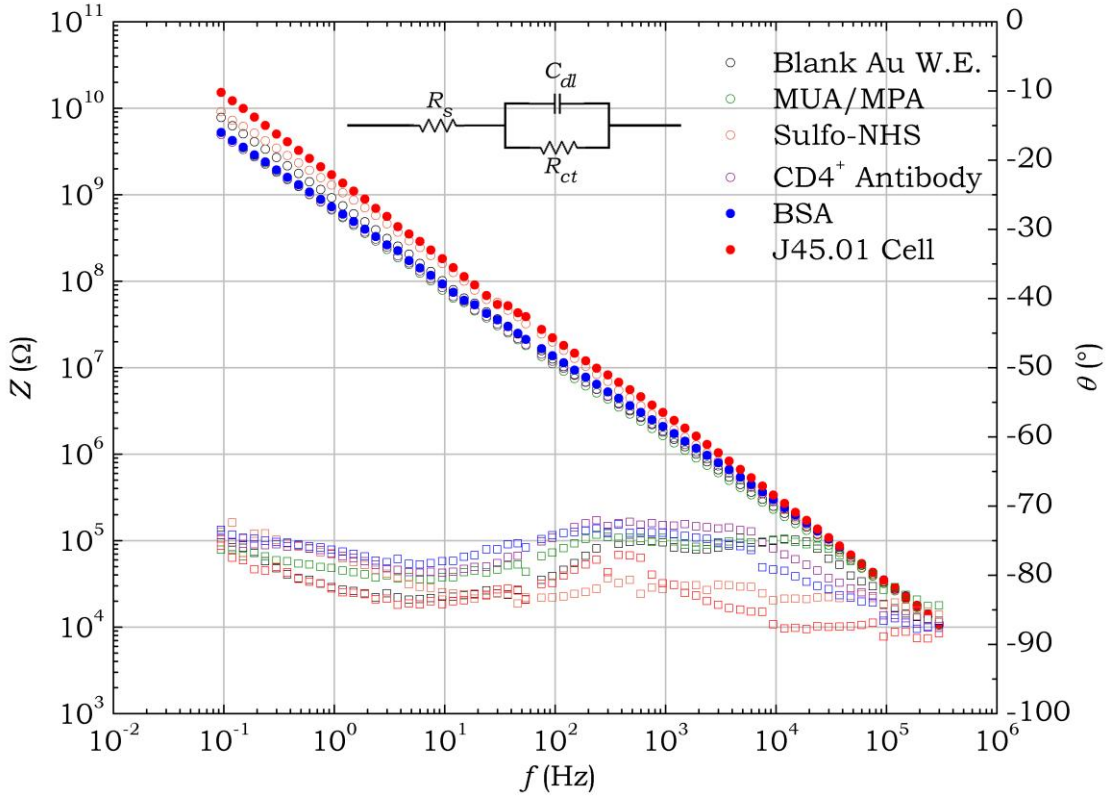

Figure 6.5. Impedance Spectra of CD4+ Cell Biosensor. The frequency (f) spectrum of the impedance (Z) (circles) and the corresponding phase angle (θ) (squares) of a working electrode with: no chemical modifications (black), MUA/MPA monolayer (green), sulfo-NHS coating (yellow), CD4+ antibody attachment (purple), BSA blocking (blue), and cell capture (red). The inset shows a simple Randles circuit model, consisting of three elements: the resistance of the buffer solution (R_s), the capacitance of the electric double layer (C_{dl}), and the resistance of charge transfer (R_{ct}).

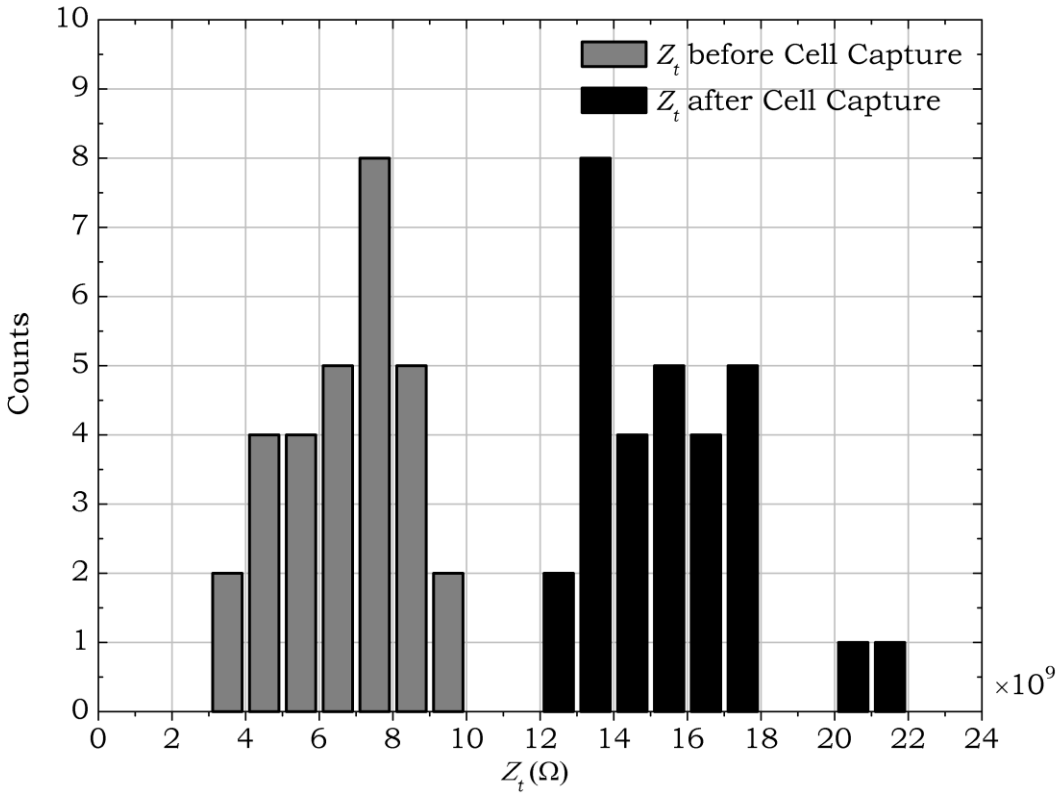

Figure 6.6. Impedances before and after Cell Capture. The histogram shows the distribution of the total impedance (Z_t) measured from 30 working electrode pixels before (gray) and after (black) the cell capture.

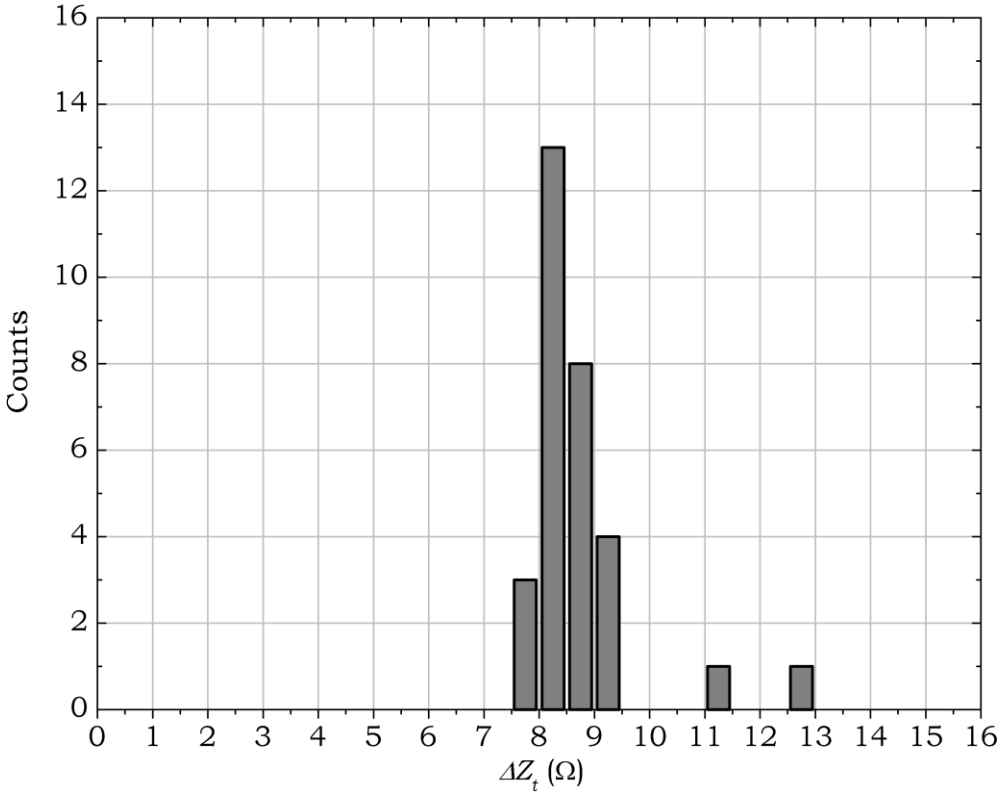

Figure 6.7. Impedance Change by Cell Capture. The histogram shows the distribution of the impedance change (ΔZ_t) introduced by the cell capture. The data were measured from 30 working electrode pixels.

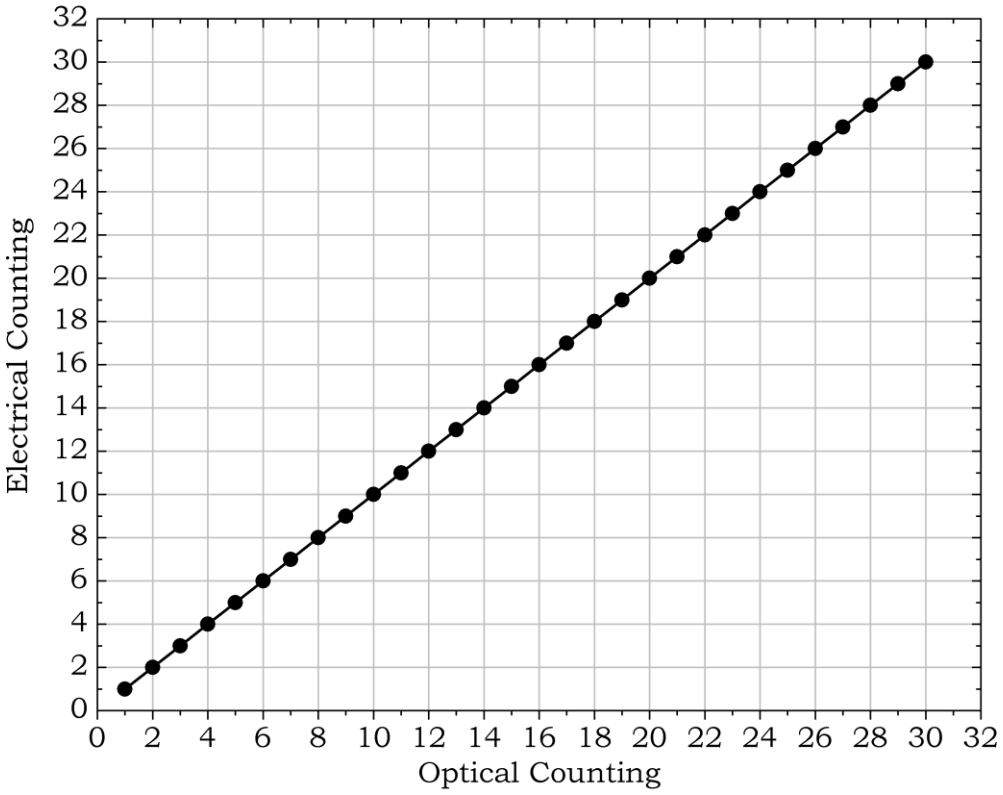

Figure 6.8. Counting Accuracy of $CD4^+$ Cell Biosensor. The plot shows a linear relation between the cells counted by the optical microscopy and the ones by the pixelated impedance sensor, demonstrating the single-cell accuracy of the impedance sensor for counting a low amount of $CD4^+$ cells.

electrode interfacial impedance sensor, the simplest equivalent circuit could be represented by the Randles circuit model (the inset in Figure 6.5), in which one resistor R_s connected with another RC couple in series. R_s was the ohmic resistance of the PBS buffer. R_{ct} was the charge-transfer resistance across the interface between the electrode surface and the aqueous buffer solution, and C_{dl} was the capacitance introduced by the electric double layer in the vicinity of the electrode surface. The total impedance was $R_{ct} + R_s$ at the low-frequency extreme, and R_s at the high-frequency extreme. The events occurring on the working electrode were reflected by the changes of R_{ct} and C_{dl}.

As seen from the figure, the impedance spectra before and after the electrode was attached with a single J45.01 cell were significantly different. The total impedance (Z_t) increased by ~10^{10} Ω at the low-frequency end (0.1 Hz), suggesting that the presence of the single cell on the electrode posed a significant resistance to the current passage at the low-frequency end. The changes of the low-frequency impedance between earlier surface modification steps (step 1-5) were noticeable. After the Au electrode was coated with MPA/MUA, Z_t at 0.1 Hz decreased by 2.58×10^9 Ω, indicating that the MPA/MUA film facilitated the interfacial charge transport possibly because of the hydrophilic carboxyl (–COOH) terminals. The subsequent modification with sulfo-NHS and EDAC increased Z_t by 3.88×10^9 Ω. After the $CD4^+$ antibodies were attached Z_t decreased by 4.13×10^9 Ω. The impedance change caused by the further coating with BSA proteins was small (2.56×10^8 Ω). The difference of the low-frequency impedance before and after the cell capture was large (~10^{10} Ω) and consistent, being able to

distinguish the “on” and “off” states of the working electrode. Therefore the data at single frequency point (0.1 Hz) was analyzed in the following discussion.

Figure 6.6 shows the histogram of Z_t at 0.1 Hz obtained from 30 identical working electrodes. On the left side was the impedances measured on the electrodes that were coated with $CD4^+$ antibodies and BSA proteins, ranging from 3×10^9 Ω to 10×10^9 Ω. The bars on the right side, ranging from 1.2×10^{10} Ω to 2.2×10^{10} Ω, were measured from the same electrodes after they each were attached with a single cell. The two groups of data were located with a significant separation distance, representing the “empty” and “occupied” states, respectively. Figure 6.7 shows the distribution of the impedance change (ΔZ_t) caused by the cell attachment. The majority of the impedance changes fell in a narrow range, from 7.5×10^9 Ω to 9.5×10^9 Ω. Therefore a value of 5×10^9 Ω could serve as a reasonable threshold point for determining the binary status of the cell occupancy on the electrode.

In this biosensor, the cell counting was essentially digitalized. The total amount of the J45.01 cells captured by the electrode array was simply the sum of the electrode pixels in the “on” state. To verify the correlation between the impedance signals and the cell occupancies, the electrode array after the cell capture was inspected optically. The electrodes attached with cells were counted manually under microscope. Figure 6.8 is the comparison between the optical enumeration and the impedance detection approach. The linear relationship demonstrated the feasibility of using the pixel array of working electrodes for the precise counting of $CD4^+$ cells.

6.4 Conclusion

A microchip biosensor based on electrochemical impedance spectroscopy has been developed for precise counting human $CD4^+$ lymphocyte cells. The key feature of the sensor device was an array of densely packed working electrode pixels. Each of them was as small as a single $CD4^+$ cell. These working electrodes were chemically modified with $CD4^+$ antibodies on the surface, being able to selectively capture one single $CD4^+$ cell on each electrode. A Si_3N_4 grid structure was built along with the working electrode pixels, playing an important role in centering cells on the electrodes. The "on" and "off" states of each electrode pixel, depending on the cell capture status, was monitored by measuring the electrochemical impedance spectrum between the working and counter electrodes. The experiment data showed that the cell capture on an electrode pixel increased the interfacial impedance by at least 7×10^9 Ω. The cell counting by this pixelated electrode system agreed well with the optical counting.

The sensor device developed here was able to detect the cell targets at a single-cell resolution. The counting mechanism was independent of the sample concentration, particularly useful for detecting cells at very low concentrations. The capture of each individual cell on a pixel was determined in a binary mode, making the system robust to the signal noises. The sensor device, as well as the concept of electrode pixels, provided a promising approach for sensing biological species at single-object resolution and can be useful in the future biosensor applications.

REFERENCES

1 Masuda, H. and Fukuda, K., *Science* 268 (5216), 1466-1468 (1995).

2 Lira, H. D. L. and Paterson, R., *J. Membr. Sci.* 206 (1-2), 375-387 (2002).

3 Li, A. P., Muller, F., Birner, A., Nielsch, K., and Gosele, U., *J. Appl. Phys.* 84 (11), 6023-6026 (1998).

4 Harrop, P. J., *Br. J. Appl. Phys.* 16 (5), 729-730 (1965).

5 Loh, E., *Solid State Commun.* 2 (9), 269-272 (1964).

6 Pappis, J. and Kingery, W. D., *J. Am. Ceram. Soc.* 44 (9), 459-464 (1961).

7 Dittmer, G., *Thin Solid Films* 9 (3), 317-328 (1972).

8 Gould, R. D. and Hogarth, C. A., *Thin Solid Films* 51 (2), 237-250 (1978).

9 Hickmott, T. W., *J. Appl. Phys.* 36 (6), 1885-1896 (1965).

10 Hitzig, J., Juttner, K., Lorenz, W. J., and Paatsch, W., *Corrosion Sci.* 24 (11-1), 945-952 (1984).

11 Xia, Z., Riester, L., Sheldon, B. W., Curtin, W. A., Liang, J., Yin, A., and Xu, J. M., *Rev. Adv. Mater. Sci.* 6 (2), 131-139 (2004).

12 Diggle, J. W., Downie, T. C., and Goulding, C. W., *Chem. Rev.* 69 (3), 365-405 (1969).

13 Patnaik, P., *Handbook of Inorganic Chemicals*. (McGraw-Hill, 2002).

14 Almawlawi, D., Coombs, N., and Moskovits, M., *J. Appl. Phys.* 70 (8), 4421-4425 (1991).

15 Pontifex, G. H., Zhang, P., Wang, Z., Haslett, T. L., Almawlawi, D., and Moskovits, M., *J. Phys. Chem.* 95 (24), 9989-9993 (1991).

16 Nielsch, K., Muller, F., Li, A. P., and Gosele, U., *Adv. Mater.* 12 (8), 582-586 (2000).

17 Ohji, N., Enomoto, N., Mizushima, T., Kakuta, N., Morioka, Y., and Ueno, A., *J. Chem. Soc.-Faraday Trans.* 90 (9), 1279-1284 (1994).

18 Li, J., Papadopoulos, C., Xu, J. M., and Moskovits, M., *Appl. Phys. Lett.* 75 (3), 367-369 (1999).

19 Li, Y., Meng, G. W., Zhang, L. D., and Phillipp, F., *Appl. Phys. Lett.* 76 (15), 2011-2013 (2000).

20 Sugawara, S., Sakurai, I., Konno, M., and Saito, S., *J. Chem. Eng. Jpn.* 19 (5), 477-480 (1986).

21 Hoshino, S., Suzuki, K., and Nakane, K., *Trans. Inst. Metal Finish.* 75, 134-136 (1997).

22 Jirage, K. B., Hulteen, J. C., and Martin, C. R., *Science* 278 (5338), 655-658 (1997).

23 Onuki, K., Nakajima, H., Shimizu, S., and Nagoshi, M., *J. Chem. Eng. Jpn.* 30 (2), 359-362 (1997).

24 Pan, M., Cooper, C., Lin, Y. S., and Meng, G. Y., *J. Membr. Sci.* 158 (1-2), 235-241 (1999).

25 Pages, X., Rouessac, V., Cot, D., Nabias, G., and Durand, J., *Sep. Purif. Technol.* 25 (1-3), 399-406 (2001).

26 Kyotani, T., Xu, W. H., Yokoyama, Y., Inahara, J., Touhara, H., and Tomita, A., *J. Membr. Sci.* 196 (2), 231-239 (2002).

27 Asaeda, M. and Du, L. D., *J. Chem. Eng. Jpn.* 19 (1), 72-77 (1986).

28 Das, R. and Dutta, B. K., *Sep. Sci. Technol.* 34 (4), 609-625 (1999).

29 Lee, S. B., Mitchell, D. T., Trofin, L., Nevanen, T. K., Soderlund, H., and Martin, C. R., *Science* 296 (5576), 2198-2200 (2002).

30 Mitchell, D. T., Lee, S. B., Trofin, L., Li, N. C., Nevanen, T. K., Soderlund, H., and Martin, C. R., *J. Am. Chem. Soc.* 124 (40), 11864-11865 (2002).

31 Vlassiouk, I., Krasnoslobodtsev, A., Smirnov, S., and Germann, M., *Langmuir* 20 (23), 9913-9915 (2004).

32 Inada, T., Uno, N., Kato, T., and Iwamoto, Y., *J. Mater. Res.* 20 (1), 114-120 (2005).

33 Cheow, P. S., Zhi, E., Ting, C., Tan, M. Q., and Toh, C. S., *Electrochim. Acta* 53 (14), 4669-4673 (2008).

34 Gong, D. W., Yadavalli, V., Paulose, M., Pishko, M., and Grimes, C. A., *Biomed. Microdevices* 5 (1), 75-80 (2003).

35 Kipke, S. and Schmid, G., *Adv. Funct. Mater.* 14 (12), 1184-1188 (2004).

36 Hohlbein, J., Steinhart, M., Schiene-Fischer, C., Benda, A., Hof, M., and Hubner, C. G., *Small* 3 (3), 380-385 (2007).

37 Nahar, R. K. and Khanna, V. K., *Int. J. Electron.* 52 (6), 557-567 (1982).

38 Heilmann, A., Teuscher, N., Kiesow, A., Janasek, D., and Spohn, U., *J. Nanosci. Nanotechnol.* 3 (5), 375-379 (2003).

39 Varghese, O. K., Gong, D. W., Dreschel, W. R., Ong, K. G., and Grimes, C. A., *Sens. Actuator B-Chem.* 94 (1), 27-35 (2003).

40 Sano, T., Iguchi, N., Iida, K., Sakamoto, T., Baba, M., and Kawaura, H., *Appl. Phys. Lett.* 83 (21), 4438-4440 (2003).

41 Takoh, K., Takahashi, A., Matsue, T., and Nishizawa, M., *Anal. Chim. Acta* 522 (1), 45-49 (2004).

42 Matsumoto, F., Nishio, K., and Masuda, H., *Adv. Mater.* 16 (23-24), 2105-2108 (2004).

43 Cloutier, S. G., Lazareck, A. D., and Xu, J., *Appl. Phys. Lett.* 88 (1) (2006).

44 Steinle, E. D., Mitchell, D. T., Wirtz, M., Lee, S. B., Young, V. Y., and Martin, C. R., *Anal. Chem.* 74 (10), 2416-2422 (2002).

45 Vlassiouk, I., Takmakov, P., and Smirnov, S., *Langmuir* 21 (11), 4776-4778 (2005).

46 Takmakov, P., Vlassiouk, I., and Smirnov, S., *Analyst* 131 (11), 1248-1253 (2006).

47 Kim, D. K., Tamiya, E., Jung, K. H., Shin, H. K., and Kwon, Y. S., *Curr. Appl. Phys.* 6 (4), 663-668 (2006).

48 Kang, M. C., Trofin, L., Mota, M. O., and Martin, C. R., *Anal. Chem.* 77 (19), 6243-6249 (2005).

49 Takmakov, P., Vlassiouk, I., and Smirnov, S., *Anal. Bioanal. Chem.* 385 (5), 954-958 (2006).

50 Darder, M., Aranda, P., Hernandez-Velez, M., Manova, E., and Ruiz-Hitzky, E., *Thin Solid Films* 495 (1-2), 321-326 (2006).

51 Hou, S. F., Wang, J. H., and Martin, C. R., *J. Am. Chem. Soc.* 127 (24), 8586-8587 (2005).

52 Hou, S. F., Wang, J. H., and Martin, C. R., *Nano Lett.* 5 (2), 231-234 (2005).

53 Masuda, H., Yamada, H., Satoh, M., Asoh, H., Nakao, M., and Tamamura, T., *Appl. Phys. Lett.* 71 (19), 2770-2772 (1997).

54 Asoh, H., Nishio, K., Nakao, M., Tamamura, T., and Masuda, H., *J. Electrochem. Soc.* 148 (4), B152-B156 (2001).

55 Masuda, H., Hasegwa, F., and Ono, S., *J. Electrochem. Soc.* 144 (5), L127-L130 (1997).

56 Jessensky, O., Muller, F., and Gosele, U., *J. Electrochem. Soc.* 145 (11), 3735-3740 (1998).

57 Jessensky, O., Muller, F., and Gosele, U., *Appl. Phys. Lett.* 72 (10), 1173-1175 (1998).

58 Li, A. P., Muller, F., Birner, A., Nielsch, K., and Gosele, U., *Adv. Mater.* 11 (6), 483-487 (1999).

59 Li, A. P., Muller, F., and Gosele, U., *Electrochem. Solid State Lett.* 3 (3), 131-134 (2000).

60 Muller, F., Birner, A., Schilling, J., Li, A. P., Nielsch, K., Gosele, U., and Lehmann, V., *Microsyst. Technol.* 8 (1), 7-9 (2002).

61 Wood, G. C., Osullivan, J. P., and Vaszko, B., *J. Electrochem. Soc.* 115 (6), 618-620 (1968).

62 Furneaux, R. C., Rigby, W. R., and Davidson, A. P., *Nature* 337 (6203), 147-149 (1989).

63 Yuan, J. H., Chen, W., Hui, R. J., Hu, Y. L., and Xia, X. H., *Electrochim. Acta* 51 (22), 4589-4595 (2006).

64 Tian, M. L., Xu, S. Y., Wang, J. G., Kumar, N., Wertz, E., Li, Q., Campbell, P. M., Chan, M. H. W., and Mallouk, T. E., *Nano Lett.* 5 (4), 697-703 (2005).

65 Plecis, A., Schoch, R. B., and Renaud, P., *Nano Lett.* 5 (6), 1147-1155 (2005).

66 Liu, Y.-C., Wang, Q., and Lu, L.-H., *J. Chem. Phys.* 120 (22), 10728-10735 (2004).

67 Xu, B., Ooi, K. T., Wong, T. N., and Liu, C. Y., *J. Micromech. Microeng.* 9 (4), 377-384 (1999).

68 Dalvie, S. K. and Baltus, R. E., *J. Membr. Sci.* 71 (3), 247-255 (1992).

69 Bluhm, E. A., Bauer, E., Chamberlin, R. M., Abney, K. D., Young, J. S., and Jarvinen, G. D., *Langmuir* 15 (25), 8668-8672 (1999).

70 Bluhm, E. A., Schroeder, N. C., Bauer, E., Fife, J. N., Chamberlin, R. M., Abney, K. D., Young, J. S., and Jarvinen, G. D., *Langmuir* 16 (17), 7056-7060 (2000).

71 Thompson, G. E. and Wood, G. C., *Nature* 290 (5803), 230-232 (1981).

72 Guthe, K. E., *Phys. Rev.* 15 (6), 327-334 (1902).

73 Fitch, A. L., *Phys. Rev.* 9 (1), 15-28 (1917).

74 Meserve, W. E., *Phys. Rev.* 30 (2), 215-221 (1927).

75 Setoh, S. and Miyata, A., *Sci. Paper. Inst. Phys. Chem. Res.* 19, 237-291 (1932).

76 Keller, F., Hunter, M. S., and Robinson, D. L., *J. Electrochem. Soc.* 100 (9), 411-419 (1953).

77 Paolini, G., Masoero, M., Sacchi, F., and Paganell.M, *J. Electrochem. Soc.* 112 (1), 32-38 (1965).

78 Jagminas, A., Bigeliene, D., Mikulskas, I., and Tomasiunas, R., *J. Cryst. Growth* 233 (3), 591-598 (2001).

79 Sulka, G. D., Stroobants, S., Moshchalkov, V., Borghs, G., and Celis, J. P., *J. Electrochem. Soc.* 149 (7), D97-D103 (2002).

80 Sulka, G. D. and Parkola, K. G., *Thin Solid Films* 515 (1), 338-345 (2006).

81 Thompson, G. E., *Thin Solid Films* 297 (1-2), 192-201 (1997).

82 O'sullivan, J. P. and Wood, G. C., *Proceedings of the Royal Society of London, Series A: Mathematical and Physical Sciences* 317 (1531), 511-543 (1970).

83 Parkhutik, V. P. and Shershulsky, V. I., *J. Phys. D-Appl. Phys.* 25 (8), 1258-1263 (1992).

84 Patermarakis, G., Lenas, P., Karavassilis, C., and Papayiannis, G., *Electrochim. Acta* 36 (3-4), 709-725 (1991).

85 Patermarakis, G. and Kerassovitou, P., *Electrochim. Acta* 37 (1), 125-137 (1992).

86 Patermarakis, G. and Papandreadis, N., *Electrochim. Acta* 38 (15), 2351-2361 (1993).

87 Patermarakis, G. and Tzouvelekis, D., *Electrochim. Acta* 39 (16), 2419-2429 (1994).

88 Patermarakis, G. and Karayannis, H. S., *Electrochim. Acta* 40 (16), 2647-2656 (1995).

89 Patermarakis, G. and Moussoutzanis, K., *J. Electrochem. Soc.* 142 (3), 737-743 (1995).

90 Patermarakis, G., *Electrochim. Acta* 41 (16), 2601-2611 (1996).

91 Patermarakis, G., *J. Electroanal. Chem.* 404 (1), 69-76 (1996).

92 Patermarakis, G., *J. Electroanal. Chem.* 447 (1-2), 25-41 (1998).

93 Patermarakis, G., Moussoutzanis, K., and Chandrinos, J., *Appl. Catal. A-Gen.* 180 (1-2), 345-358 (1999).

94 Patermarakis, G. and Nicolopoulos, N., *J. Catal.* 187 (2), 311-320 (1999).

95 Patermarakis, G., Moussoutzanis, K., and Chandrinos, J., *J. Solid State Electrochem.* 6 (1), 39-54 (2001).

96 Patermarakis, G. and Masavetas, K., *J. Electroanal. Chem.* 588 (2), 179-189 (2006).

97 Patermarakis, G., Chandrinos, J., and Masavetas, K., *J. Solid State Electrochem.* 11 (9), 1191-1204 (2007).

98 Thamida, S. K. and Chang, H. C., *Chaos* 12 (1), 240-251 (2002).

99 Hoar, T. P. and Mott, N. F., *J. Phys. Chem. Solids* 9 (2), 97-99 (1959).

100 Hunter, M. S. and Fowle, P., *J. Electrochem. Soc.* 101 (10), 514-519 (1954).

101 Michelson, C. E., *J. Electrochem. Soc.* 115 (2), 213-219 (1968).

102 Diggle, J. W., Downie, T. C., and Goulding, C. W., *J. Electrochem. Soc.* 116 (10), 1347-& (1969).

103 Siejka, J. and Ortega, C., *J. Electrochem. Soc.* 124 (6), 883-891 (1977).

104 Mei, Y. F., Siu, G. G., Zou, J. P., and Wu, X. L., *Phys. Lett. A* 324 (5-6), 479-483 (2004).

105 Sulka, G. D. and Parkola, K. G., *Electrochim. Acta* 52 (5), 1880-1888 (2007).

106 Li, A. P., Muller, F., Birner, A., Nielsch, K., and Gosele, U., *J. Vac. Sci. Technol. A-Vac. Surf. Films* 17 (4), 1428-1431 (1999).

107 Asoh, H., Nishio, K., Nakao, M., Yokoo, A., Tamamura, T., and Masuda, H., *J. Vac. Sci. Technol. B* 19 (2), 569-572 (2001).

108 Ono, S., Saito, M., Ishiguro, M., and Asoh, H., *J. Electrochem. Soc.* 151 (8), B473-B478 (2004).

109 Zhou, W. Y., Li, Y. B., Liu, Z. Q., Tang, D. S., Zou, X. P., and Gang, W., *Chin. Phys.* 10 (3), 218-222 (2001).

110 Booker, C. J. L., Wood, J. L., and Walsh, A., *Nature* 176 (4474), 222-223 (1955).

111 Serebrennikova, I., Vanysek, P., and Birss, V. I., *Electrochim. Acta* 42 (1), 145-151 (1997).

112 Zahavi, J. and Metzger, M., *J. Electrochem. Soc.* 119 (11), 1479-1485 (1972).

113 Zhang, L., Cho, H. S., Li, F., Metzger, R. M., and Doyle, W. D., *J. Mater. Sci. Lett.* 17 (4), 291-294 (1998).

114 Masuda, H., Watanabe, M., Yasui, K., Tryk, D., Rao, T., and Fujishima, A., *Adv. Mater.* 12 (6), 444-447 (2000).

115 Liu, C. Y., Datta, A., and Wang, Y. L., *Appl. Phys. Lett.* 78 (1), 120-122 (2001).

116 Masuda, H., Asoh, H., Watanabe, M., Nishio, K., Nakao, M., and Tamamura, T., *Adv. Mater.* 13 (3), 189-192 (2001).

117 Li, F. Y., Zhang, L., and Metzger, R. M., *Chem. Mat.* 10 (9), 2470-2480 (1998).

118 Ba, L. and Li, W. S., *J. Phys. D-Appl. Phys.* 33 (20), 2527-2531 (2000).

119 Franklin, R. W. and Stirland, D. J., *J. Electrochem. Soc.* 110 (4), 262-267 (1963).

120 Lee, W., Nielsch, K., and Gosele, U., *Nanotechnology* 18 (47) (2007).

121 Kashi, M. A., Ramazani, A., Rahmandoust, M., and Noormohammadi, M., *J. Phys. D-Appl. Phys.* 40 (15), 4625-4630 (2007).

122 Bai, A., Hu, C. C., Yang, Y. F., and Lin, C. C., *Electrochim. Acta* 53 (5), 2258-2264 (2008).

123 Masuda, H., Yotsuya, M., Asano, M., Nishio, K., Nakao, M., Yokoo, A., and Tamamura, T., *Appl. Phys. Lett.* 78 (6), 826-828 (2001).

124 Ding, G. Q., Zheng, M. J., Xu, W. L., and Shen, W. Z., *Nanotechnology* 16 (8), 1285-1289 (2005).

125 Masuda, H. and Satoh, M., *Jpn. J. Appl. Phys. Part 2 - Lett.* 35 (1B), L126-L129 (1996).

126 Choi, J., Nielsch, K., Reiche, M., Wehrspohn, R. B., and Gosele, U., *J. Vac. Sci. Technol. B* 21 (2), 763-766 (2003).

127 Asoh, H., Ono, S., Hirose, T., Nakao, M., and Masuda, H., *Electrochim. Acta* 48 (20-22), 3171-3174 (2003).

128 Oh, H. J., Lee, J. H., Ahn, H. J., Jeong, Y., Heo, C. H., and Chi, C. S., *J. Electroceram.* 17 (2-4), 369-373 (2006).

129 Gould, R. D., *Thin Solid Films* 89 (1), 49-55 (1982).

130 Gould, R. D. and Sadler, D. N., *Int. J. Electron.* 54 (1), 21-30 (1983).

131 Hickmott, T. W., *J. Appl. Phys.* 35 (7), 2118-2122 (1964).

132 Yamamoto, Y., Baba, N., and Tajima, S., *Nature* 289 (5798), 572-574 (1981).

133 Du, Y., Cai, W. L., Mo, C. M., Chen, J., Zhang, L. D., and Zhu, X. G., *Appl. Phys. Lett.* 74 (20), 2951-2953 (1999).

134 Huang, G. S., Wu, X. L., Mei, Y. F., Shao, X. F., and Siu, G. G., *J. Appl. Phys.* 93 (1), 582-585 (2003).

135 Xu, W. L., Zheng, M. J., Wu, S., and Shen, W. Z., *Appl. Phys. Lett.* 85 (19), 4364-4366 (2004).

136 Huang, G. S., Wu, X. L., Xie, Y., Shao, X. F., and Wang, S. H., *J. Appl. Phys.* 94 (4), 2407-2410 (2003).

137 Dorre, E. and Hobner, H., *Alumina*. (Springer-Verlag, New York, 1984).

138 Callister, D. W., *Materials Science and Engineering: An Introduction*, 3rd ed. (Wiley, New York, 1994).

139 Yasuichi, S. and Takemi, C., *Denki Kagaku* 38 (11), 848- (1970).

140 Jeon, J. H., Choi, D. H., Lee, P. S., Lee, K. H., Park, H. C., and Hwang, W., *Mech. Compos. Mater.* 42 (2), 173-186 (2006).

141 Sokol, V., Vrublevsky, I., Parkun, V., and Moskvichev, K., *Anal. Bioanal. Chem.* 375 (7), 968-973 (2003).

142 Choi, D., Lee, S., Lee, C., Lee, P., Lee, J., Lee, K., Park, H., and Hwang, W., *J. Micromech. Microeng.* 17 (3), 501-508 (2007).

143 Choi, D., Lee, S., Kim, S., Lee, P., Lee, K., Park, H., and Hwang, W., *Scr. Mater.* 58 (10), 870-873 (2008).

144 Choi, D., Kim, S., Lee, S., Kim, D., Lee, K., Park, H., and Hwang, A., *Nanotechnology* 19 (14) (2008).

145 Madhusudana, C. V. and Fletcher, L. S., *Aiaa J.* 24 (3), 510-523 (1986).

146 Fletcher, L. S., *J. Heat Transf.-Trans. ASME* 110 (4B), 1059-1070 (1988).

147 Ogden, T. R., Rathsam, A. D., and Gilchrist, J. T., *Mater. Lett.* 5 (3), 84-87 (1987).

148 Borca-Tasciuc, D. A. and Chen, G., *J. Appl. Phys.* 97 (8) (2005).

149 Madou, M., *Fundamentals of Microfabrication*. (CRC Press, Boca Raton, 1997).

150 Tiwari, S., Rana, F., Hanafi, H., Hartstein, A., Crabbe, E. F., and Chan, K., *Appl. Phys. Lett.* 68 (10), 1377-1379 (1996).

151 Brumlik, C. J. and Martin, C. R., *J. Am. Chem. Soc.* 113 (8), 3174-3175 (1991).

152 Whitney, T. M., Jiang, J. S., Searson, P. C., and Chien, C. L., *Science* 261 (5126), 1316-1319 (1993).

153 Nielsch, K., Wehrspohn, R. B., Barthel, J., Kirschner, J., Gosele, U., Fischer, S. F., and Kronmuller, H., *Appl. Phys. Lett.* 79 (9), 1360-1362 (2001).

154 Choi, J., Sauer, G., Nielsch, K., Wehrspohn, R. B., and Gosele, U., *Chem. Mat.* 15 (3), 776-779 (2003).

155 Sander, M. S. and Tan, L. S., *Adv. Funct. Mater.* 13 (5), 393-397 (2003).

156 Rabin, O., Herz, P. R., Lin, Y. M., Akinwande, A. I., Cronin, S. B., and Dresselhaus, M. S., *Adv. Funct. Mater.* 13 (8), 631-638 (2003).

157 Sander, M. S., Gronsky, R., Sands, T., and Stacy, A. M., *Chem. Mat.* 15 (1), 335-339 (2003).

158 Hobbs, K. L., Larson, P. R., Lian, G. D., Keay, J. C., and Johnson, M. B., *Nano Lett.* 4 (1), 167-171 (2004).

159 Kim, K. T., Sim, S. J., and Cho, S. M., *IEEE Sens. J.* 6 (3), 509-513 (2006).

160 Wu, C. T., Ko, F. H., and Hwang, H. Y., *Microelectron. Eng.* 83 (4-9), 1567-1570 (2006).

161 Bauer, L. A., Birenbaum, N. S., and Meyer, G. J., *J. Mater. Chem.* 14 (4), 517-526 (2004).

162 Das, B., *J. Electrochem. Soc.* 151 (6), D46-D50 (2004).

163 Toh, C. S., Kayes, B. M., Nemanick, E. J., and Lewis, N. S., *Nano Lett.* 4 (5), 767-770 (2004).

164 Kokonou, M., Nassiopoulou, A. G., and Giannakopoulos, K. P., *Nanotechnology* 16 (1), 103-106 (2005).

165 Xu, T. T., Piner, R. D., and Ruoff, R. S., *Langmuir* 19 (4), 1443-1445 (2003).

166 Jiang, X., Turner, J. N., and Spencer, M. G., *The 2004-2005 CNF Research Accomplishments*, 62-63 (2005).

167 Jiang, X., Mishra, N., Turner, J. N., and Spencer, M. G., *Microfluid. Nanofluid.* 5 (5), 695-701 (2008).

168 Crouse, D., Lo, Y. H., Miller, A. E., and Crouse, M., *Appl. Phys. Lett.* 76 (1), 49-51 (2000).

169 Asoh, H., Matsuo, M., Yoshihama, M., and Ono, S., *Appl. Phys. Lett.* 83 (21), 4408-4410 (2003).

170 Kanamori, Y., Hane, K., Sai, H., and Yugami, H., *Appl. Phys. Lett.* 78 (2), 142-143 (2001).

171 Jiang, X., Mishra, N., Turner, J. N., and Spencer, M. G., *IEEE Trans. Nanotechnol.* 6 (3), 328-333 (2007).

172 Schneider, J. J., Engstler, N., Budna, K. P., Teichert, C., and Franzka, S., *Eur. J. Inorg. Chem.* (12), 2352-2359 (2005).

173 Lau, K. H. A., Tan, L. S., Tamada, K., Sander, M. S., and Knoll, W., *J. Phys. Chem. B* 108 (30), 10812-10818 (2004).

174 Metzger, R. M., Konovalov, V. V., Sun, M., Xu, T., Zangari, G., Xu, B., Benakli, M., and Doyle, W. D., *IEEE Trans. Magn.* 36 (1), 30-35 (2000).

175 Sander, M. S., Prieto, A. L., Gronsky, R., Sands, T., and Stacy, A. M., *Adv. Mater.* 14 (9), 665-667 (2002).

176 Wolfrum, B., Mourzina, Y., Sommerhage, F., and Offenhausser, A., *Nano Lett.* 6 (3), 453-457 (2006).

177 Winkler, B. H. and Baltus, R. E., *J. Membr. Sci.* 226 (1-2), 75-84 (2003).

178 Nishizawa, M., Menon, V. P., and Martin, C. R., *Science* 268 (5211), 700-702 (1995).

179 Daiguji, H., Yang, P. D., and Majumdar, A., *Nano Lett.* 4 (1), 137-142 (2004).

180 Bruus, H., *Theoretical Microfluidics*. (Oxford, New York, 2007).

181 Price, W. E., *J. Chem. Soc., Faraday Trans. 1* 85, 415-419 (1989).

182 Niesner, R. and Heintz, A., *J. Chem. Eng. Data* 45 (6), 1121-1124 (2000).

183 Pfenniger, M. and Calzaferri, G., *ChemPhysChem* 1 (4), 211-217 (2000).

184 Hinds, B. J., Chopra, N., Rantell, T., Andrews, R., Gavalas, V., and Bachas, L. G., *Science* 303 (5654), 62-65 (2004).

185 Watson, J. D. and Crick, F. H. C., *Cold Spring Harbor Symp. Quant. Biol.* 18, 123-131 (1953).

186 Lee, J. W., Nigo, S., Nakano, Y., Nahlovskyy, B., Kato, S., Kitazawa, H., and Kido, G., in *21st International Microprocesses and Nanotechnology Conference* (Fukuoka, Japan, 2008).

187 Mathews, C. K. and Van Holde, K. E., *Biochemistry*. (Benjamin/Cummings, Redwood City, 1990).

188 Peterlinz, K. A., Georgiadis, R. M., Herne, T. M., and Tarlov, M. J., *J. Am. Chem. Soc.* 119 (14), 3401-3402 (1997).

189 Peterson, A. W., Wolf, L. K., and Georgiadis, R. M., *J. Am. Chem. Soc.* 124 (49), 14601-14607 (2002).

190 Eimer, W. and Pecora, R., *J. Chem. Phys.* 94 (3), 2324-2329 (1991).

191 Joint United Nations Programme on HIV/AIDS, *2008 Report on the Global Aids Epidemic*, 2008.

192 Rodriguez, W. R., Christodoulides, N., Floriano, P. N., Graham, S., Mohanty, S., Dixon, M., Hsiang, M., Peter, T., Zavahir, S., Thior, I., Romanovicz, D., Bernard, B., Goodey, A. P., Walker, B. D., and Mcdevitt, J. T., *PLos Med.* 2 (7), 663-672 (2005).

193 Cheng, X. H., Irimia, D., Dixon, M., Sekine, K., Demirci, U., Zamir, L., Tompkins, R. G., Rodriguez, W., and Toner, M., *Lab Chip* 7 (2), 170-178 (2007).

194 Cheng, X. H., Irimia, D., Dixon, M., Ziperstein, J. C., Demirci, U., Zamir, L., Tompkins, R. G., Toner, M., and Rodriguez, W. R., *Jaids* 45 (3), 257-261 (2007).

195 Thorslund, S., Larsson, R., Nikolajeff, F., Bergquist, J., and Sanchez, J., *Sens. Actuator B-Chem.* 123 (2), 847-855 (2007).

196 Thorslund, S., Larsson, R., Bergquist, J., Nikolajeff, F., and Sanchez, J., *Biomed. Microdevices* 10 (6), 851-857 (2008).

197 Jokerst, J. V., Floriano, P. N., Christodoulides, N., Simmons, G. W., and Mcdevitt, J. T., *Lab Chip* 8 (12), 2079-2090 (2008).

198 Wang, Y. N., Kang, Y. J., Xu, D. Y., Chon, C. H., Barnett, L., Kalams, S. A., Li, D. Y., and Li, D. Q., *Lab Chip* 8 (2), 309-315 (2008).

199 Mishra, N. N., Retterer, S., Zieziulewicz, T. J., Isaacson, M., Szarowski, D., Mousseau, D. E., Lawrence, D. A., and Turner, J. N., *Biosens. Bioelectron.* 21 (5), 696-704 (2005).

200 Cheng, X., Liu, Y. S., Irimia, D., Demirci, U., Yang, L. J., Zamir, L., Rodriguez, W. R., Toner, M., and Bashir, R., *Lab Chip* 7 (6), 746-755 (2007).